Mechanics of Exchange Flow between Open Water and an Aquatic Canopy

by

Xueyan Zhang

M.Phil., University of Hong Kong, Hong Kong, 2006

Submitted to the Department of Civil and Environmental Engineering
in partial fulfillment of the requirements for the degree of

Doctor of Philosophy in the field of Environmental Fluid Mechanics

at the

MASSACHUSETTS INSTITUTE OF TECHNOLOGY

September 2010

Author .....
Department of Civil and Environmental Engineering
July 31, 2010

Certified by .....
Heidi M. Nepf
Professor of Civil and Environmental Engineering
Thesis Supervisor

Accepted by .....
Daniele Veneziano
Chairman, Departmental Committee for Graduate Students

Mechanics of Exchange Flow between Open Water and an Aquatic Canopy

by

Xueyan Zhang

Submitted to the Department of Civil and Environmental Engineering
on July 31, 2010, in partial fulfillment of the
requirements for the degree of
Doctor of Philosophy in the field of Environmental Fluid Mechanics

Abstract

The presence of aquatic vegetation is a common feature in shallow water systems. It alters the dynamics of the system by producing additional drag and by generating differential heating between regions of vegetation and open water through the shading it provides. The differential heating creates density differences that drive flow between vegetated and open regions. This thesis presents a series of experiments that explored the magnitude and structure of these exchange flows for different forcing and vegetation distributions.

The first project considers emergent vegetation with flow forced by a constant density difference. After a short inertial period, the discharge is controlled by the vegetative drag, and the current entering the vegetation, as well as the total discharge, decrease with time. The toe velocity of the current moving into the open region is controlled only by inertia and is constant in time.

The second project considers emergent vegetation with a temporally increasing density difference, which was generated by a constant heat input. In the vegetated region, both the buoyancy and vegetative drag experienced by the intruding current increase linearly in time, offsetting on another and resulting in a current velocity moving into the vegetation that is constant in time. The thickness of this intruding layer is set by the length scale of light penetration.

The third project considers a mat of floating vegetation whose roots penetrate a fraction of the water depth. The flow was driven by a constant density difference (constant g'). The flow entering the vegetated side bifurcates, with some flow moving through the root layer and the remaining flow displaced downward beneath this layer. The fraction of flow going through and beneath the root layer is allocated such that the conversion from potential energy to kinetic energy is maximized in the system.

Finally, this work shows that thermally-driven exchange flow can flush a significant portion of a vegetated sidearm during a diurnal cycle and thus can play a crucial role in the mass balance and distribution in a natural water body.

Thesis Supervisor: Heidi M. Nepf
Title: Professor of Civil and Environmental Engineering

Acknowledgments

First and foremost, I wish to express my greatest appreciation to my advisor, Professor Heidi Nepf for sharing with me her creativity, knowledge and passion for high quality research and effective teaching. This thesis would not be accomplished without her guidance. What I have learned from Professor Nepf is far beyond fluid mechanics. She always encourages and supports me to explore different fields, not only in science and engineering, but also in business; I had many opportunities to apply my transferable to solve challenging and interesting problems in business.

I would also like to thank my thesis committee, Doctor Eric Adams and Professor Chiang C. Mei, for their time, insights and advice.

I also benefit a great deal from my discussions with fellow students at Parsons, Dr. Brian White, Dr. Anne Lightbody, Dr. Yukie Tanino, Dr. Peter Israelsson, Dr. Aaron Chow, Dr. David Gonzalez-Rodriguez, Mitul Luhar, Jeff Rominger, Lijun Zong, Mack Durham, Marcus, Tanvir Ahmed and Jim Gensheimer.

I also want to thank many supporting staff at Parsons Lab. My research would not have been so smooth without their help and hard work.

Last but not least, my parents and my wife, Jennifer C. Ye, deserve my sincerest thanks for their care and love. They are always a fountain of love and support that helps me overcome difficulties.

This thesis is based on work supported by the National Science Foundation under grant EAR0509658. Any opinions, findings or recommendations expressed herein are those of the authors and do not necessarily reflect the views of the National Science Foundation. The author was also supported by the Martin Family Society Fellowship for Sustainability in the spring of 2008.

Contents

List of Figures

List of Tables

Chapter 1

Introduction

The study of water systems is a highly interdisciplinary subject. A full understanding of surface water systems requires in depth understanding of the physical, chemical and biological processes involved in the system, as well as their interactions. In this thesis, I focus on the physical aspect of the water system. More specifically, I want to study the influence of vegetation in generating and controlling exchange flows. Exchange flow can occur when adjacent water regions have a density difference. In the resulting flow, a layer of heavy fluid moves along the bottom and a layer of lighter water moves in the opposing direction at the surface. Since exchange flow is generally driven by a density difference, it is also called gravity current in the literature. In fresh water systems, this type of exchange flow is primarily driven by temperature difference. In coastal system, it can also be driven by salinity gradients.

Emergent and aquatic vegetation is a common feature in littoral regions. The presence of aquatic vegetation alters the dynamics of the water flow in two important ways. First, aquatic vegetation introduces additional drag to the flow. This additional hydraulic resistance not only diminishes the magnitude of the flow inside the vegetation, but also alters the flow structure. Second, aquatic vegetation can cause differential heating, which is the main driving force of the exchange flow in fresh water systems. The emergent portion of the vegetation prevents the water underneath from directly receiving solar radiation during the daytime. Compared to adjacent open water, the amount of solar energy absorbed by the vegetated water is substantially

less. This uneven absorption of solar energy creates a temperature difference, which drives an exchange flow between the open and vegetated regions. Rooted, emergent vegetation, as well as floating vegetation can generate temperature difference (Dale and Gillespie, 1976; Ultsch, 1973). In addition to the physical influence described above, aquatic vegetation also creates a distinct biochemical environment within the vegetated water (Jacob and Otte, 2004; Lee and McNaughton. 2004). The exchange flow thus builds an important hydrodynamic link between biologically and chemically distinct regions of surface water. The distinct properties residing inside the vegetated region are carried into the open water by the exchange flow. During periods of weak wind, or within a protected water body, thermally-driven exchange flows have be observed to have significant influence on the distribution/redistribution of pollutants, nutrients and contaminants in the water body (Nepf and Oldham, 1997; Knauer *et al.*, 2000).

The classic exchange flow between two unobstructed flow domains was studied by Benjamin (1968). A sketch of the flow is depicted in Fig. 1.1. In the absence of dissipation, each exchange current occupies half of the water depth, H. The interface of the two current is approximately horizontal. The toe velocities of the currents moving in both directions are controlled by the balance between inertia and buoyancy and given by $\sqrt{g'H/4}$, where g' is the reduce gravity due to the density difference of water.

More recently, Tanino *et al.* (2005) studied the exchange flow within a canopy of rooted, emergent vegetation. A sketch of the flow for this case is shown in Fig. 1.2. The presence of vegetative drag alters the vertical velocity structure of the exchange flow; the exchange current exhibits a triangular shape. Tanino *et al.* (2005) have identified two drag regimes associated with exchange within a vegetated region. Depending on the stem Reynolds number, the vegetative drag may switch from a quadratic to a linear dependence on velocity.

This thesis presents a series of experiments that examine the combined effects of vegetative drag and vegetative shading on exchange flow. Chapter 2 describes an experimental study of a density-driven exchange flow between open water and

emergent vegetation that uses a lock exchange configuration. In this case, the density difference between two fluids is constant, *i.e.* $g' = (\rho_2 - \rho_1)g/\rho_1$ (Fig. 1.3). In this case, the drag in the vegetated region is distributed uniformly across the depth. The gravity current in the open region moves at a constant speed set by the initial inertial condition, $u_i = \sqrt{g'H/4}$. The speed of the current in the vegetative region is controlled by the canopy drag and decreases with time. Model predictions of toe velocity and discharge are also verified with experimental observations.

Chapter 3 describes a thermally-driven exchange flow between open water and a rooted, emergent canopy. Compared to the work in chapter 2, the exchange flow in this case is driven by a thermal forcing, and thus the density difference is time-varying, *i.e.* $g' = f(\text{time})$ (Fig. 1.4). Scaling analysis identifies several distinct flow regimes, namely, inertia-dominated, drag-dominated and energy-dominated regimes. The velocity scale in each regime is derived. The thickness of the intruding layer is set by the light penetration. The velocity field inside the vegetated region was quantified using Particle Imaging Velocimetry (PIV). And the experimental data are used to validate the model from scaling analysis.

Chapter 4 describes the exchange flow generated by floating vegetation (Fig. 1.5). The flow entering the vegetated region bifurcates, with some flow moving through the root layer of vegetation and the remaining flow displaced downward beneath this layer. After an inertial transient, the velocity through the root layer is less than the velocity of the underflow. A model is developed that predicts the flow rates within the root layer and the underflow based on energy considerations. The system adjusts the energy losses due to drag dissipation in the root layer and the potential energy cost to displace the underflow beneath the root layer, so that the resulting kinetic energy is maximized, which also maximizes the resulting volumetric exchange.

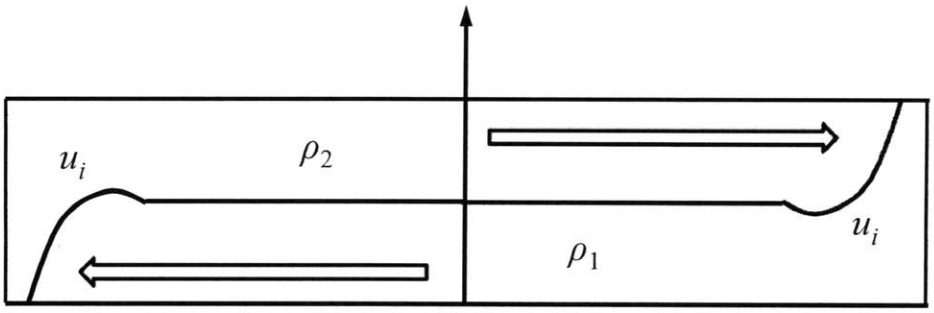

Figure 1.1: Classic exchange flow between two unobstructed regions (Benjamin, 1968). The toe velocity of the current in both region is equal to $\sqrt{g'H/4}$ and is constant in time. Here, $\rho_2 < \rho_1$ and $g' = (\rho_2 - \rho_1)g/\rho_1$.

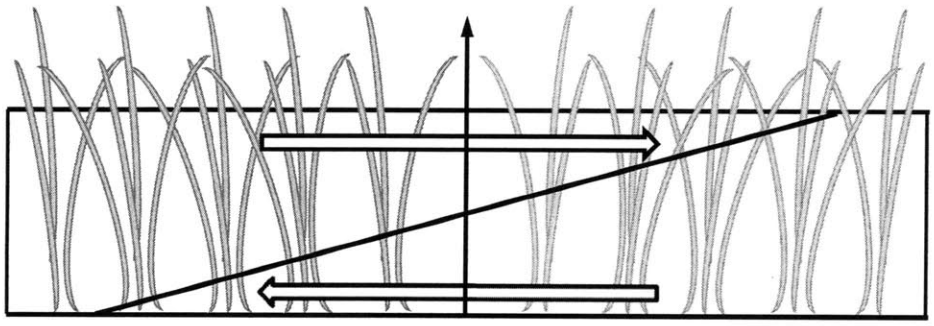

Figure 1.2: Exchange flow within vegetation (Tanino *et al.*, 2005). The solid line shows the interface of the exchange current.

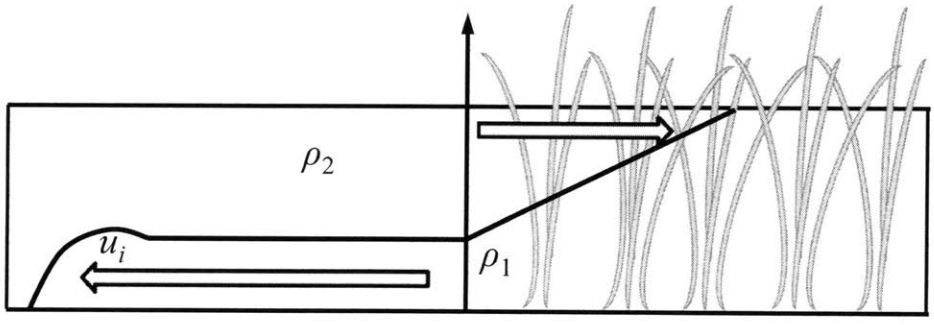

Figure 1.3: Exchange flow between open water and rooted emergent vegetation, where the density difference of water is constant.

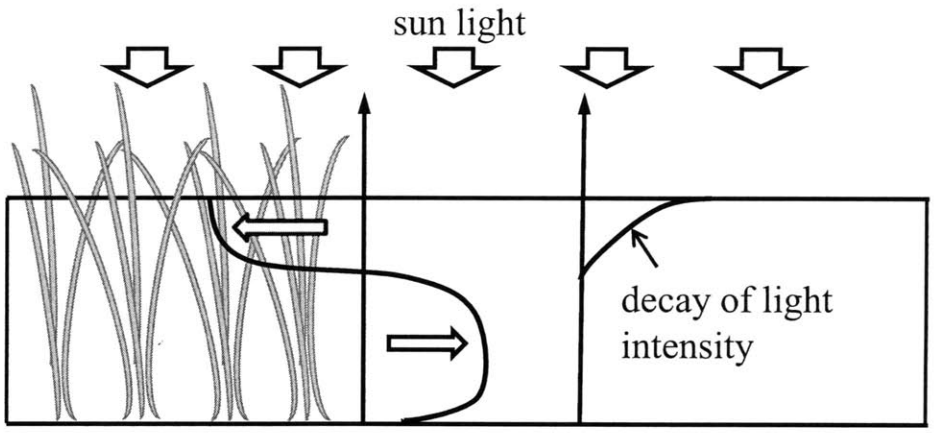

Figure 1.4: Thermally-driven exchange flow between open water and rooted emergent vegetation, where the density difference of water is time-varying.

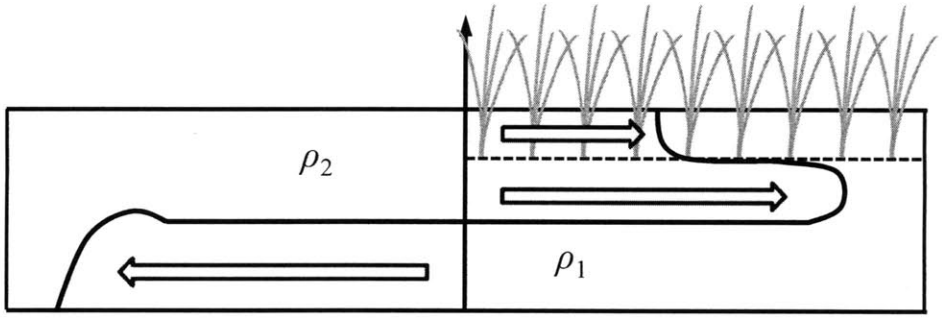

Figure 1.5: Exchange flow between open water and floating vegetation, where the density difference of water is constant. The dashed line indicates the bottom of root layer.

Chapter 2

Density Driven Exchange Flow between Open Water and an Aquatic Canopy

Abstract

Differences in water density can drive an exchange flow between the vegetated and open regions of surface water systems. A laboratory experiment has been conducted to investigate this exchange flow, using a random array of rigid, emergent cylinders to represent the canopy region. The flow pattern was captured using a CCD camera. The velocity of the current entering the canopy and the volume discharge both decrease with increasing vegetative drag, and also decrease gradually over time. Theoretical predictions for velocity and discharge rate are developed and verified with experimental observations. Extensions to field conditions are also discussed.

[1]This chapter is Zhang and Nepf (2008) with minor corrections and modifications.

2.1 Introduction

Convective water exchange produced by spatial heterogeneity in water temperature plays an important role in the transport of nutrients and other substances, in particular between the littoral and pelagic regions of surface water bodies (Adams and Wells, 1984; James and Barko, 1991; James *et al.*, 1994; James and Barko, 1999; MacIntyre *et* al., 2002; Horsh and Stefan, 1988). Most commonly, temperature differences develop between shallow and deep regions when the same incoming solar radiation is distributed over different depths. This process has been studied in a triangular cavity both numerically (Farrow and Patterson, 1993) and experimentally (Lei and Patterson, 2002). Farrow (2004) extended this work to arbitrary bathymetry and described the transient and steady components of the flow, as well as the pattern of reversing flow that is generated by the diurnal cycle of heating and cooling. Under weak wind conditions, these flows control the flushing of littoral regions, reducing the flushing time by several orders of magnitude from turbulent diffusion alone. Similarly, the presence of phytoplankton can affect the penetration of irradiance into the water column, so that spatial heterogeneity in phytoplankton, or other sources of turbidity, can also produce density gradients (Edwards *et al.*, 2004). Coates and Patterson (1993) used scale analysis supported by experiment to describe the flow generated when an opaque layer, representing a region of high turbidity, shelters the water column.

Shading associated with aquatic macrophytes can also influence local water temperature (e.g. Chimney *et al.*, 2006; Ultsch, 1973). Lightbody *et al.* (2008) observed that day-time temperatures within the marsh region of a constructed wetland remained, on average, 2.0 degrees cooler than the open areas of the same wetland. Similarly, water temperature within a stand of the emergent *Schoenoplectus acutus* and *S. californicus* was as much as 2.5 degrees lower than within the nearby open water (Sartoris *et al.*, 2000). Shading by floating vegetation and the resulting convection has been studied by Coates and Ferris (1994). They observed exchange flows of $O(1)\text{mm} \cdot \text{s}^{-1}$ beneath mats of water fern (*Azolla*) and duckweed (*Lemna perpusilla*). A thin root layer beneath the floating macrophytes displaced the flow downward,

indicating a modifying influence of vegetative drag. But, this effect was not quantified in the study. In this paper, we consider rooted vegetation, which, in addition to generating temperature difference, provides drag over the entire flow domain, which should significantly alter the flow response.

A lake is generally divided into the pelagic zone, the region of open water, and the littoral zone, where rooted vegetation exists. The littoral zone is further divided into several regions based on the distribution of aquatic vegetation. The upper infralittoral zone is occupied mainly by emergent vegetation. The middle infralittoral zone is occupied by floating-leaved rooted vegetation. The lower infralittoral zone contains submersed rooted vegetation. The results of this paper apply mostly to the middle and upper infralittoral zone, where vegetation exists throughout the water depth. The impact of the submersed vegetation is discussed briefly in section 5.

To model the impact of littoral zone vegetation on density-driven exchange flow, we must characterize the vegetative drag. Several models for vegetative drag have been considered in the literature. In a numerical study, Horsch and Stefan (1988) modeled vegetative drag as an enhanced viscosity. Drag characterizations based on porous media flow have also been used (Oldham and Sturman, 2001). However, vegetative drag is most commonly modeled using a quadratic law, e.g. as in Burke and Stolzenbach (1983), Mazda *et al.* (1997) and Nepf (1999). The canopy drag coefficient, C_D, must be determined empirically. For solid volume fraction, ϕ, up to 9%, the drag coefficient, C_D, may be estimated by the empirical expression for isolated cylinders (White, 1991)

$$C_D \approx 1 + 10.0Re^{-2/3}, \tag{2.1}$$

where Re is the cylinder Reynolds number and is given by

$$Re = \frac{u_v d}{\nu}, \tag{2.2}$$

in which ν is the kinematic viscosity. For higher solid volume fraction, Tanino and Nepf (2007) measured C_D for random arrays up to $\phi = 35\%$ and $Re = 25$ to 685.

In this work, we conduct a lock-exchange experiment, in which the density difference between open and vegetated region is constant. This is a simplification of the field situation in which the density difference varies over the course of the diurnal heating. However, we will show that the set-up, or transient, time scale for the exchange flow is short compared to the time scale of diurnal temperature variation, so that this simplification is justified in evaluating velocity scales. In section 2.2, we present theory that predicts the velocity in both the open and vegetated regions, as well as the total exchange rate between these regions. Section 2.3 introduces the experimental methods, including set-up, image acquisition and data analysis. In section 2.4, experimental results are presented and discussed. Section 2.5 connects the new model and lab observations to field conditions, exploring the range of exchange flow magnitude expected for different canopy density and solar forcing.

2.2 Theory

The lock-exchange experiment has been widely used to study exchange flows in a laboratory setting. The exchange flow is produced by initially filling two reservoirs with fluids of different densities. The reservoirs are separated by a gate. When the gate is removed, the denser fluid propagates along the bottom while the lighter fluid propagates in the opposite direction along the top boundary. The flow evolves under a constant density difference.

The classic exchange current is depicted in (Fig. 2.1(a)). Benjamin (1968) found that, under the condition of negligible momentum dissipation, the interface is essentially horizontal, *i.e.* each layer occupies half of the total depth, and each front travels at speed u_i, where the subscript 'i' indicates inertial conditions,'

$$u_i = \frac{1}{2}\sqrt{g'H}. \tag{2.3}$$

H is the total depth of water, and g' is the reduced gravity which is expressed as

$$g' = \frac{\rho_2 - \rho_1}{\rho_2} g, \tag{2.4}$$

where ρ_2 and ρ_1 are the densities of the heavier and lighter fluid, respectively, and g is gravity. Later, our observations show that the velocity in the open region is controlled by the inertial velocity scale given in Eq. (2.3).

Shin *et al.* (2004) extended Benjamin (1968)'s theory to cover different initial fluid depths. By considering the currents propagating in both directions in the energy balance, they derived a more general theory in which the depth of the propagating current, h, need not be $H/2$. Specifically, the speed of the front is given by

$$u_i = \sqrt{\frac{h}{H}\left(1 - \frac{h}{H}\right)}\sqrt{g'H}, \tag{2.5}$$

For the case $h = H/2$, Eq. (2.5) correctly reduces to Eq. (2.3).

Tanino *et al.* (2005) studied a lock exchange entirely contained within an array of circular cylinders of diameter d. The arrays consisted of N cylinders per bed area A. The array density was characterized by the frontal area of the cylinders per unit volume, a, and the porosity, n, which are expressed as

$$a = Nd/A, \tag{2.6}$$

$$n = 1 - (\pi/4)ad = 1 - \phi, \tag{2.7}$$

respectively. For convenience, we also define the solid volume fraction, ϕ, which is the ratio of total cylinder volume to the total volume. When the array is sufficiently dense, the exchange flow is controlled by the canopy drag and exhibits an interface that is inclined to the horizontal plane, rotating about its midpoint (Fig. 2.1(b)). The drag-dominated frontal velocity is (Tanino *et al.* 2005)

$$u_v = \sqrt{-\frac{2n}{C_D a} g' S \frac{H}{L}}, \tag{2.8}$$

where subscript v indicates parameters within the vegetation, C_D is the canopy drag coefficient discussed earlier. S is a scale constant that describes the interfacial slope in proportion to the geometric ratio H/L, where L is the frontal length, as shown in Fig. (2.1(b)). Eq. (2.8) was confirmed by experiment in Tanino *et al.* (2005), and the scale factor S was found to be 0.6.

Eq. (2.8) is valid only when inertia is negligible compared with the canopy drag, which was shown by scaling and experiment to occur when $C_D aL > 10$. Note that L is equal to zero at the start of the exchange ($t = 0$), and increases as the two fronts propagate away from the center, such that at early time $C_D aL \to 0$, and the exchange flow is controlled by inertia and evolves according to inertial theory.. As L increases, more fluid is brought into motion, and the contribution of canopy drag increases ($C_D aL$ increases) and u_v declines (Eq. (2.8)). In addition, C_D may be slowly varying as u_v varies (Eq. (2.1) and (2.2)). But, C_D varies much more slowly than L and within the time-scale of the experiments, C_D does not vary significantly.

In this work, we consider a new configuration in which only half of the tank, i.e. only one side of the lock, is occupied by a model canopy (Fig. 2.1(c)). Compared with Tanino *et al.* (2005), the new configuration is a better simulation of the field, where exchange flows are more likely to occur between a vegetated area and the open water, because of differential shading than to be contained wholly within the vegetation. When the gate is removed, we expect the exchange flow to be initially controlled by inertia. However, as the current goes deeper into the canopy, the total canopy drag grows and eventually dominates inertia. Once this occurs, the boundary conditions within the canopy match those considered in Tanino *et al.* (2005), and thus we expect that Eq. (2.8) will still be valid within the canopy, with the following modification. We define L_v as the length of front contained within the vegetation. From geometric considerations, we replace L by $2L_v$, so that the interface slope within the canopy is given by $SH/2L_v$ (Fig. 2.1(c)). Then, from Eq. (2.8), we predict that for the case of exchange flow between an open region and an canopy, that the velocity within the canopy will be

$$u_v = \frac{\mathrm{dL_v}}{\mathrm{dt}} = \sqrt{\frac{ng'HS}{C_D aL_v}}, \tag{2.9}$$

It is not known a priori whether the interface geometry and thus the scale constant will be the same as that found previously for exchange flow contained within an canopy, and so it will be determined by experiment.

Based on the visual observations reported in Section 4, once the flow has reached the drag-dominated regime, the interface between the inflow and outflow in linear within the canopy (Fig. 2.1(c)). Then, at any time, the total volume per unit width that has entered the vegetation, V_v, can be estimated from geometry (see shaded region in Fig. 2.1(c)), as

$$V_v = \frac{1}{2} L_v h_v, \tag{2.10}$$

where h_v is the thickness of the current entering the vegetation measured at $x = 0$ (Fig. 2.1(c)).

The length of the front in the array can be obtained by integrating Eq. (2.9),

$$\frac{2}{3} L_v^{3/2} = \sqrt{\frac{ng'HS}{C_D a}} (t - t_0), \tag{2.11}$$

in which t_0 is a reference time that corrects for the initial transient, i.e. t_0 is the time scale of the transition from inertia to drag-dominated flow. It is defined shortly.

Using Eqs. (2.10) and (2.11), we can write V_v as

$$V_v = \frac{1}{2} L_v h_v = \frac{1}{2} \alpha L_v H = \frac{1}{2} \alpha \left[\frac{3}{2} \sqrt{\frac{ng'HS}{C_D a}} (t - t_0) \right]^{2/3} H, \tag{2.12}$$

and α is given by

$$\alpha = \frac{h_v}{H}. \tag{2.13}$$

The value of α as well as the assumption that α is constant will be evaluated by experiment.

The volume discharge rate per unit width q_v is obtained by taking the time derivative of Eq. (2.12),

$$q_v = \frac{\alpha}{3} \left[\frac{3}{2} \left(\frac{ng'HS}{C_D a} \right)^{1/2} \right]^{2/3} (t - t_0)^{-1/3} H. \tag{2.14}$$

From Eq. (2.14), we can see that the total exchange rate q_v is a function of $C_D a$ and is thus controlled by drag provided by the vegetation. From conservation of mass, the total volume of water going into the canopy must be equal to the total volume intruding into the open region.

The transition time scale t_0 can be estimated from the momentum equation,

$$n\frac{Du}{Dt} = -n\frac{1}{\rho}\frac{\partial P}{\partial x} - \frac{C_D a u|u|}{2}, \tag{2.15}$$

in which P is the hydrostatic pressure, ρ is the mean fluid density, and $C_D a u|u|/2$ is the canopy drag. When the flow is just initiated, little fluid volume is in motion, making the total drag small. During this period, the flow is controlled by inertia and $\partial u/\partial t = 0$. As the exchange evolves, more fluid is brought into motion, and the effect of the drag increases. At some point the vegetative drag equals inertia, *i.e.*

$$nu\frac{\partial u}{\partial x} \sim \frac{C_D a u|u|}{2}. \tag{2.16}$$

Scaling $x \sim L_v$, the above equation gives the frontal length at which drag equals and then surpasses inertia,

$$L_v \sim \frac{2n}{C_D a}. \tag{2.17}$$

Because up to this length $u = u_i$, the time scale t_0 to reach L_v is $t_0 \sim L_v/u_i$, using Eqs. (2.3) and (2.17), the initial period of inertia flow is limited to the time

$$t_0 \sim \frac{\frac{2n}{C_D a}}{u_0} \sim \frac{4n}{C_D a\sqrt{g'H}} = 4\frac{n}{C_D a H}\sqrt{\frac{H}{g'}}. \tag{2.18}$$

2.3 Experimental Methods

To explore the impacts of vegetative drag on the velocity scale in the open and vegetated regions, a series of lock-exchange experiments were conducted in a 200.0cm × 12.0cm × 20.0cm Plexiglas tank with a horizontal bottom. The tank was separated into two regions of equal length by a removable gate which was 5mm thick. A thin

layer of felt was attached to the edge of the gate to form a seal, and two plexiglas blocks were attached on the top of the tank to guide the gate as it is pulled out vertically. A perforated PVC board was placed atop half of the tank. Dowels with diameter $d = 6$mm and length $l = 36.4$cm were pushed through the holes in the board and extended down to the bed. The holes in the board were randomly distributed, and when completely filled with dowels, the board produced a maximum stem density $a = 0.75\text{cm}^{-1}$, corresponding to $\phi = \pi ad/4 = 0.35$. Each of the holes was assigned a number, and a numerical program was used to randomly choose a subset of holes to create arrays of different densities. Here, we will consider cases with $\phi = 0$ to 0.35, which corresponds to the full range observed in field canopies (Kadlec, 1990). For example, the water lily (*Nymphaea Odorata*) has a typical diameter $d \approx 1$cm and $\phi \approx 0.01$ to 0.04. The most dense canopies are mangroves, which have $d \approx 4$ to 9cm and ϕ as high as 0.45 (Mazda *et al.*, 1997).

For most experiments, the canopy was filled with saltwater of density ρ_2, and the saltwater was dyed black or blue with food dye. The open region was filled with fresh tap water with a density ρ_1 smaller than ρ_2. In seven runs, the density difference was reversed, i.e. the lower density water was placed in the model array. The reversed cases were included for two reasons. First, the effects of bottom drag can be examined by comparing the normal and reversed cases with identical experimental parameters, e.g. same ϕ, ρ_1 and ρ_2. Second, the reversed condition occurs during night time when the heat in the open water radiates faster than that in the vegetated region, where emergent vegetation tends to diminish radiation losses (O'Sullivan and Reynolds, 2004). The reversed cases are marked with an asterisk in Table. 1. The density of water in each region was measured with a hydrometer with a precision of $\pm 0.0005\text{g} \cdot \text{cm}^{-3}$.

From Eq. 2.9, the non-dimensional velocity is

$$\frac{u_v}{\sqrt{g'H}} = \sqrt{\frac{n}{C_D a H}} \sqrt{S \frac{H}{L_v}}. \tag{2.19}$$

The experimental conditions were scaled to field conditions based on the velocity scale

$\sqrt{g'H}$, as well as the dimensionless drag $C_D aH/n$. In the field, a typical water depth for vegetated zones is in the range of $H = 10$ to 100cm, and a typical $g' \leq 1.0\text{cm} \cdot \text{s}^{-2}$ (based on temperature differences observed by Dale and Gellepie, 1976; James and Barko, 1991; Nepf and Oldham, 1997; Lightbody *et al.*, 2008). Thus, in the field $\sqrt{g'H}$ is in the range of $O(1)$ to $O(10)$ cm/s. In our experiments, the depth of water H, as well as the density of the salt water ρ_2, were chosen so that the velocity scale $\sqrt{g'H}$ in the laboratory fell within these field conditions. The dimensionless parameter that describes the canopy drag, $C_D aH/n$, was also matched to field conditions. With a reasonable simplification that $C_D = 1$ for sparse canopies ($\phi < 0.09$) but increases to $C_D = 3$ for very dense canopies ($\phi \geq 0.3$) (Tanino and Nepf, 2007), we estimated that $C_D aH/n$ ranges from $O(1)$ (e.g. water lily) to $O(100)$ (e.g. mangrove). In our experiments, the dimensionless drag covered a similar range, from 0.6 to 76 (Table. 2.1).

When imaging the exchange flow, the back of the tank was illuminated with four 40W fluorescent lights to enhance contrast. Tracing paper was used to diffuse the light. When the gate was removed, the salt water flowed along the bottom due to its larger density, while the fresh water flowed along the free surface. The whole experiment was captured by a Pulnix TM-6702 CCD camera with a resolution of 640×480 at a rate of 1fps. The CCD camera was mounted on a tripod in front of the tank, and the distance between the camera and tank was set as long as possible (5.4m) to minimize the parallax error (less than 1%).

The images were analyzed using the Matlab image processing toolbox. First, the images were converted from gray-scale to binary pictures. The threshold was manually chosen such that the binary images gave the best agreement with the original images. At each longitudinal position, the height of the interface was identified at the transition from white to black pixels. For the cases with solid volume faction ϕ up to 9%, the toe velocity in each region was calculated from the displacement of the toe at both the bed and the free surface between two consecutive images, divided by the time interval between these two images. For the cases with high solid volume fraction, i.e. $\phi > 0.09$, the flow in the canopy could not be imaged clearly with the camera,

because too much of the domain was blocked by cylinders. The velocity of the toe for these cases was estimated by visual tracking and manually timing the movement of the toe between fixed points with a stop watch. The velocity in the vegetation, u_v, was then used to calculate the drag coefficient from Eq. (2.1) and the empirical relations given in Tanino and Nepf (2008).

At each time point, the total volume intruding into the open region per unit width, V_o, was estimated by integrating the interface over $x < 0$. A similar estimate was made for V_v, the volume intruding into the vegetation, with corrections made for ϕ. The discharge rate q_o (or q_v) was calculated as the difference of V_o (or V_v) between two consecutive images divided by the time interval. The discharge rate q_0 was measured in every case ($\phi = 0$ to 0.35), but q_v could only be measured up to $\phi = 0.09$. At higher solid volume fraction, the visual obstruction from the array introduced too much error to provide a reliable estimate of V_v.

2.4 Results

After the removal of the gate, the gravity currents start to propagate. Fig. 2.2 shows the temporal evolution of the interface in both the open region and the canopy for case 26. The time interval between each curve is four seconds. At the first time step (heavy line in Fig. 2.2(a)), the interface resembles that in a classic inertial exchange, with the two currents having nearly equal depth ($h/H \approx h_v/H \approx 0.5$). A pronounced head is also present at the toe of each current. Shortly after, however, the exchange flow deviates from the classic inertial evolution. The toe of the current in the open region continues to propagate at a constant speed, but the toe in the canopy decelerates. In the open region the top of the outflowing gravity current is horizontal, as in a classic inertial exchange, but the thickness of the current is less than that observed in a classic lock exchange, *i.e.* $h/H < 0.5$. In the vegetative region, as the current intrudes further into the canopy, the height of the current at the toe decreases and the interface gradually becomes linear. At the fifth profile ($t = 20$sec), the interface is clearly linear within the vegetation (Fig. 2.2(b)). From Eq. (2.18), the transition

to drag-dominated flow occurs at $t_0 = 6$ sec for this case. However, linear profile is expected to be developed after t_0, i.e. after the transition to the drag-dominated regime, because the interface has some memory of its initial shape.

Note that undulations are observed along the interface in the open region. These reflect mixing and overturning that results from the strong shear along the interface between the inflow and outflow. Similar mixing and undulation has been observed in free gravity currents (*e.g.* Fig. 9 in Shin *et al.*, 2004). Within the canopy, however, the presence of the vegetative drag suppresses the instability leading to overturning, as discussed in White and Nepf (2007) (*e.g.* see Fig. 21 in that paper), and no mixing is observed along the interface within the canopy. Finally, at the transition to drag-dominated flow, the depth of the current intruding into the vegetation, h_v, has increased to $0.62H$, where it remains for the duration of the experiment. The same progression was seen for each value of $C_D aH/n$, with the final $\alpha = h_v/H = 0.70 \pm 0.05$ (data not shown, standard deviation across the observed cases). There was no correlation between α and ϕ.

The length of the gravity current in the open region increases linearly with time, indicating that the toe velocity in the open region, i.e. the slope of $x_o(t)$, is constant (Fig. 2.3). The velocity of the toe in the canopy, however, decreases over time, due to increasing drag ($C_D aL$), i.e. the slope of $x_v(t)$ is decreasing. The same development is observed in all cases. As an example, the positions of the toe in the open region and in the vegetation, x_o and x_v, respectively, normalized by the water depth, H, are shown for case 26 (Fig. 2.3). The time, t, is normalized by $\sqrt{g'/H}$.

The toe velocity in the open region, u_o, is not a strong function of canopy drag parameterized by $C_D aH/n$ (Fig. 2.4(a)). For the standard cases, *i.e.* open region gravity current at the bed (solid circle), $u_o/\sqrt{g'H} = 0.40 \pm 0.04$ (standard deviation). For the reversed cases, i.e. open region gravity current at the surface (open circle), $u_o/\sqrt{g'H} = 0.47 \pm 0.05$ (standard deviation). For gravity currents propagating along the bed (Fig. 2.4, solid circle), the observed Froude number, $F_H = u_o/\sqrt{g'H}$, is smaller than the theoretical prediction for inertial gravity currents, $F_H = 0.5$ (Benjamin, 1968). However, a diminished Froude number has been observed in other studies as

well, e.g. $F_H = 0.42$ (Shin *et al.*, 2004) and is attributed to the viscous drag associated with the bed. For the reversed cases, in which the gravity current propagates along the free surface (shown as open circles in Fig. 2.4), the Froude number is actually greater than 0.5 for some cases. Simpson (1997) found similar results in an open rectangular tank, observing a Froude number of 0.59 for the surface current.

The fact that the the velocity of the open current does not change with canopy drag is somewhat surprising, because the depth of the current in the open region, h, decreases with increasing canopy drag $C_D aH/n$ (Fig. 2.4(b)). One might expect u_o to adjust following Eq. (2.5), but a shift in velocity scale is not observed until h grows quite small, $h/H < 0.2$, which corresponds to $h \leq 2$ cm in these experiments (Fig. 2.4(c)). The constant value suggests that the current propagating into the open region has its speed set by the initial inertial conditions, u_i, *i.e.* Eq. (2.3). The data suggest that u_o may become sensitive to array drag for $C_D aH/n > 10$, declining as drag increases. For these cases, the initial inertial transient may be too short to imprint upon the the frontal velocity. Indeed, for these cases, $t_0 < 0.5$ sec. In addition, the shallowness of the layer for $C_D aH/n > 10$, as can be seen in Fig. 2.4(b), enhances the bed drag, i.e. as h decreases, the bottom shear stress $\tau_w \sim \rho \nu u_o/h$ increases. For $h < 2$ cm, the bed stress may become sufficiently significant to slow the current.

Next, we consider the current propagating into the model canopy. When the flow has reached the drag dominated state, the front velocity, u_v, decelerates slowly due to the drag exerted by the cylinders. The toe velocity in the canopy is then given by Eq. (2.9). The scale constant S in Eq. (2.9) can be determined by fitting the observed frontal length, L_v, to Eq. (2.11). The following normalization collapses all the case, indicating this scaling is universal.

$$\hat{L}_v = (\frac{3}{2})^{2/3} L_v (\frac{nH^2}{C_D a})^{-1/3}, \tag{2.20}$$

$$\hat{t} = t\sqrt{\frac{g'}{H}}, \tag{2.21}$$

Using Eq. (2.20) and (2.21), Eq. (2.11) can be written as

$$\hat{L}_v^{3/2} = \sqrt{S}(\hat{t} - \hat{t}_0). \tag{2.22}$$

Eq. (2.22) implies that $\hat{L}_v^{3/2}$ is proportional to $(\hat{t} - \hat{t}_0)$, and the constant of proportionality is $\sqrt{S}$. Here, we remark that t_0, as predicted by Eq. 2.18, is in the range of 0.06 sec to 6 sec in our experiments, i.e. the transition from inertia to drag-dominated regime is short compared to the duration of the experiment, $O(50)$, even for the very sparse cases.

Fig. 2.5 shows the evolution of $\hat{L}_v$ with $\hat{t}$ for ϕ ranging from 0.03 to 0.09. Although experiments with ϕ as high as 0.35 have been conducted, the temporal evolution of L_v can not be detected with sufficient resolution for ϕ higher than 0.09. The scale constant S can be obtained by evaluating the slope of the curves (which is essentially $\sqrt{S}$) in Fig. 2.5. The value of S falls between 0.5 to 0.7, with no correlation with ϕ over this range. Tanino *et al.* (2005) obtained a similar value, $S = 0.6$, in their study of exchange flow contained within a uniform canopy (see Fig. 2.1(b)). Given that no correlation with ϕ is detected, we anticipated that $S = 0.6$ will apply at higher ϕ as well.

In the drag dominated regime, the total volume of water entering the cylinder array is given by Eq. (2.12), which can be written in the following dimensionless form,

$$\hat{V}_v = \alpha(\hat{t} - \hat{t}_0)^{2/3}, \tag{2.23}$$

in which $\hat{V}_v$ is given by

$$\hat{V}_v = \frac{V_v}{\frac{1}{2}\left[\frac{3}{2}(nH^2S/C_Da)^{1/2}\right]^{2/3} H}. \tag{2.24}$$

Since the volume discharge into the open region, V_o, equals the volume discharge into the array, V_v, and V_o can be measured more reliably, the discharge into the open region has been used to evaluate the relationship shown in Eq. 2.23. $\hat{V}_o$ versus $\hat{t}$ is shown in Fig. 2.6 for the cases with ϕ ranging from 0.03 to 0.14. For the cases with

$\phi = 0.20$ or 0.35, the difficulty in visualizing the flow within canopy makes it difficult to estimate C_D with less than a factor of 2 uncertainty. Since the normalization is sensitive to C_D, these cases are excluded. Although the data do not collapse perfectly, V_o in all cases follow the same trend, specifically non-linear in time. The best fit for the experimental data is

$$\hat{V}_v = (0.63 \pm 0.18)[\hat{t} - (0.1 \mp 1.1)]^{0.74 \pm 0.08}, \tag{2.25}$$

The exponent, (0.74 ± 0.08), agrees within uncertainty with the theoretical exponent, of 2/3 given in Eq. (2.12). In addition, the fitted scale constant, $\alpha = 0.63 \pm 0.18$, agrees with the observed value of $\alpha = h_v/H = 0.70 \pm 0.05$.

The exchange rate, q_o, can be found by taking the time derivative of V_o. Given that $q_o \equiv q_v$, Eq. (2.14) can be written in dimensionless form,

$$\hat{q}_o = \left[\frac{\alpha}{3}(\frac{3}{2})^{2/3} S^{1/3}\right] (C_D a H/n)^{-1/3} (\hat{t} - \hat{t}_0)^{-1/3}, \tag{2.26}$$

in which $\hat{q}_o$ is given by

$$\hat{q}_o = \frac{q_o}{(g' H^3)^{1/2}}. \tag{2.27}$$

Fig. 2.7 shows the variation of $\hat{q}_o$ as a function of $C_D aH/n$ for all cases ($\phi = 0.03$ to 0.35. For comparison among different cases, $\hat{q}_o$ was estimated at the dimensionless time, $(\hat{t} - \hat{t}_0) = 10$, for each case. The solid line represents the theoretical prediction (Eq. (2.26)) evaluated at $(\hat{t} - \hat{t}_0) = 10$, and with $S = 0.6$, $\alpha = 0.7$ which were found experimentally, as shown in Figs. 2.5 and 2.6, respectively. The dashed lines are the upper and lower bounds of the theoretical prediction based on the uncertainties in S and α. Note that although S and α were obtained by fitting the data for $\phi \leq 0.09$ and $\phi = 0.14$, respectively, the prediction for $\hat{q}_o$ using these values agrees with the observation, even for the cases with $\phi = 0.2$ and 0.35 (see data points for $C_D aH/n > 10$ in Fig. 2.7). This provides confirmation that $S = 0.6$ and $\alpha = 0.7$ does not change at higher solid volume fraction ϕ.

Recall that the toe velocity in the open region is constant in time (Fig. 2.3) but

the discharge rate decreases with time (Fig. 2.6), so that we expect the thickness of the current in the open region to decrease with time. Specifically, $h = q_o/u_o$, which in non-dimensional form is,

$$\hat{h} = \frac{h}{H} = \frac{1}{0.4}\left[\frac{\alpha}{3}(\frac{3}{2})^{2/3}S^{1/3}\right](C_D aH/n)^{-1/3}(\hat{t}-\hat{t}_0)^{-1/3}. \tag{2.28}$$

The time variation of h for case 30 is shown in Fig. 2.8. The good agreement between the observed h and the estimated q_o/u_o suggests that the velocity along the entire intrusion is equal to the toe velocity u_o. A similar result was observed in inertial currents by Lowe *et al.* (2002). The solid line is the theoretical prediction from Eq. (2.28), in which the input parameters are again $S = 0.6$, $\alpha = 0.7$. The dashed lines are the upper and lower bounds based on the uncertainties in S and α. In addition, the theory given by Eq. (2.28) provides a good prediction to the temporal variation of $\hat{h}$ (Fig. 2.8). Note that the theory breaks down when $(\hat{t}-\hat{t}_0)$ approaches zero due to fact that, initially, the flow is controlled by inertia, such that theoretical value does not go back to 0.5 as $(\hat{t}-\hat{t}_0)$ goes to zero.

2.5 Field Applications and Limitations

Using the theoretical and empirical relations developed in Section 4, we now consider the evolution of the exchange flow in real field systems. During the daytime, due to shading by emergent vegetation, water within a canopy absorbs less solar energy than the adjacent open water. The density difference associated with this differential absorption of energy will drive an exchange flow. This situation is sketched in Fig. 2.9(a). The differential heating associated with vegetative shading was recently observed in a wetland (Lightbody *et al.*, 2008). The water depth H was 0.5m. The marsh grass, *Zizaniopsis Miliacea*, had a solid volume fraction $\phi = 0.1$ and the diameter of the stem was 3 cm. The average diurnal variation in water temperature in the canopy and in the adjacent open water is shown Fig. 2.9(b). The temperature difference was nearly zero from midnight to early morning, then increased gradually

to reach the peak value of $\triangle T = 2$ degrees Celsius around 4PM, and finally decreased to zero again at midnight. This temperature record will be used to estimate the density-driven exchange flow, as it varies over the course of the day. The drag coefficient, C_D, is assumed to be equal to 1, which is reasonable for this solid volume fraction. The transient time-scale t_0 is estimated from Eq. 2.18 to be less than 50 sec, which is short compared to the time-scale of the thermal variation in the daily cycle. Consequently, the inertial transient can be neglected, and a quasi-steady estimate of flow should be reasonable. We divide the period (from 10AM to midnight) into one-hour subdivisions and apply Eq. (2.11) to estimate the intrusion length L_v at the end at each hour. The volume discharge V_v occurring in each hour in response to the temperature variation in Fig. 2.9(b) is shown in Fig. 2.9(c). In a single day the exchange flow can penetrate approximately 100m into the vegetation. This suggests that if the band of vegetation is less that 100m in width, it can be fully flushed each diurnal cycle. The average discharge rate per unit width during the twelve hour cycle is 1.7 m^3/m hr, which is the same of order of magnitude as the mean flow through the vegetative band of this wetland, 1.8 m^3/m hr, as measured by Lightbody *et al.* (2008). Therefore, the thermally-driven exchange flow adds significantly to the total flushing in this wetland.

When applying our model to field conditions, we assume that the flow structure is two-layer, even though the stratification is likely to have a more continuous vertical structure. Many studies in the field, lab and numerical domain have considered exchange flows driven by differential heating. In each case, the temperature profiles are forced by the absorption of solar radiation, which result in continuous stratification. However, in each case the resulting flow is a two-layer exchange (Andradottir and Nepf, 2001; Oldham and Sturman, 2001; Coates and Ferris, 1994; Coates and Patterson, 1993; and Farrow and Patterson, 1994). Multiple intrusions have not been observed. Therefore, the two-layer exchange observed in our study appears to be consistent with what would be observed in the field.

To evaluate the potential impact to a broader range of systems, we have repeated the above scenario for 1 m deep water and for a range of canopy densities, representing

the most sparse to most dense canopies observed in the field. The intensity of radiation is assumed to vary over the day, with peak radiation intensity $I_0 = 400, 600$ and 800 $\mathrm{Wm^{-2}s^{-1}}$. This produces variation in ΔT of the same form as shown in Fig. 2.9, with peak value ΔT_0. Fig. 2.10 shows the predicted average discharge rate over a daily cycle, as a function of $C_D aH/n$ and I_0 (ΔT_0). This figure can be used to compare to other flushing mechanisms, and thus it provides an easy way to evaluate the significance of the density-driven exchange flow in different systems.

The spatial extent of flushing from within a canopy is given by the maximum penetration of the front, L_v. For the cases shown in Fig. (2.10), the maximum L_v ranges from $O(400)$m for low density canopies ($C_D aH/n = 1$) to $O(100)$m for high density canopies ($C_D aH/n = 100$). It is useful to compare this length scale with the spatial footprint of exchange associated with wind-driven currents. First, consider wind-driven currents running parallel to a canopy edge (Fig. 2.11(a)). As described in White and Nepf (2007), these currents penetrate a distance into the canopy of scale $(C_D a)^{-1}$ and therefore contribute to canopy flushing only over this length-scale. For typical field values, $(C_D a)^{-1}$ is on the order of 1 m or less. Second, consider wind-driven currents approaching perpendicularly to the canopy edge (Fig. 2.11(b)). Assuming the canopy blocks all wind-stress at the water surface, the flow into the canopy is quickly decelerated by the canopy drag over the length-scale $(C_D a)^{-1}$, *e.g.* as in Jackson and Winant (1983). The associated surface set-up can drive an exchange flow near the edge of the canopy. In both scenarios, wind-driven currents can promote flushing only over scales of order 1 m. Whereas density-driven currents can promote flushing over 10's to 100's m. Thus, thermally-driven exchange is likely to be the dominant vehicle for flushing of littoral regions with dense vegetation.

A limitation of the model discussed here is that it does not explicitly account for bed drag in the open region. In the field, flow exiting a region of sheltering, emergent vegetation may encounter submerged vegetation, which would enhance the bed drag. Based on our experimental observations, the velocity in the open region may be diminished because of this bed drag. However, the total discharge rate would still be controlled by the emergent canopy drag and therefore unchanged. A slower velocity in

the open region due to bottom drag would simply cause the thickness of this current to increase. In addition, because of the diminished velocity , material flushed from canopy will not be distributed as far from the vegetation edge. Although unlikely, if the bed drag in the open region becomes comparable to that in the emergent canopy, the conditions will revert to those described by Tanino *et al.* (2005), with total exchange dependent upon the drag throughout the entire flow domain.

Finally, the present work is limited to the condition of uniform temperature over depth. Under field conditions, the absorption of solar radiation in water decreases exponentially away from the surface according to Beer's Law, and heating may not occur over the full depth. If solar radiation penetrates less than the water depth, we expect, based on Coats and Patterson (1993) and Coates and Ferris (1994) that the vertical extent of the resulting exchange current will scale on the extinction depth. However, the velocity scales should follow a dependence on canopy drag similar to that described here. In addition, the present work assumes that the solid volume fraction of aquatic vegetation ϕ is constant over water depth. Vertical structure in ϕ would impact the vertical structure of the velocity, but to first order, the total exchange should still scale on the depth-averaged solid volume fraction ϕ, as reflected in the depth-averaged $C_D aH/n$.

2.6 Conclusion

The density-driven exchange flow between open water and adjacent vegetation has been studied using a lock exchange experiment. Unlike an classic lock exchange or the exchange flow subject to uniform drag, the exchange flow occurring between two regions of dissimilar drag,, *i.e.* canopy and open water, is asymmetric. The gravity current in the open region moves at a constant speed set by the initial inertial condition, while the speed of the current in the vegetative region is controlled by the canopy drag and decreases with time. The total discharge rate is also controlled by the vegetative drag, decreasing with increasing canopy drag and also decreasing slowly with time. Application of the theoretical model to typical field conditions suggests

that thermally-driven exchange is likely to be the dominant process in flushing littoral bands of vegetation.

Table 2.1: Summary of experimental conditions and model parameters. Cases with $*$ represent the reversed cases.

Run	ϕ	$g'(\pm 0.05)cm/s^2$	$H(\pm 0.1)cm$	$C_D aH/n$	$u_o(\pm 0.3)$cm/s
1	0.05	9.24	10.0	1.5	4.0
2	0.05	6.33	10.4	1.6	3.2
3	0.05	3.42	10.9	1.8	2.4
4	0.03	11.2	10.3	0.8	4.6
5	0.03	9.73	10.2	0.9	4.0
6	0.03	8.76	10.7	0.9	3.7
7	0.03	7.31	10.5	0.9	3.4
8	0.04	9.73	10.5	1.3	3.3
9	0.04	4.89	10.6	1.3	2.8
10	0.04	2.94	11.0	1.4	2.2
11	0.04	4.89	10.6	1.3	3.0
12	0.06	7.31	11.0	2.0	3.7
13	0.06	4.88	10.5	2.1	2.8
14	0.06	3.91	11.1	2.2	2.7
15	0.09	12.1	11.0	3.1	4.8
16	0.09	5.86	11.0	3.5	3.2
17	0.09	6.34	11.5	4.7	3.6
18	0.14	7.31	12.1	12	3.7
19	0.14	4.89	12.5	18	2.8
20	0	3.91	10.1	0	2.6
21	0.14	3.43	12.0	14	2.5
22	0	5.37	10.5	0	3.3
23	0.01	4.39	10.3	0.3	3.1
24	0.35	7.79	12.0	76	2.9
25*	0.03	4.88	10.1	0.9	3.4
26	0.03	4.88	10.2	0.9	3.0
27	0.03	6.82	10.0	0.9	3.6
28*	0.03	6.82	10.0	0.9	4.2
29*	0.06	3.42	10.0	2.0	3.0
30	0.06	3.42	10.0	2.0	2.5
31	0.06	6.34	10.0	1.9	3.7
32*	0.06	6.34	10.0	1.9	4.1
33*	0.05	3.91	10.0	1.6	2.7
34	0.05	3.91	10.0	1.6	2.7
35	0.05	3.42	10.1	1.7	2.3
36*	0.05	3.42	10.0	1.6	2.6
37	0.35	5.86	10.0	71	2.4
38*	0.35	5.86	10.0	71	3.0
39	0.20	4.40	10.0	27	2.2
40	0.20	8.77	10.0	23	2.9
41	0	4.40	10.0	0	2.7

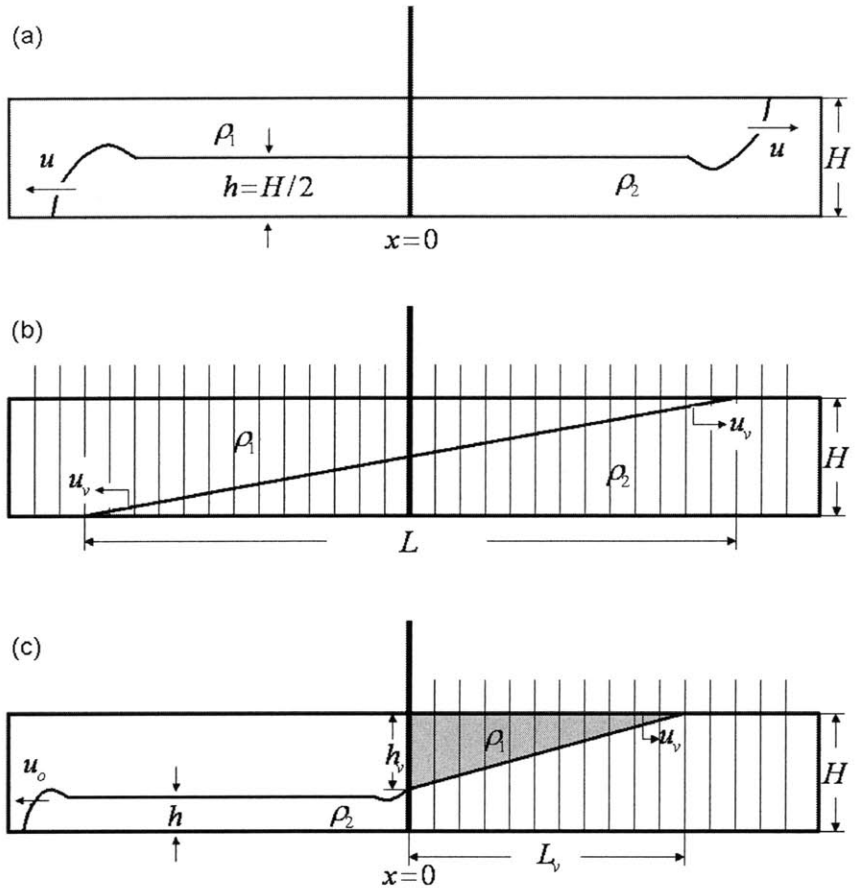

Figure 2.1: Interface profiles for (a) classic exchange flow in an unobstructed domain; (b) exchange flow within a domain of uniform obstruction; (c) exchange flow between a region of obstruction (canopy) and open water. In all cases, $\rho_2 > \rho_1$.

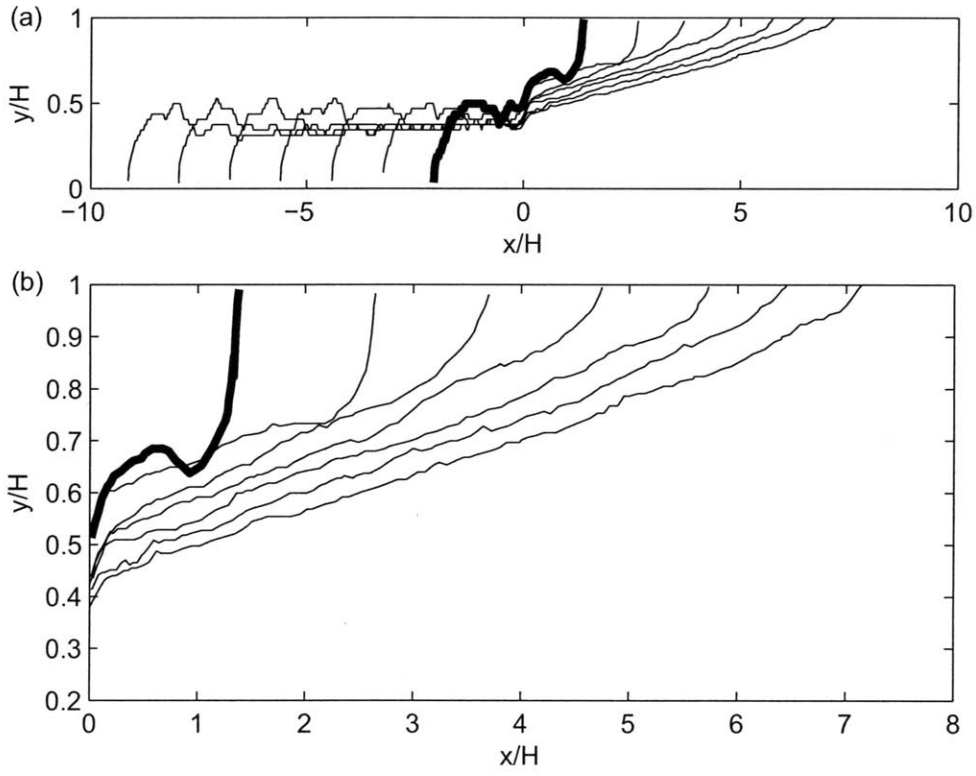

Figure 2.2: Evolution of the entire interfacial profile (a) and also a close-up of the region within the vegetative model (b) for case 26. The time interval between each curve is 4 sec. Cylinder array occupies $x > 0$.

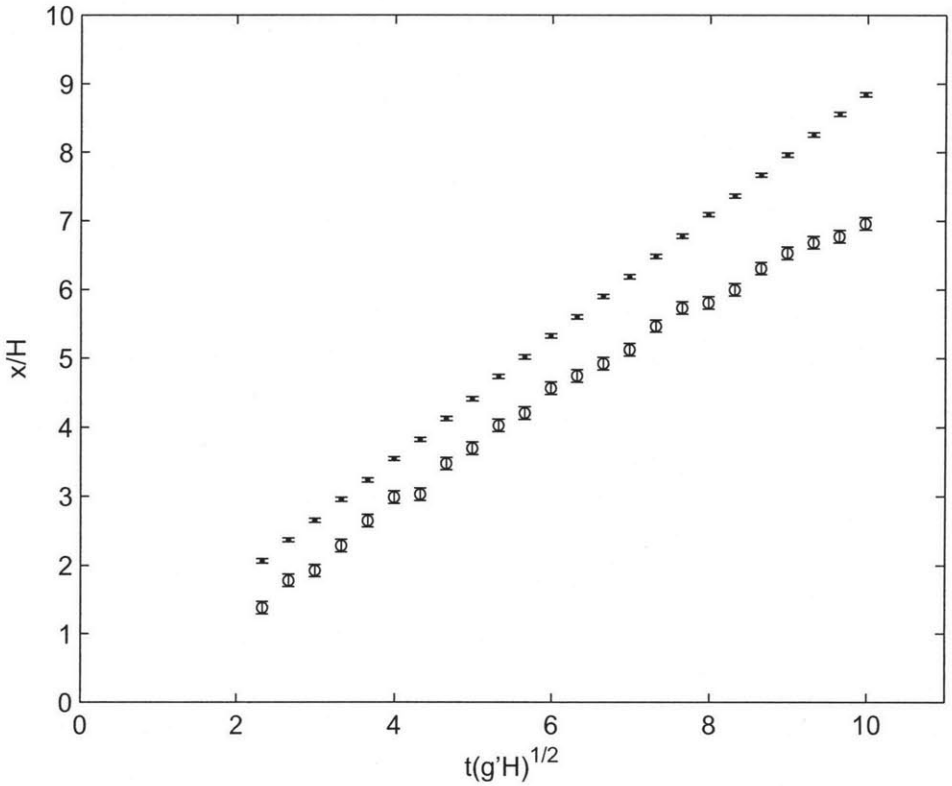

Figure 2.3: Temporal evolution of the toe position in the open region x_o ($\cdot$) and the vegetated region x_v ($\circ$) for case 26.

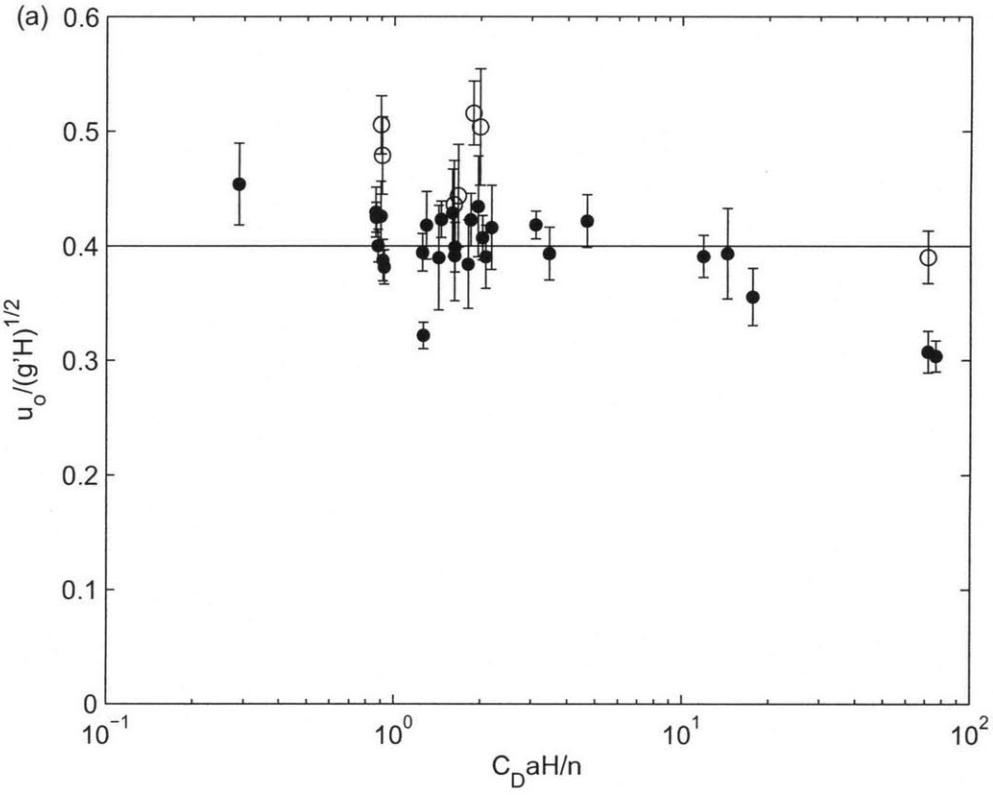
(a)
0.6
0.5
0.4
0.3
0.2
0.1
0
$u_o/(g'H)^{1/2}$
10^{-1}
10^{0}
10^{1}
10^{2}
$C_D aH/n$

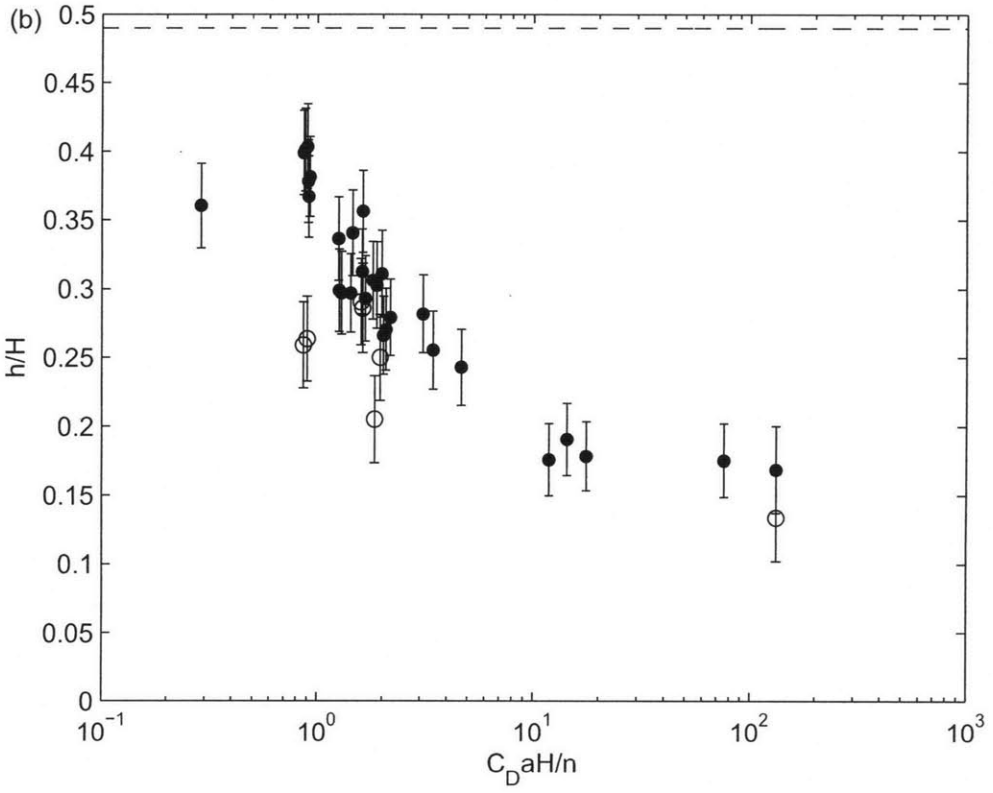
(b)
0.5
0.45
0.4
0.35
0.3
0.25
0.2
0.15
0.1
0.05
0
h/H
10^{-1}
10^{0}
10^{1}
10^{2}
10^{3}
$C_D aH/n$

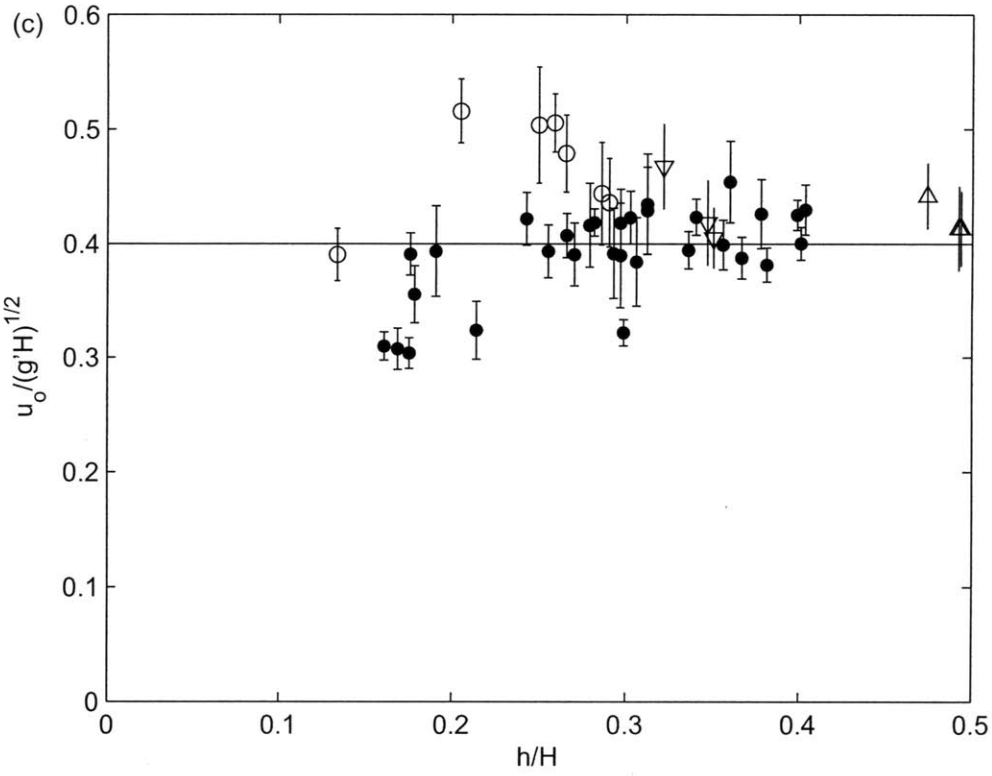

Figure 2.4: (a). Normalized toe velocity in the open region, $u_o/\sqrt{g'H}$ versus canopy drag, $C_D aH/n$. The mean of the standard cases (solid circle)is shown by the horizontal line. (b). The variation of the normalized thickness of the current in the open region, h/H, with $C_D aH/n$. The dashed horizontal line is the thickness of the current along the bottom for the cases with $\phi = 0$. (c). The variation of the normalized toe velocity in the open region $u_o/\sqrt{g'H}$ with h/H. In each subplot, the open circles represent the reversed cases, i.e. current propagating into the open region at the surface, which are denoted by an asterisk in Table. 2.1. The upward- and downward-facing triangles represent current along the bottom and surface, respectively for the classic cases ($\phi = 0$).

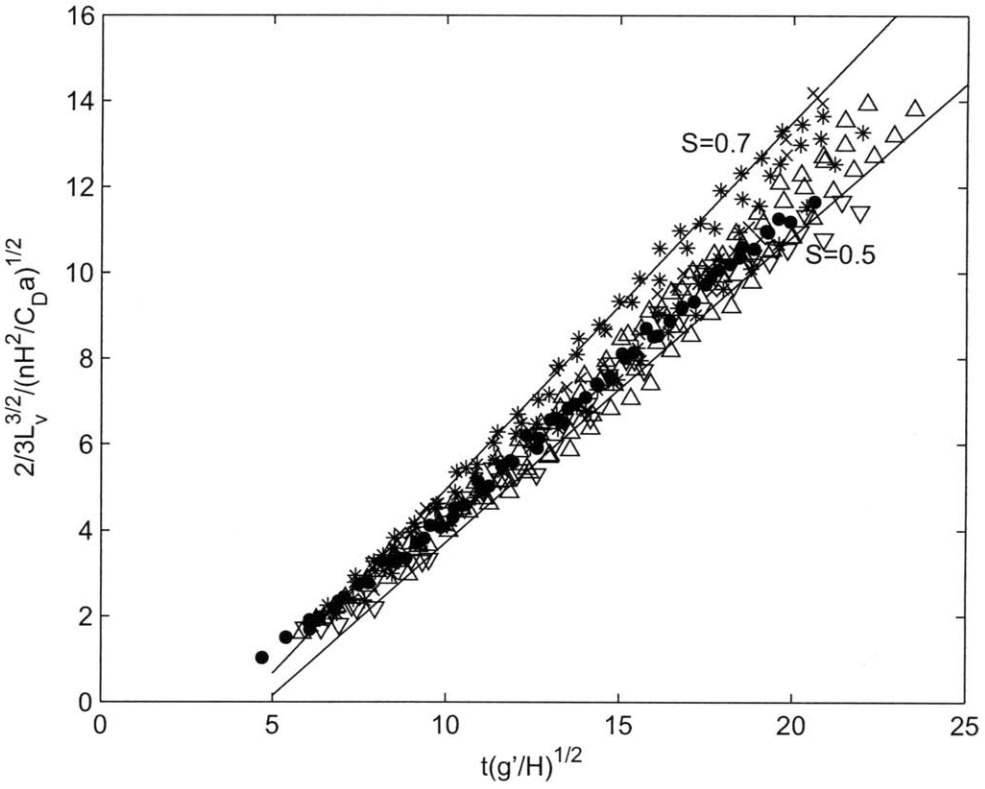

Figure 2.5: Temporal variation of the length of the current, L_v, within the array for different solid volume fraction: $\phi = 3\%(\bullet)$, $\phi = 4\%(\triangledown)$, $\phi = 5\%(\triangle)$, $\phi = 6\%(*)$, $\phi = 9\%(\times)$. Eq. (2.22) is plotted as a line for $S = 0.5$ and 0.7.

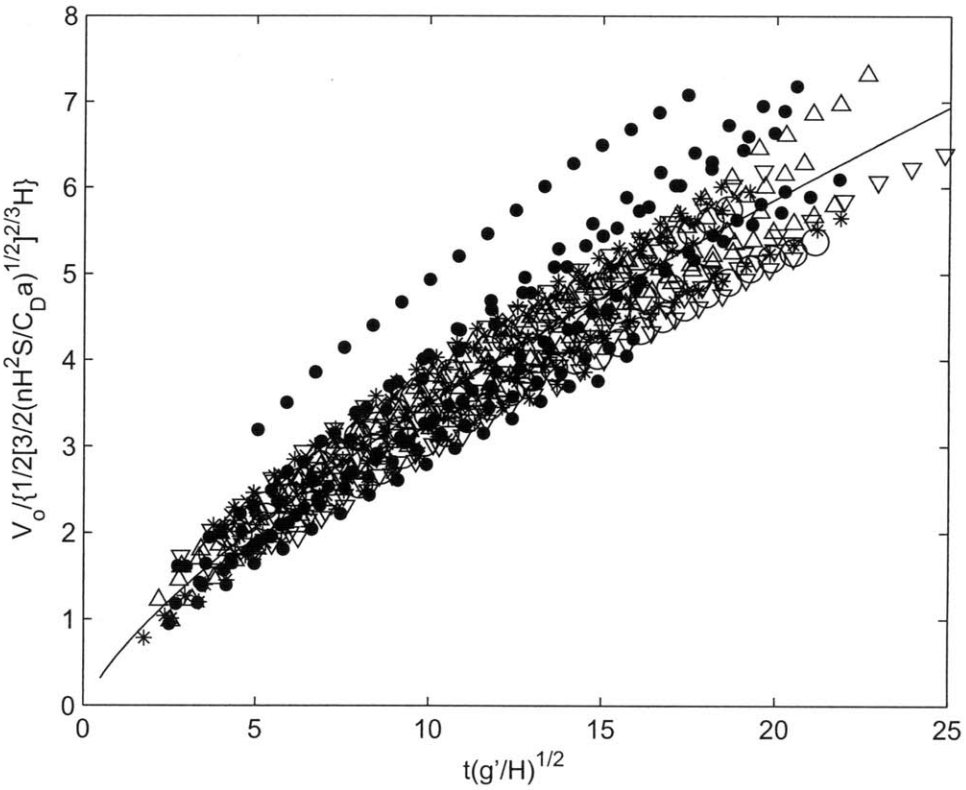

Figure 2.6: Temporal evolution of the total volume discharge per unit width for different solid volume fraction: $\phi = 3\%(\bullet)$, $\phi = 4\%(\triangledown)$, $\phi = 5\%(\triangle)$, $\phi = 6\%(*)$, $\phi = 9\%(\times)$, $\phi = 14\%(\circ)$. The solid line is the best fit for all the data, which is given by Eq. 2.25. The uncertainty for normalized V_o is 20%.

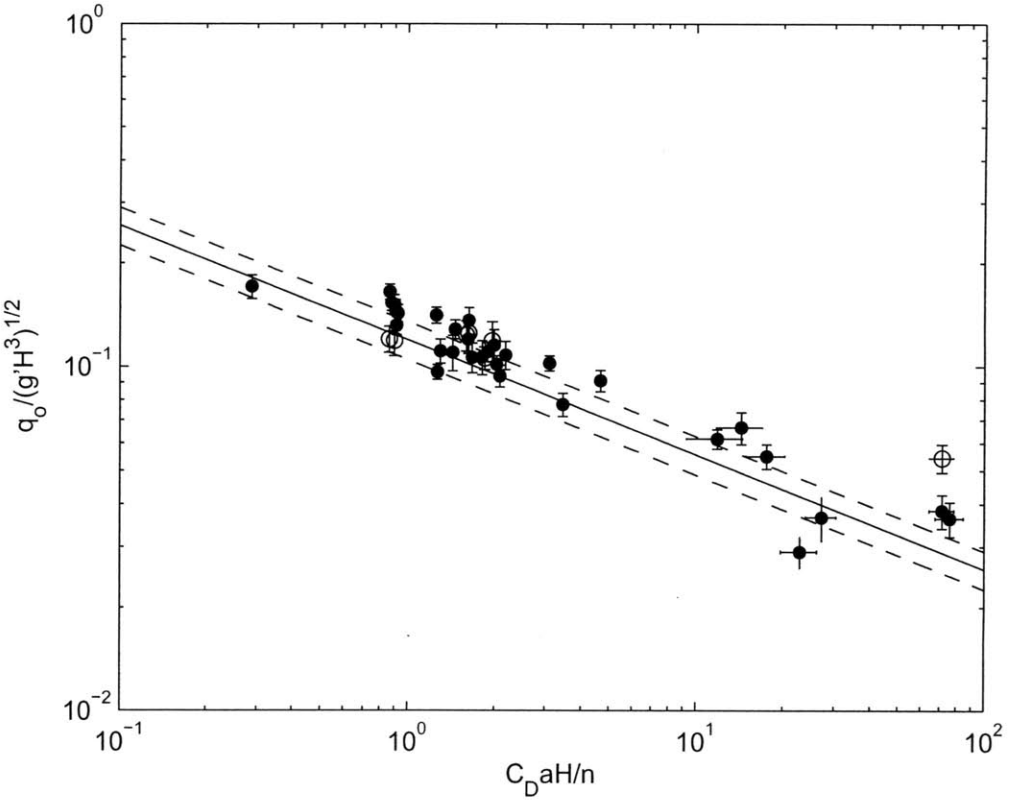

Figure 2.7: The variation of the normalized discharge rate $\hat{q_o}$ with $C_D aH/n$. The solid line is the theoretical prediction given by Eq. 2.26. The dashed lines are the upper and lower bounds of the theoretical prediction. The open circles represent the reversed cases. The parameters S and α used to calculate q_o were obtained by fitting the data for $\phi < 0.14$.

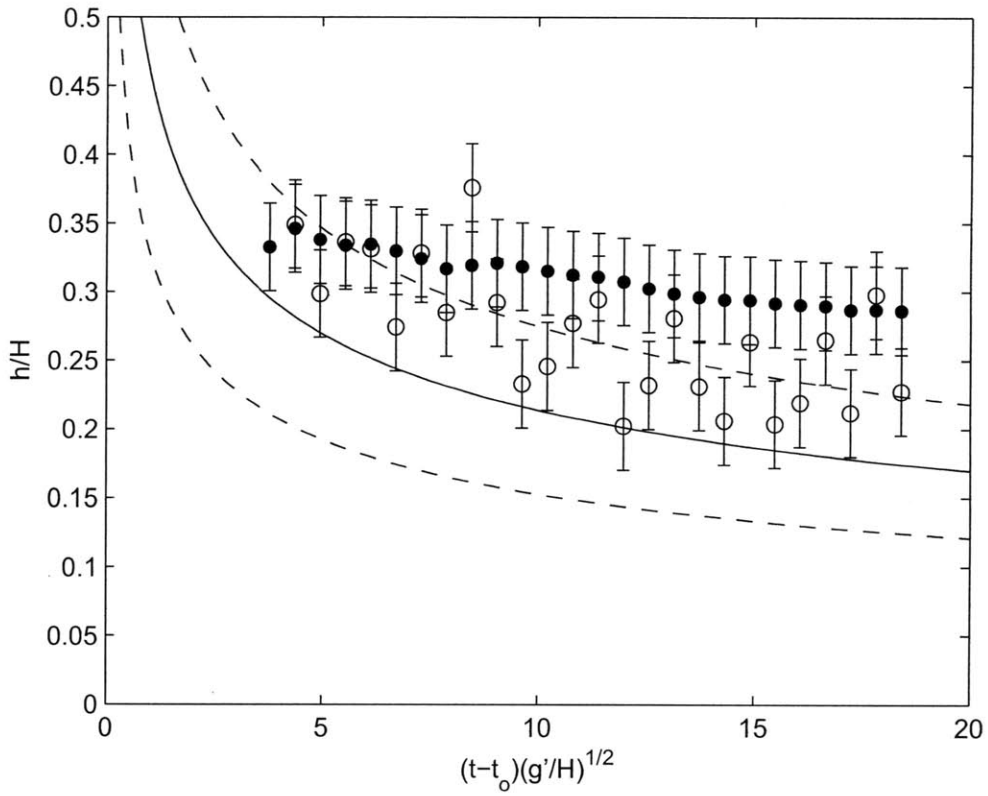

Figure 2.8: The variation of the normalized thickness of the current in the open region $\hat{h}$ with time for case 30. The solid circles are the measured values of $\hat{h}$ at each time point and the open circles are calculated from $\hat{q_o}/\hat{u_o}$ at each time point. The solid line is the theoretical prediction given by Eq. 2.28. The dashed lines are the upper and lower bounds based on the uncertainties in S and α.

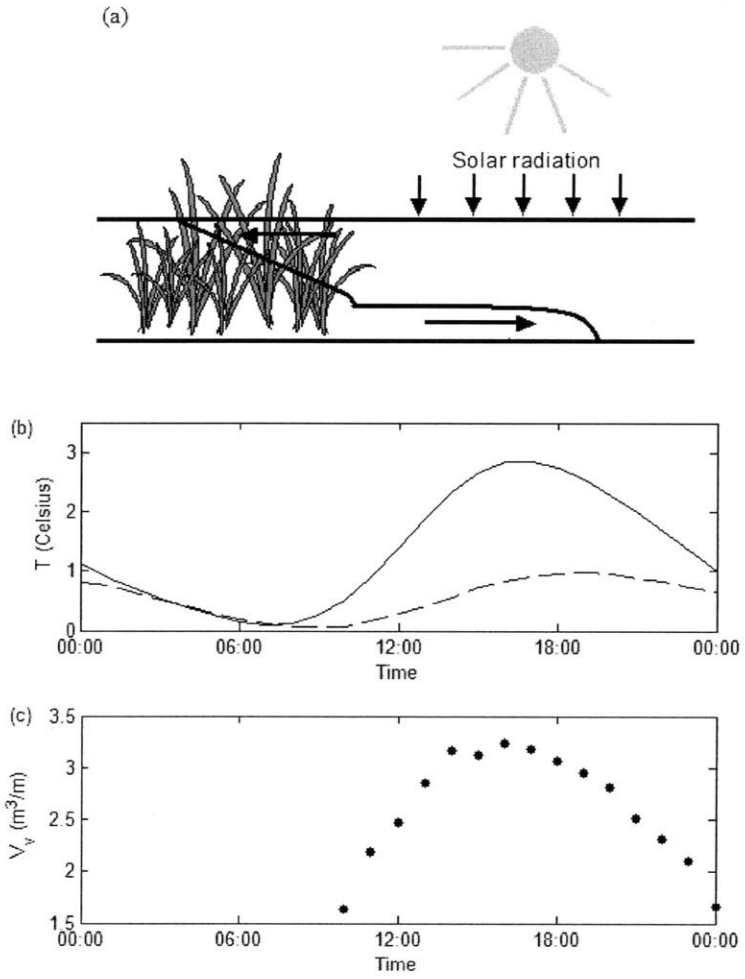

Figure 2.9: (a). Conceptual sketch of thermally-driven exchange in the field. (b). Temperature rise relative to night time low, ensemble averaged over 24 days, in the open (solid line) and vegetated regions (dashed line), data from Lightbody *et al.* (2008). (c). The volume discharge V_v over each hour interval.

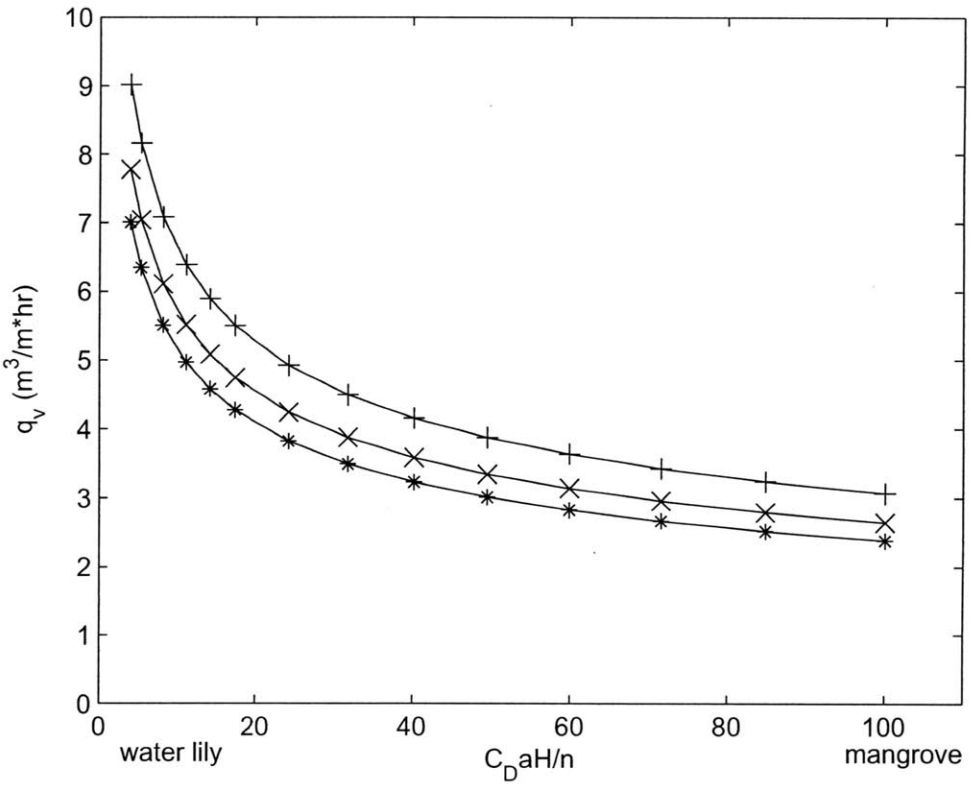

Figure 2.10: The variation of the mean discharge rate q_v over a daily cycle with C_DaH/n for different radiation intensity I_0, assuming $H = 1$ m. $I_0 = 400\ \mathrm{W \cdot m^{-2} \cdot s^{-1}}$ ($\Delta T_0 = 2°\mathrm{C}$) (•) ; $I_0 = 600\ \mathrm{W \cdot m^{-2} \cdot s^{-1}}$ ($\Delta T_0 = 3°\mathrm{C}$) (×) ; $I_0 = 800\ \mathrm{W \cdot m^{-2} \cdot s^{-1}}$ ($\Delta T_0 = 4°\mathrm{C}$) (+).

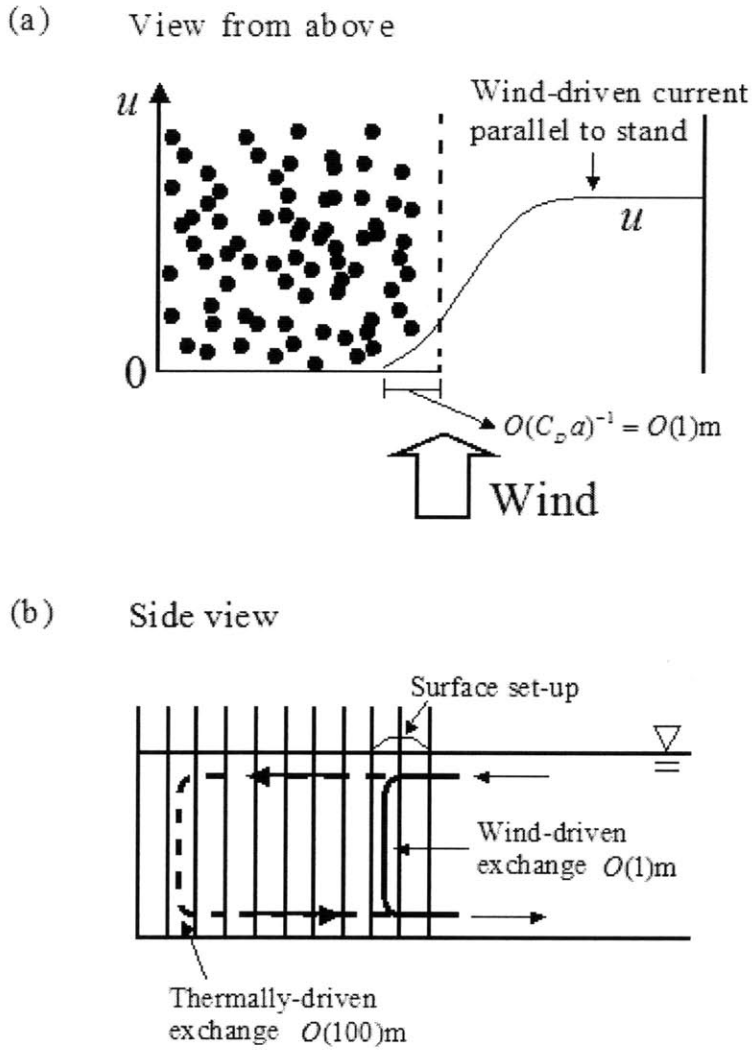

Figure 2.11: (a). Top view of canopy with wind-driven currents running parallel to a canopy edge (after White and Nepf, 2007). (b). Cross-sectional view of wind-driven currents perpendicular to a canopy and exchange flow, and resulting flushing currents. Density-driven flushing shown with dashed line and wind-driven flushing shown with solid line.

Chapter 3

Thermally Driven Exchange Flow between Open Water and an Aquatic Canopy

Abstract

Differential solar heating can result from shading by rooted, emergent aquatic plants, producing a temperature difference between vegetated and unvegetated regions of a surface water body. This temperature difference will promote an exchange flow between the vegetation and open water. Drag associated with the submerged portion of the plants modifies this exchange, specifically, changing the dominant velocity scale. Scaling analysis predicts several distinct flow regimes, including inertia-dominated, drag-dominated and energy-limiting regimes. After a constant heat source is initiated, the flow is initially inertial, but quickly transitions to the drag-dominated regime. Laboratory experiments describe the exchange flow and confirm the scaling analysis. Particle Imaging Velocimetry (PIV) was used to quantify the velocity field. Once the exchange flow enters the drag-dominated regime, the intrusion velocity, u_V, is steady. The intrusion velocity decreases with increasing density of vegetation. The thickness of the intruding layer is set by the length scale of light penetration.

[1]This chapter is Zhang and Nepf (2009) with minor corrections and modifications.

3.1 Introduction

Spatial heterogeneity in water temperature can generate gradients in water density, which in turn can produce convective exchange flows. In lakes, these thermally-driven exchange flows play an important role in the transport of nutrients and other chemicals, and thus can have a significant effect on the lake-scale chemistry and ecology (James & Barko, 1991; MacIntyre & Melack, 1995). Temperature differences can occur between the shallow and deep regions of a water body. During the daytime, uniform solar radiation causes the temperature within the shallow region to rise more rapidly than that in the adjacent deeper region, because the same heat flux is distributed over a smaller water depth. Similarly, during the night, as the heat leaves the water, the temperature in the shallow region drops more rapidly than that in the deeper region. This diurnal cycle of temperature difference has been observed to generate diurnally-varying exchange flows between the littoral zone and the main body of a lake (Adam & Wells, 1984; Monismith *et al.*, 1990; James *et al.*, 1994). Under weak wind conditions, this exchange flow controls the flushing of the littoral zone, reducing the flushing time by several orders of magnitude from turbulent diffusion alone. The exchange flow generated by the differential heating and cooling associated with depth variation has also been studied through laboratory experiment (Sturman & Ivey, 1998; Sturman *et al.*, 1999; Lei & Patterson, 2002a) and modeling (Horsh & Stefan, 1988; Farrow & Patterson, 1993; Lei & Patterson, 2002b; Farrow, 2004). In most of these studies, the variation in depth is modeled as a triangular wedge. These studies provide a clear understanding of the transient and steady components of depth-driven thermal exchange flow, as well as the pattern of reversing flow that is generated by the diurnal cycle of heating and cooling.

Exchange flow due to differential internal heating was first studied by Patterson (1984), who provided the basic scaling analysis for unsteady natural convection due to an internal heat source that was constant vertically and in time, but varied longitudinally. Trevisan & Bejan (1986) studied a similar problem, but modeled the internal heat source as that generated by the absorption of solar radiation through the surface.

Following from this, Coates & Patterson (1993) experimentally studied the unsteady convection produced when part of a water surface is heated, and part is shaded by an opaque layer. Initially, the exchange flow was controlled by the balance between acceleration and the buoyancy-induced pressure gradient. The intrusion velocity in this regime increased with time as $t^{3/2}$. Following this, the thermally-driven exchange flow was controlled by inertia, during which time its velocity varied as $t^{1/2}$. Eventually, the exchange velocity became constant in an energy-limiting regime, in which the rate of absorption of energy is balanced by the rate of energy removal through advection.

Shading by vegetation can also cause differential heating (Chimney *et al.*, 2006; Ultsch, 1973). For example, dense vegetative stands can reduce incident light by 50 to over 90% (Wetzel, 2001). Pokorný & Květ (2004) observed the water temperature in a stand of *Nuphar Lutea* to be as much as 4°C lower than the surrounding open water during day time. Similarly, Lightbody *et al.* (2008) reported that the daytime temperature within the marsh region of a constructed wetland remained 2°C cooler than the adjacent open water areas. Coates & Ferris (1994) showed that shading from floating plants can generate an exchange flow. However, the flow was displaced downward, beneath the root layer. As an extension to Coates & Ferris (1994), this paper will examine the impact of rooted vegetation, for which the root obstruction extends over the entire depth.

Rooted vegetation provides a significant amount of drag, such that we expect rooted plants to both promote, through differential shading, and inhibit, through drag, the thermally-driven exchange flow. Tanino *et al.* (2004) studied the impact of canopy drag on exchange flows by generating a lock-exchange within an array of circular cylinders that extended through the entire water depth. They identified distinct flow structure for the two different drag regimes, namely, linear and quadratic drag. In addition, the drag associated with the array significantly reduced the exchange velocity, compared with the classic, unobstructed exchange flow. Zhang & Nepf (2008) considered the more natural case of exchange between a model canopy and an adjacent region of unobstructed water. The velocity of the intrusion entering

the canopy, as well as the total discharge between the open water and the canopy were strongly dependent on the canopy drag. Tanino *et al.* (2004) and Zhang & Nepf (2008) considered cases in which the reduced gravity, g', was constant, set by the density difference between the initial reservoirs. In this work, g' is not constant because it is generated by spatial variation in a steady heat source, mimicking the evolution of shaded and unshaded regions receiving uniform solar radiation. Under a constant heat source, the temperature difference between the shaded and unshaded regions, ΔT, increases linearly with time, such that g' also increases linearly with time.

The importance of both differential heating and of aquatic vegetation to the ecology and water quality of lakes and reservoirs is well recognized. However, most previous studies have been limited to either exchange flow due to differential heating/cooling or to the effects of vegetation. Oldham & Sturman (2001) examined the impact of vegetative drag on the convective flushing of the littoral zone, associated with depth-differential-cooling. However, the combined effects of vegetative shading and vegetative drag on an exchange flow have not received specific attention. This is the focus of the current study. Compared to Coates & Patterson's (1993) and Coates & Ferris' (1994) classic studies of differential shading, the current work adds the impact of rooted vegetation, providing new insight to a wider range of natural conditions.

3.2 Model development and scaling analysis

When solar radiation impinges on a water surface, a significant portion is reflected from the surface and is lost through scattering. The remaining energy penetrates the surface and is absorbed by the water. Due to absorption, the light intensity or irradiance, I, decreases with distance from the water surface following Beer's Law,

$$I(z) = \sum_{i=1}^{n} I_i \exp\left[-\eta_i(h-z)\right]. \tag{3.1}$$

Here, I_i and η_i are the radiation intensity and the extinction coefficient associated with a particular wavelength, h is the total water depth and z is the height measured from the bed and is positive upward. The extinction coefficient η_i also increases with on turbidity. The infrared band of the spectrum is most easily absorbed in water, and most of the energy associated with the infrared region is absorbed near the water surface. The absorption of light decreases with decreasing wavelength and reaches a minimum absorption for blue, and then increases again in the ultraviolet (UV) region. According to Wetzel (2001), about 53% of the total light energy is transformed into heat and absorbed in the first meter of water. For the purpose of parameterization and application in the field, we consider the bulk behavior of the incoming light and adopt a single-band model, *i.e.* a single value of I_0 and η to represent the behavior of the full spectrum of light, in which I_0 is the total energy input at the surface and η is the bulk extinction coefficient, representing a composite for all wavelengths (Coates & Ferris, 1994; Lei & Patterson, 2002a). Beer's Law can then be written as

$$I(z) = I_0 \exp\left[-\eta(h-z)\right]. \tag{3.2}$$

Now, consider a rectangular domain of constant depth, h, and total length, $(L_V + L_O)$, in which L_V and L_O are the lengths of the vegetated and open region, respectively (Fig. 3.1). In this work, we assume that the emergent portions of the rooted plants completely block the incoming solar radiation. Under constant heat flux I_0, the water in the open region heats up, and becomes less dense than the adjacent water in the vegetatation. This density difference drives an intrusion of warm water into the vegetated region at the surface, with a compensating return flow underneath. The intrusion depth, h_I, is expected to scale with $1/\eta$, which according to Beer's Law (3.2) is the length-scale of heat absorption. In some cases this length scale might be modified by thermal diffusion. However, the diffusion length scale, $\sqrt{\kappa t}$, with κ the thermal diffusivity of water, grows too slowly to impact the exchange flow considered here. Specifically, in one hour diffusion could deepen the heated layer by only 1 cm.

In the field, the extinction coefficient varies from 0.1 m^{-1} to 10 m^{-1}, so that we

expect that h_I ranges from $O(10)$cm to$O(10)$m. As shown in Fig. 3.1, when $h_I < h/2$, the extinction coefficient should set the depth of the intrusion layer, $h_I \sim 1/\eta$. However, the total water depth likely constrains the intrusion depth for $h_I > h/2$.

In the littoral regions of a lake, the horizontal length scale is generally much greater than the water depth. The viscous term $\nu(\partial^2 u/\partial x^2)$ is thus much smaller than $\nu(\partial^2 u/\partial z^2)$ and can be neglected. The conservation of horizontal momentum in a two-dimensional system is then

$$\frac{\mathrm{D}u}{\mathrm{D}t} = -\frac{1}{\rho}\frac{\partial P}{\partial x} - Cau + \nu\frac{\partial^2 u}{\partial z^2}, \tag{3.3}$$

where u is the horizontal velocity component, P is the pressure, ρ is the fluid density, ν is the kinematic viscosity of water and x and z are horizontal and vertical axis, respectively, and t is time. The second term on the right-hand side characterizes the vegetative drag, and a is the frontal area of vegetation per unit volume. C $(\mathrm{m}\cdot\mathrm{s}^{-1})$ is a linear drag coefficient. A linear drag law is selected based on the expected range of stem Reynolds number. Based on Coates & Patterson (1993), the velocity of an exchange flow produced by surface shading without vegetation can be on the order of 0.1 cm/s. This value can be regarded as an upper limit for the cases being considered here, which will be damped by vegetative drag. Typical values of stem diameter for aquatic plants are between 0.5 to 1 cm, indicating a typical stem-Reynolds number ($Re_d = ud/\nu$) of less than 10. Previous studies by Tanino *et al.* (2004) and Zhang & Nepf (2007) have shown that a linear drag law is appropriate in characterizing the flow at this range of Reynolds number. As we will show later, the Reynolds numbers for our experiments range from 0.8 to 3. In addition, we will consider model vegetation with densities between solid volume fraction 3% and 15%. Koch & Ladd (1997) modeled the drag produced by random arrays of cylinders with solid volume fraction between 5% and 40% and Reynolds number between 0.2 to 180. In this work, we will estimate the drag coefficient C based on drag values reported in Koch & Ladd (1997).

The following scaling is introduced,

$$x \sim L, \quad z \sim h_I, \quad \Delta P \sim \Delta\rho g h_I \sim \rho\alpha\Delta T g h_I, \tag{3.4}$$

in which L is the horizontal length scale of the intrusion in the canopy (Fig. 3.1). $\Delta\rho$ is the density difference between the canopy and open water, and ΔP is the resulting pressure difference. α is the coefficient of thermal expansion. g is gravity. The temperature difference, ΔT, increases with time due to the constant heat flux, I_0, impacting the water in the open region only. The temperature difference can be expressed as $\Delta T = I_0 t/\rho C_P h_I$, where C_P is the specific heat of water. With the above scaling, (3.3) can be written in the following form,

$$u^2 \sim -\frac{g\alpha I_0 t}{\rho C_P} - CauL + \nu\frac{uL}{{h_I}^2}. \tag{3.5}$$

We assume that the system starts from rest with $L = 0$. Therefore, in the initial period after the heat flux has started, the system is controlled by the balance between inertia and buoyancy only, *i.e.* the last two terms in (3.5) drop out for small L. Equating the first and second term in (3.5), the velocity scale for the inertia-dominated regime, u_i, can be found.

$$u_i \sim \left(\frac{g\alpha I_0 t}{\rho C_P}\right)^{1/2} \sim \sqrt{g' h_I}, \tag{3.6}$$

where g' is obtained by

$$g' = \frac{\Delta\rho}{\rho} g = \alpha\Delta T g = \frac{g\alpha I_0 t}{\rho C_P h_I}. \tag{3.7}$$

The result given by (4.14) is mathematically similar to the theory for the classic gravity current, except that the reduced gravity, g', is not constant, but increases linearly with time, resulting in $u_i \sim t^{1/2}$. The same scaling was previously derived by Coates and Patterson (1993) for flows in the absence of rooted vegetation. Coates and Patterson (1993) also noted that prior to the inertia-dominated regime, the conduction

length scale, $\sqrt{\kappa t}$, is briefly dominant and the velocity scale in this regime varies with $t^{3/2}$. However, this regime is very short-lived and is not considered here.

As the intruding front lengthens ($L > 0$) over time, both the viscous and vegetative drag become important. For most canopies the vegetative drag will dominate, as is shown by comparing the two drag terms. Specifically, vegetative drag will dominate when

$$\frac{Cah_I{}^2}{\nu} \gg 1. \tag{3.8}$$

In typical aquatic systems, $a = O(0.01 \sim 0.1\ \mathrm{cm}^{-1})$, which corresponds to roughly 100 to 1000 stems/m^2 (Kadlec, 1990). With $Re_d = O(100)$ and $C \approx 1$cm/s (Tanino *et al.*, 2004), (3.8) shows that viscous drag can be neglected for $h_I \gg 0.3$ cm. This condition will generally be met in the field, as well as in our laboratory studies. In evaluating (3.8), we assumed the flow to be laminar, *i.e.* we consider molecular viscosity, ν. This can be justified by considering $h_I = O(10\ \mathrm{cm})$ and $u \leq 0.1$ (cm/s) (Coates & Patterson, 1993), $Re_{h_I} = uh_I/\nu \leq O(100)$. Therefore, we anticipate that the laminar flow assumption will be correct for most conditions.

By comparing the terms for vegetative drag and inertia in (3.5), we anticipate that vegetative drag will dominate when $u \ll CaL$. Recognizing $L = ut$, the time-scale at which vegetative drag will exceed inertia is

$$T_V \sim (Ca)^{-1}. \tag{3.9}$$

With the values for a and C given above, T_V is estimated to be $O(10 - 100\ \mathrm{s})$, which indicates a short duration of inertial flow, *e.g.* as compared to the time-scale of daily heating $O(12)$ hours. After this time, the velocity is determined by the balance of buoyancy and vegetative drag. Equating these terms in (3.5), and using $L = ut$, gives

$$u_V \sim \left(\frac{g\alpha I_0}{\rho C_P Ca}\right)^{1/2}. \tag{3.10}$$

It is interesting to see that the velocity is steady in this regime. Although the buoyancy increases with time due to the constant heat flux, $g' = \alpha g I_0 t/\rho C_P h_I$, the vege-

tative drag also increases with increasing intrusion length, $L \sim t$, and the two effects balance.

Previous studies considered the case with a constant buoyancy (*e.g.* ΔT, $\Delta\rho$ being fixed, such that g' is fixed), for which (3.10) reduces to

$$u_{Vg'} \sim \left(\frac{g'h_I}{Cat}\right)^{1/2}. \tag{3.11}$$

The subscript g' denotes constant g' condition. For constant g', the velocity decreases with time. This scaling was verified by Tanino *et al.* (2004) and Zhang & Nepf (2008) for the case $h_I = h$. Finally, since we anticipate that the extinction coefficient, η, sets the depth of intrusion, h_I, it is reasonable to write the volume discharge rate under constant flux I_0 as

$$q \sim \left(\frac{g\alpha I_0}{\rho C_P Ca}\right)^{1/2} \frac{1}{\eta}. \tag{3.12}$$

The energy balance provides another possible control on the velocity, because the flow cannot carry away more heat than is supplied by the surface flux (Coates & Patterson, 1993). In the energy-limiting regime, the surface flux per unit width, $I_0 L_O$, is balanced by the advective flux per unit width, *i.e.*

$$I_0 L_O = u\rho C_P \Delta T h_I, \tag{3.13}$$

Recall that L_O is the length of heated surface in the open water region (Fig. 3.1). From (3.13), the energy-limiting velocity scale is found to be (as in Coates & Patterson, 1993)

$$u_E \sim \frac{I_0 L_O}{\rho C_P \Delta T h_I}. \tag{3.14}$$

Once the flow has reached the energy-limiting regime, the heat fluxes are in balance and ΔT will be constant. The value of ΔT in this regime depends on how long it takes to reach the energy-limiting regime, which in turn depends on whether the drag-dominated regime is reached before or after the energy-limiting regime. First, consider the case in which the flow is inertia-dominated until reaching the energy-

limiting regime. Equating the inertial velocity scale u_i (4.14) to the energy-limiting velocity scale in (3.14), and using $\Delta T = I_0 t/\rho C_P h_I$, the time scale to reach the energy-limiting regime is given by

$$T_E \sim \left(\frac{\rho C_P {L_O}^2}{g\alpha I_0}\right)^{1/3}. \tag{3.15}$$

This result was previously derived by Coates & Patterson (1993) for differential heating without vegetation. With typical field values of $I_0 = 515$ Wm^{-2} and $L_O = 100$ m (as suggested by Coates & Patterson, 1993), (3.15) gives $T_E = 3500$ s, which is much longer than the time required for the vegetative drag to dominate, $T_V = 10 - 100$ s. Therefore, under typical conditions, the drag-dominated regime will occur first, and once achieved it will set up a steady flow, *i.e.* u_V is constant and ΔT increases over time. This is different from the result of Coates & Patterson (1993) in which the inertia-dominated regime is followed by the energy-limiting regime. That is, the contribution of vegetation drag changes the dominant velocity scale.

Since the vegetative drag becomes important at very early time, we now revise our estimate for the time-scale at which the energy-limiting regime is reached. By equating the drag-dominated velocity, u_V given in (3.10) to u_E given in (3.14), along with $\Delta T \sim (I_0 t/\rho C_p h_I)$, we have

$$T_E \sim \left(\frac{\rho C_P C a {L_O}^2}{g\alpha I_0}\right)^{1/2}. \tag{3.16}$$

Using the representative values give above, $T_E = 6.5 \times 10^4$ s, or roughly 18 hrs. Given the diurnal heating cycle is typically 12 hrs or less, this time scale indicates that under typical field conditions the energy-limiting regime is unlikely to occur, and the exchange flow is completely controlled by the drag-dominated regime.

3.3 Experimental Procedures

To test the above scaling analysis, a series of experiments were conducted in a Plexiglass® tank with dimensions of 70(L) × 15(W) × 40(H)cm. The tank consisted of two separate chambers, shown in Fig. 4.2. Two 600-Watt spotlights were used to produce a uniform heat source. Different combinations of the two spotlights produced three different radiation intensities (Table. 3.1). A mirror was mounted over the tank to direct the parallel light from the spotlights vertically downward into the experimental chamber. The angle of the mirror was adjusted to ensure a sharp edge between the open region and the shaded region. The aperture of the spotlight was wider than the tank, so that only the central region of the light was used for heating. This ensured that the incoming light uniformly illuminated the open water.

Temperature measurements were made using four submersible Hart Scientific® 5611-T teflon thermistor probes. The probe tip was 3 mm in diameter and the sensor was 13 mm long. The thermistor probe had a measuring range of 0 °C to 100 °C with an accuracy of 0.0025 °C. A 1529 Chub-E4 Thermometer was used to simultaneously log temperature data from the four probes at a sampling rate of 1 Hz.

On one side of the tank, a side chamber with dimensions of 10(L) × 15(W) × 40(H)cm was separated from the main chamber. This region was used to determine the values of I_0 and η. Because of the narrowness of the side chamber, fluid motions were prohibited. If we neglect conductive heat transfer within the water, the temperature change at depth, z, can be expressed as

$$T(z,t) = \frac{I_0\eta}{\rho C_p} \exp[-\eta(h-z)]t, \tag{3.17}$$

Differentiating (3.17) with time gives the time rate of change of temperature,

$$\frac{\partial T(z,t)}{\partial t} = \frac{I_0\eta}{\rho C_p} \exp[-\eta(h-z)]. \tag{3.18}$$

Under a constant heat source, *i.e.* I_0 constant, temperature increases linearly over time; and $\partial T(z,t)/\partial t$ is constant. Using temperature data from two different depths,

e.g. $T(z_a, t)$ and $T(z_b, t)$, we can use (3.18) to find the following relation,

$$\frac{\partial T(z_a, t)/\partial t}{\partial T(z_b, t)/\partial t} = \exp[-\eta(z_b - z_a)]. \tag{3.19}$$

Temperature records and (3.19) were used to find the extinction coefficient η. The radiation intensity I_0 was then found by fitting the measured temperature to (3.18). For this analysis, the four temperature probes were placed in the side chamber, at $z = 2$, 10, 18 and 25 cm above the bottom of the tank.

The thermally-driven flow was generated in a subchamber with dimensions of 60(L) $\times$ 15(W) $\times$ 40(H)cm, half of which was covered by a board, perforated with 6 mm holes. Cylindrical dowels with diameter $d = 6$ mm and 50 cm length were passed through randomly selected holes and extended down to the bottom of the chamber. The cylinder array was then covered by a piece of black cloth to prevent light from going through unfilled holes.

The solid volume fraction, ϕ, ranged from 3% to 15%, corresponding to a frontal area per unit volume of $a = 0.01$ cm^{-1} to 0.05 cm^{-1}. In the field, solid volume fraction varies from a lower limit of $\phi = 1\%$ (water lily) to an upper limit of $\phi = 40\%$ (mangroves). Because of the difficulty in visualizing flow within a dense dowel array, our work was restricted to cases up to $\phi = 15\%$. To track the intrusion, three thermistor probes were placed within the model canopy along the centerline of the tank and, at distances of 6.5, 13.0 and 19.5 cm from the canopy edge, and at 2 cm below the water surface. This depth was chosen to fall in the middle of the intruding layer, based on preliminary observations. Stainless steel rods of the same diameter as the dowels were used to hold the probes. To position the probes, small holes were drilled in the rods 1 cm apart, with an accuracy of ± 1 mm. After the light was turned on, the thermometers logged temperature for the duration of the experiment at a frequency of 1 Hz. For some experiments, an additional temperature probe was placed at 13.0 cm, but located near the side-wall of the tank. Comparing the two probes located at the same longitudinal (13 cm) but different transverse positions confirmed that there were no preferential flow paths, and the intrusion was

approximately uniform over the tank width.

Particle Imaging Velocimetry (PIV) was used to quantify the flow field within the model vegetation. Pliolite® particles with a density of 1.02 g/cm^3 were added to the water. A 2-cm wide gap starting at 8 cm from the edge of the canopy was left within the model canopy as a window for the PIV. The width of the gap was chosen to be the same order of magnitude as or smaller than the distance between dowels. A laser sheet entering through the bottom of the tank illuminated the gap. The laser power was kept low enough (0.3 watts) to prevent thermal plumes from being generated due to the heating of the tank's bottom wall. Preliminary experiments also confirmed that no thermal plumes were formed on the side walls due to heating by the spot light.

Coates & Patterson (1993) reported in their study of exchange flow, without vegetation, that the exchange velocity generated by similar differential heating was approximately 0.1 cm/s. This can be regarded as an upper limit of the expected magnitude of flow in the present study. To improve the accuracy of PIV at such low velocity, a digital single-lens-reflex (SLR) camera with a maximum resolution of 3872×2592 pixels was used to capture the flow field at a frame rate of 0.5 fps. Given the resolution of the camera, one pixel was approximately equal to a distance of 0.005 cm. Consequently, the PIV technique could resolve velocities on the order of 0.005 cm/s. The image acquisition was started after the intrusion had passed the PIV window located at 8 cm. The passage of the intrusion front was indicated by an increase in the temperature at the 13-cm thermistor. Fifty pictures were taken for each experiment. MatPIV v. 1.6.1, a Matlab software package, was used to calculate the velocity field from the pictures. Details about the technique of Particle Imaging Velocimetry can be found in Sveen (2004) and Gharib & Daribi (2000).

After the velocity field was obtained from PIV, a velocity profile was extracted from the middle of the PIV window. The velocity profiles within each 10 second interval, *i.e.* 5 pictures, were averaged to remove noise. The averaged velocity profiles were integrated over depth to confirm conservation of volume, *i.e.* the volume of the intruding layer was equal to that of the outflow. The depth of intrusion, h_I, was

defined by the position at which the velocity component changed its direction from inflow to outflow. The mean intrusion velocity, U_{mean} was calculated by averaging the velocity profile from the surface to the depth of the intrusion.

3.4 Results

For each radiation intensity we evaluated I_0 and η using the narrow side-chamber. Under constant heat flux, I_0, the temperature increased linearly with time, as expected (Fig. 3.3). The time rate of change of temperature was larger near the surface than at depth, indicating that more energy is absorbed near the water surface, which agrees with previous observations (Wetzel, 2001). The pair of sensors nearest the surface ($z_3 = 18$ cm and $z_4 = 25$ cm) were used to calculate I_0 and η. The radiation intensity and the extinction coefficient for all cases are summarized in Table. 3.1.

In our model the extinction coefficient was between 6/m and 7/m, consistent with previous, similar models used by Coates & Patterson (1993) and Lei & Patterson (2002a), who reported values of 21.6/m and 6.2/m, respectively, for clear water in laboratory tank. In contrast, the extinction coefficients found in natural lakes range from $\eta = 0.2$/m in very clear lakes to 4/m in lakes with typical high turbidity (Wetzel, 2001). However, values as high as 10/m have been observed in the field. Compared to the typical values observed in the field, laboratory experiments tend to report higher values for η. There are two reasons for this difference. First, in the field, η is a composite of wavelengths, ranging from infrared to ultraviolet. In the laboratory, however, the heat source is usually a stage light, whose irradiance is mainly composed of long-wave radiation, *e.g.* infrared to red. Since the short-wave portion penetrates more deeply into the water, excluding the short-waves results in a higher extinction coefficient. Second, in the field the calculation of the vertical extinction coefficient generally excludes data from the first meter below the surface because of surface agitation (Wetzel, 2001), and this excludes some fraction of the long wave radiation, artificially reducing η.

After the spotlight was turned on, a temperature difference between the illumi-

nated and shaded regions appeared and grew with time. An intrusion of warmer water entered the model canopy. Temperature probes positioned in the canopy marked the arrival of this intrusion. The temperature change, δT, with respect to the initial temperature at each location is shown in Fig. 3.4. Initially, $\delta T = 0$, indicating that the warm intrusion has not yet reached a given location. The rise in temperature marks the arrival of the intrusion, and the subsequent steady linear increase of temperature is consistent with an intrusion of constant velocity. For example, the temperature at $x = -6.5$ cm started to rise at $t = 300$ sec, and the temperature at $x = -13.0$ cm started to rise at $t = 500$ sec (Fig. 3.4). The temperature data at $x = -6.5$ cm and $x = -13.0$ cm exhibit a small drop in temperature, just preceding the steady increase. This is attributed to a downward vertical motion that precedes the intrusion front. Before starting the experiments, the tank sat in the laboratory for several hours to equilibrate with the room. During this period, the surface temperature became slightly lowered, due to surface heat loss. According to previous laboratory observations (Zhang & Nepf, 2008) and numerical studies (Jamali *et al.*, 2008), downward motion is induced just ahead of the intruding front. We believe this localized, downward motion delivers cooler surface water past the probe just before the intrusion arrives, creating a short drop in temperature preceding the steady rise in temperature that marks the passage of the intrusion. It was also observed that the temperature at $x = -19.5$ cm increased mildly starting about 300 sec and then increased sharply after the warm intruding current passed this position. We believe that the mild increase in the temperature in the thermistor located at -19.5 cm is due to the laser light sheet used for PIV. We turned the laser on when we observed the first temperature probe started to rise. It is possible that the outer edge of the laser sheet heated the water near the far thermistor, and caused the mild increase of the temperature before the arrival of the intrusion. In subsequent studies, we shuttered the laser to reduce this effect.

PIV measurements confirmed that after the intrusion has passed the PIV window, the velocity was predominantly horizontal. The predominantly horizontal flow is consistent with previous experimental observations by Coates & Patterson (1993) and

Coates & Ferris (1994) for thermally-driven flow, and Zhang & Nepf (2008) for lock-exchange flow. A vertical profile of velocity was extracted from the center of the PIV window. Two examples for $a = 6.4\text{m}^{-1}$ are shown in Fig. 3.5. The velocity profiles maintained the same shape and magnitude over the duration of the PIV measurements (100 sec), in agreement with our scaling analysis, which predicts a steady intrusion velocity for the drag-dominated regime, as shown in (3.10). For the cases shown in Fig. 3.5, the flow transitions to the drag-dominated regime at $T_V = 30$ sec based on (3.9). Therefore, the velocity profiles shown in Fig. 3.5 were in the drag-dominated regime. Note that, it was also observed that the intrusion consists of a single layer, despite the fact that the layer is vertically stratified. A single-layer intrusion was also observed by Coates & Patterson (1993). These observations indicate that the vertical stratification within the layer was not dynamically important. In each case the maximum intrusion velocity was 0.09 cm/s. The return flow, however, decreased with increasing total water depth, *i.e.* compare Fig. 3.5(a) ($h = 10$ cm) and Fig. 3.5(b) ($h = 15$ cm). This is consistent with continuity. Indeed, as the total water depth approaches infinity, the return flow would become vanishingly small. Finally, the parabolic shape the velocity profile near the bed indicates the development of a viscous boundary layer (Fig. 3.5).

The intrusion depth, h_I, was extracted from each velocity profile, and the variability within each experimental run used as an estimate of uncertainty. The normalized intrusion depth, ηh_I, for each run is shown in Fig. 3.6. There is no systematic correlation between the normalized intrusion depth ηh_I and ah, implying that the surface intrusion depth is not controlled either by the total water depth, h, or the canopy density, a. Using all available runs, $\eta h_I = 0.28 \pm 0.06$, which is shown by the solid line in Fig. 3.6. For similar heating conditions, Coates & Patterson (1993) found $\eta h_I = 0.65$.

Profiles of velocity, as shown in Fig. 3.5, were used to estimate the mean intrusion velocity U_V. A second estimate of U_V can be made from the temperature records, such as those shown in Fig. 3.4. Specifically, we divided the distance between two temperature probes by the time interval between the arrival of the intrusion, as indi-

cated by the onset of the steady increase of temperature. For every run the velocities calculated from PIV and from the temperature records were the same within uncertainty (data not shown). This confirms that the velocity measured at the PIV window is representative of the velocity at the intrusion front, *i.e.* the velocity is constant along the length of the intrusion.

For comparison, the drag-dominated velocity, u_V, given in (3.10) is normalized by the viscous-dominated velocity scale, which was derived in Coates & Patterson (1993). This velocity ratio is proportional to the ratio of viscous stress to vegetative drag, as shown by the third term in (3.20),

$$u_v^* = u_V / [\frac{g\alpha I_0 h_I^2}{\rho C_P \nu}]^{1/2} \sim [(\frac{Cah_I^2}{\nu})^{1/2}]^{-1}. \tag{3.20}$$

To normalize the measured velocity using (3.20), the linear drag coefficient C was interpolated from the numerical results of Koch & Ladd (1997), who reported drag for ϕ between 5% and 40% and Re_d between 0.2 to 180, conditions that correspond to those studied here. The estimated drag coefficients are listed in Table. 3.1. The drag coefficient is only weakly dependent on Re_d, which is consistent with our assumption of linear drag law. However, the drag coefficient increases with increasing a. As Koch & Ladd (1997) explain, as ϕ and therefore a increase, the spacing between array elements decreases, and the viscous stress, which dominates the total drag at these low Reynolds numbers, increases. Finally the average intrusion velocity, U_{mean}, is normalized following (3.20), and using the following parameters: $g = 9.8$ m/s^2, $\alpha = 2.1\times10^{-4}$ K^{-1}, $C_P = 4182$ J $\cdot$ Kg^{-1} $\cdot$ K^{-1}, as well as the measured I_0 and η for different cases. The normalized U^*_{mean} is plotted against $(Cah_I^2/\nu)^{1/2}$ in a log-log coordinate (Fig. 3.7). The intrusion velocity decreases as the vegetative drag increases. The fitted slope, -1.2 ± 0.2 (with 95% confidence), agrees with our theoretical prediction of -1, based on (3.20). We anticipate that as the vegetative drag decreases further and becomes comparable with the viscous drag, *i.e.* $(Cah_I^2/\nu)^{1/2} \to 1$, the normalized velocity U^*_{mean} should become $O(1)$; the intrusion velocity is then controlled by viscous drag.

3.5 Conclusion

This paper has examined the thermally driven exchange flow generated by the differential shading between open water and an adjacent emergent canopy under a constant light source. Scaling analyses described the expected flow regimes and associated velocity scales. Compared to the unobstructed exchange flow studied by Coates & Patteson (1993), the presence of a rooted aquatic canopy alters the dynamics of the exchange flow; specifically, the exchange flow is controlled by vegetative drag. The drag dominated velocity scale was confirmed by experiment. In addition, we show that the energy-limiting regime is unlikely to occur in the lab or in the field.

Using the typical values observed in the field, $I_0 = 515$ W/m^2, $L_0 = 100$ m and $\eta = 4.4$ m^{-1} (Coates & Patterson, 1993), a canopy of solid volume fraction $\phi = 0.05$ will generate an average intrusion velocity of 0.06 cm/s and a mean discharge rate of 0.42 cm^3/cm $\cdot$ s. Similarly, for a canopy of solid volume fraction $\phi = 0.15$, the average intrusion velocity will be 0.04 cm/s, with a mean discharge rate of 0.24 cm^3/cm $\cdot$ s. The duration of the exchange flow is approximately a diurnal cycle, *i.e.* $\sim$ 12 hours. Over the course of 12 hours, the exchange flow with $\phi = 0.15$ can flush a vegetated littoral zone of up to width $L = u_V t = 25$ m.

While our model can be used to estimate the magnitude of the exchange flow driven by thermal forcing, there are still challenges in applying our model in the field. First, the application of the model requires an input of the drag coefficient C, which is generally unknown a priori. Although the determination of drag coefficient has been studied in the literature, *e.g.* Koch & Ladd (1997), Tanino & Nepf (2008), most work is limited to a certain range of Reynolds number, a certain range of volume fraction, or very simple morphology, *i.e.* circular cylinders. A universal, explicit solution for C that covers a wide range of Reynolds number and solid volume fraction and vegetation morphology is still not available. Second, in most studies on vegetative drag, aquatic vegetation are modeled with a uniform morphology, such as rigid cylinders. We expect that the morphology of specific vegetation may alter the structure of the exchange flow. For example, leafy parts of a plant canopy can induce

variance in the solid volume fraction, ϕ, across the water depth and thus generate non-uniform drag. Such vertical variation in ϕ could affect the vertical structure of the exchange velocity. Third, our model has only been tested with a narrow range of η. The effects of varying η on the intrusion depth as well as the discharge rate will be a subject of future research. Last, modeling the effects of time-varying radiation intensity, as occurs over the diurnal cycle, was beyond the capabilities of the current experimental configuration. We hope this will be addressed in future field and numerical investigations.

Table 3.1: Summary of experimental conditions and model parameters.

Run	ϕ	$a\ (m^{-1})$	$h\ (\pm 0.1)cm$	$I_0\ (\mathrm{W/m^2})$	$\eta\ (\mathrm{m^{-1}})$	$C\ (m/s)$
1	0.03	6.37	10.0	157 ± 1	6.65 ± 0.04	0.0046
2	0.05	10.6	10.0	157 ± 1	6.65 ± 0.04	0.0051
3	0.08	17.0	10.0	157 ± 1	6.65 ± 0.04	0.0058
4	0.12	25.5	10.0	157 ± 1	6.65 ± 0.04	0.0074
5	0.15	31.9	10.0	157 ± 1	6.65 ± 0.04	0.0091
6	0.03	6.37	15.0	157 ± 1	6.65 ± 0.04	0.0045
7	0.05	10.6	15.0	157 ± 1	6.65 ± 0.04	0.0048
8	0.08	17.0	15.0	157 ± 1	6.65 ± 0.04	0.0056
9	0.12	25.5	15.0	157 ± 1	6.65 ± 0.04	0.0073
10	0.15	31.9	15.0	157 ± 1	6.65 ± 0.04	0.0091
11	0.03	6.37	10.0	183 ± 1	5.98 ± 0.02	0.0045
12	0.05	10.6	10.0	183 ± 1	5.98 ± 0.02	0.0051
13	0.08	17.0	20.0	183 ± 1	5.98 ± 0.02	0.0057
14	0.12	25.5	15.0	200 ± 2	7.02 ± 0.03	0.0074
15	0.05	10.5	15.0	200 ± 2	7.02 ± 0.03	0.0049
16	0.08	17.0	15.0	200 ± 2	7.02 ± 0.03	0.0057

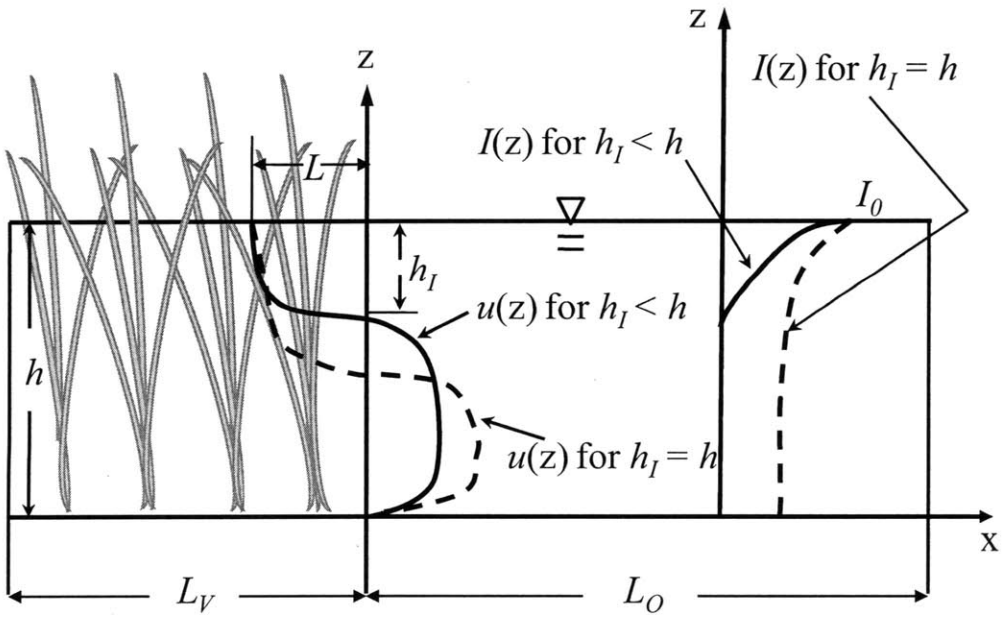

Figure 3.1: A sketch of thermal and intrusion length scales.

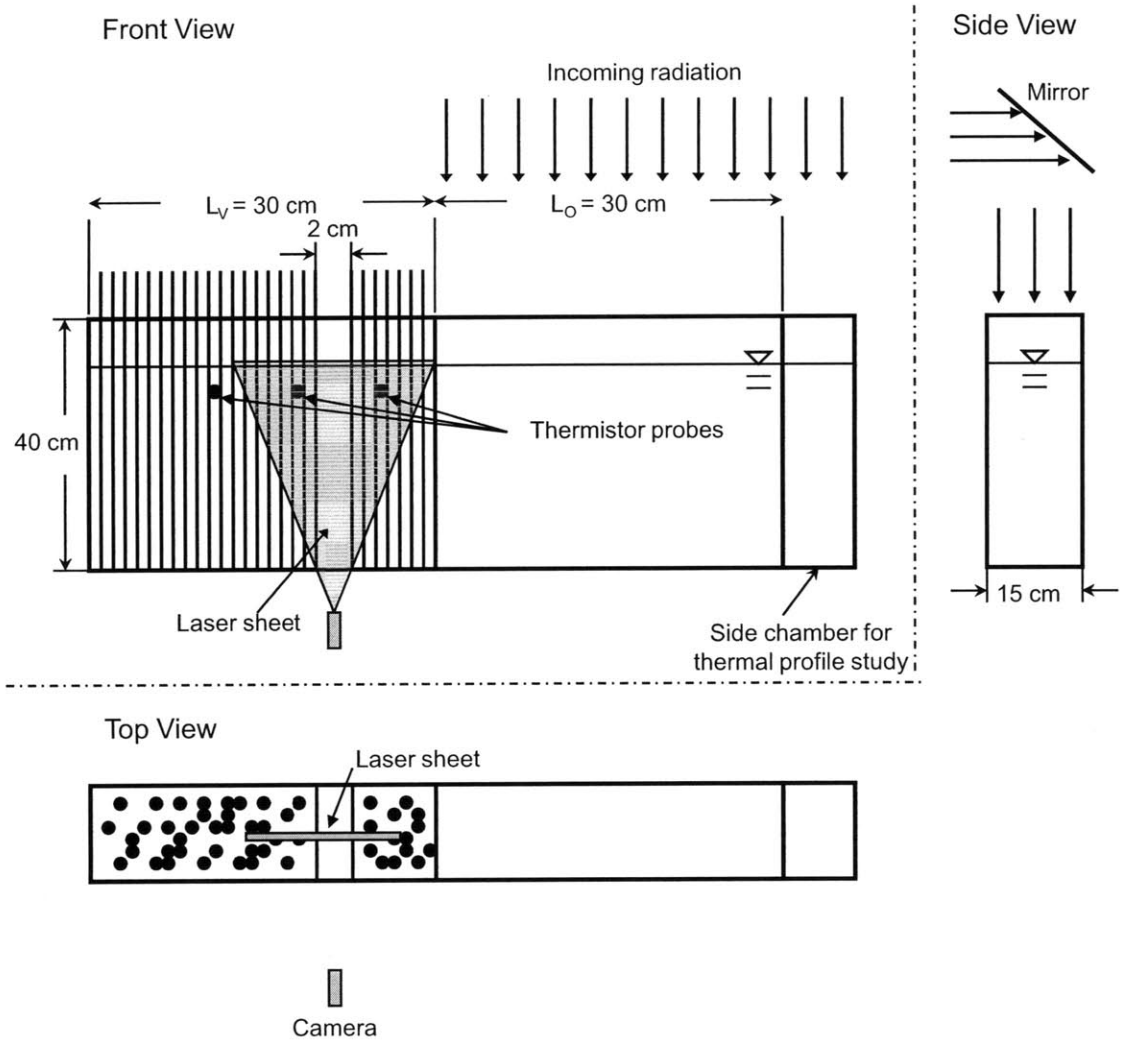

Figure 3.2: A sketch of the experimental setup. The sketch is not plotted to scale. Specifically, the width of gap for PIV is the same order of magnitude or smaller than the distance between dowels.

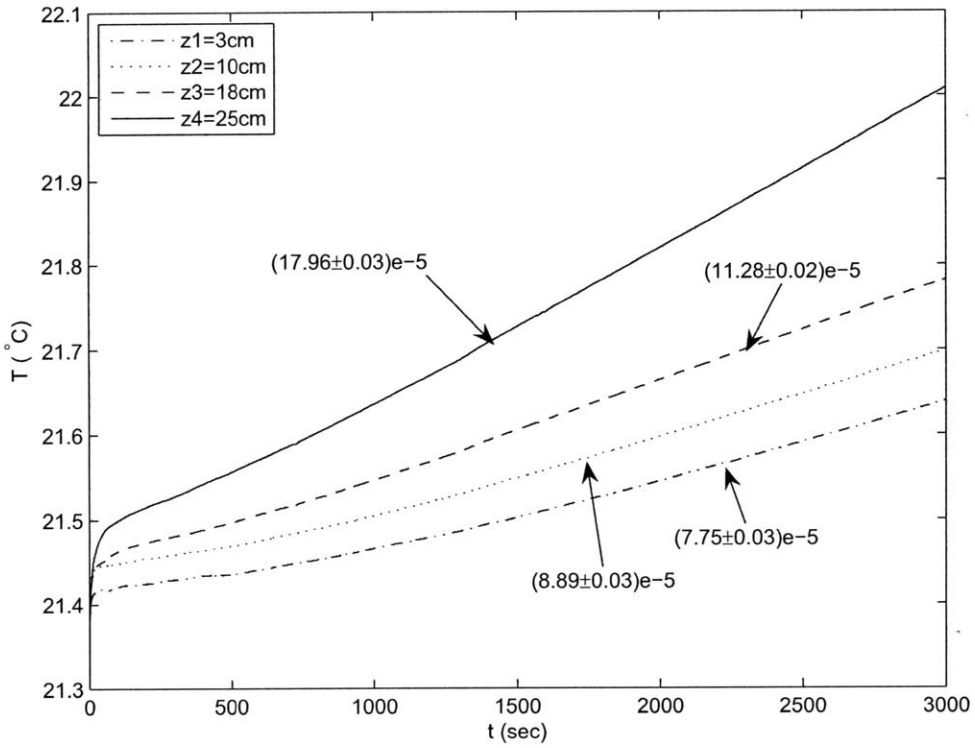

Figure 3.3: The time variation of temperature at different depths under constant heat source. Numbers are the average time rate of change of temperature at each depth (°C/s). The temperature data was collected in the side chamber.

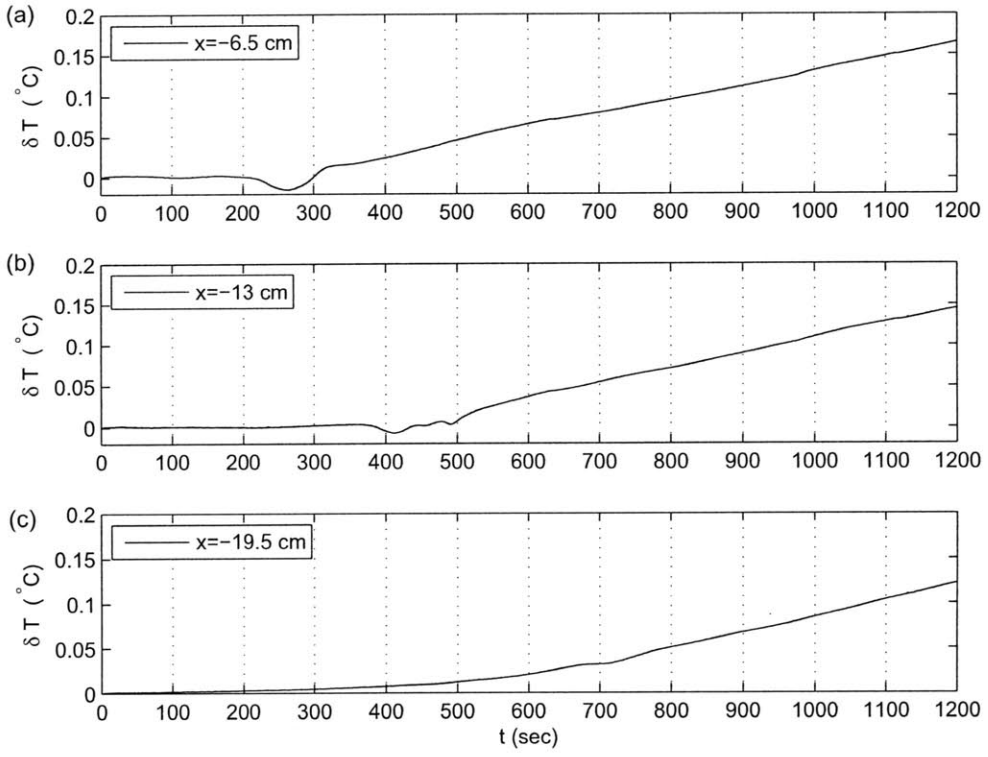

Figure 3.4: Temperature change of water in the shaded region for case 1, after the start of experiment, at (a). $x = -6.5$ cm, (b). $x = -13.0$ cm, (c). $x = -19.5$ cm. δT is the temperature change with respect to its initial temperature.

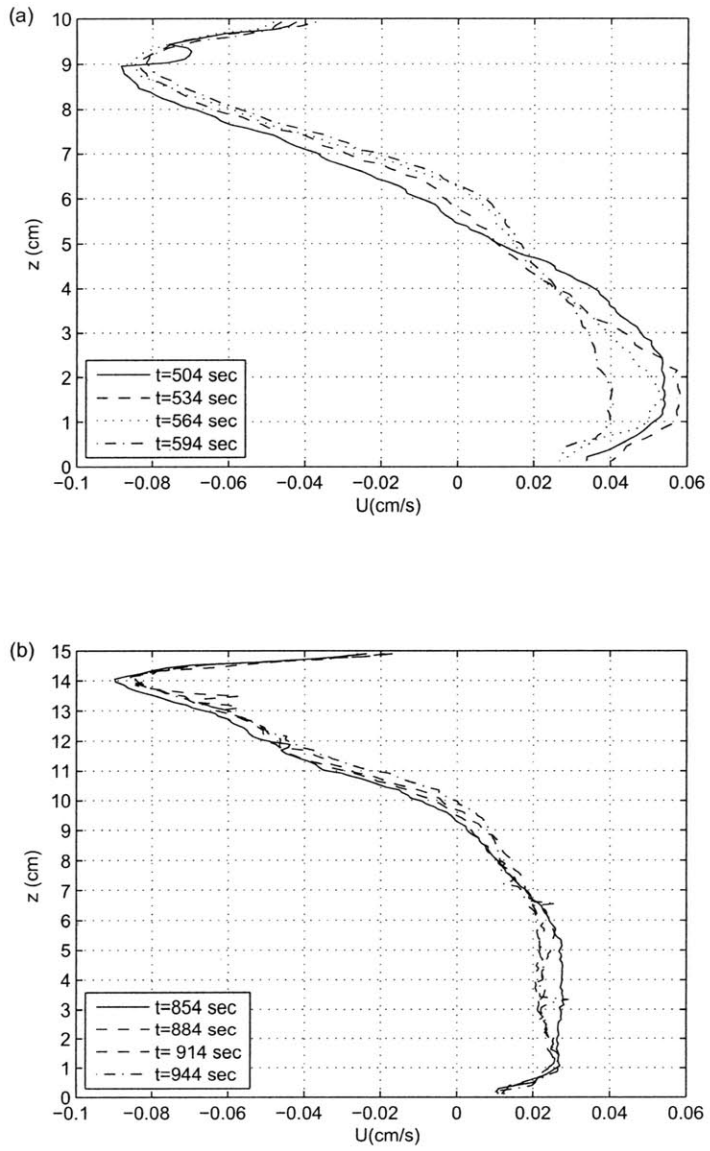

Figure 3.5: Profiles of horizontal velocity sampled at 9 cm from the edge of the canopy, for $h = 10$ cm and $a = 6.37/m$ (case 1 (a)) and $h = 15$ cm and $a = 6.37/m$ (case 6 (b)). Note that the z-axes are not the same scale.

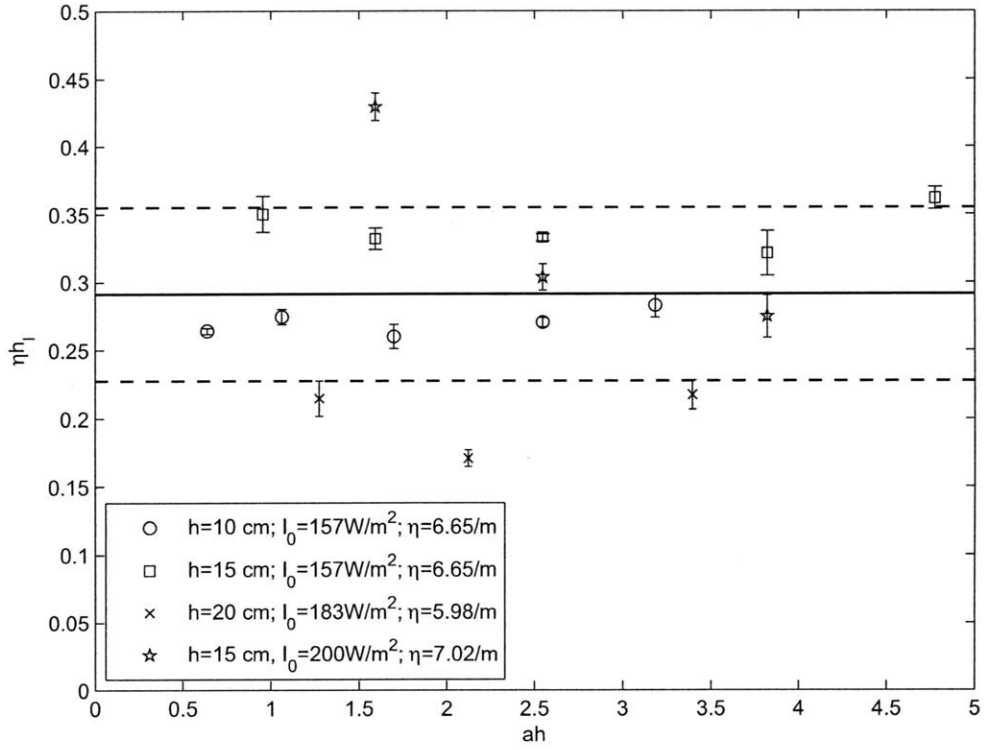

Figure 3.6: Variation of the normalized intrusion depth ηh_I with ah. The error bars show the standard error for each run. The solid line is the average of ηh_I for all cases. The dashed lines are one standard deviation from the average.

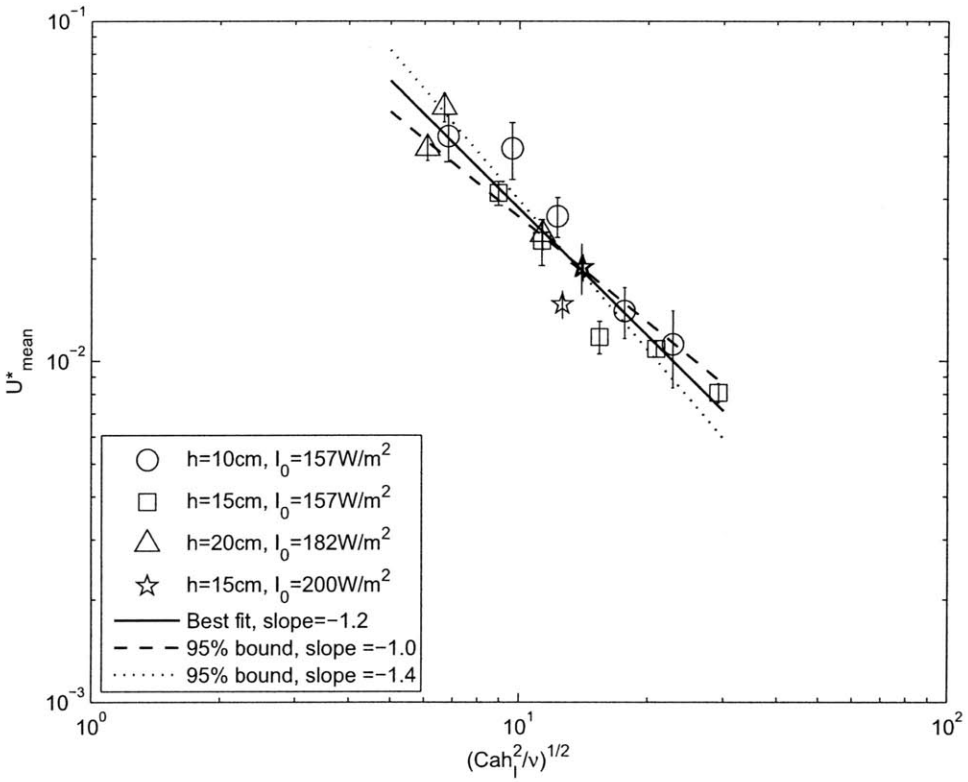

Figure 3.7: Normalized mean intrusion velocity against normalized canopy drag. The error bars show the standard error for each case. The solid line is the theoretical prediction based on (3.10).

Chapter 4

Density Driven Exchange Flow between an Open Water and a Floating Vegetation

Abstract

This experimental study explores how a partial-depth porous obstruction alters the vertical structure and magnitude of the classic density-driven lock-exchange. This model represents the thermally-driven exchange flow that occurs in the field between open water and floating vegetation. Initially, the flow entering the vegetated region bifurcates, with some flow moving through the root layer of the vegetation and the remaining flow displaced downward beneath this layer. Details of flow structure are measured using PIV and reveal that the velocity through the root layer is less than the velocity of the underflow. At long time, however, the flow structure approaches that of a fully blocked layer, with negligible flow within the root layer. A model is developed that predicts the flow rates within the porous layer and the underflow based on energy considerations. The system adjusts the energy loss due to drag dissipation in the root layer and the potential energy cost to displace the underflow beneath the root layer, so that the resulting volumetric exchange is maximized, which also maximizes the kinetic energy. The predicted magnitude of exchange flow expected under field condition is discussed.

4.1 Introduction

Floating vegetation is commonly seen in fresh-water systems, where it has been shown to create micro environments that are chemically distinct from adjacent open water (Ultsch, 1973). In addition to affecting water chemistry, vegetation also impacts phytoplankton and zooplankton biomass, as well as the predation and habitat of fish communities (Adams *et al.*, 2002; Mariana *et al.*, 2003; Padial *et al.*, 2009). In this paper, we consider the role of floating vegetation in the generation of convective water exchange, which may transport water between the chemically distinct regions of open and vegetated water. When solar radiation impinges on an open water surface, the water absorbs solar energy and its temperature increases. In regions with floating vegetation, however, the surface leaves intercept the solar radiation, and shade the water column. The difference in the absorption of solar radiation between an open and vegetated region creates a temperature difference, which in turn generates a density difference. Ultsch (1973) reported temperatures beneath water hyacinths to be as much as 2 degrees Celsius lower than in adjacent open water. Lightbody *et al.* (2008) reported that during daytime the temperature within the marsh region of a constructed wetland remained 2 degrees Celsius lower than the surrounding water. The associated density difference can drive an exchange flow between the open water and the region of vegetation. Lövstedt and Bengtsson (2008) measured temperature differences up to 1 degree Celsius between a reed belt and open water, and verified the existence of an exchange flow with a velocity up to 1.5 cm/s. For a water body that is sheltered from wind, convective exchange flow of this magnitude will dominant the mass exchange between the vegetated area and the open water (Zhang and Nepf, 2009). Floating vegetation in particular tends to live in quiescent regions, where background flow conditions are relatively calm (Azza *et al.*, 2006), so that we anticipate that flow driven by differential shading will be important in regions of floating vegetation.

In addition to causing uneven distribution of thermal radiation, the presence of the aquatic vegetation also adds hydrodynamic drag. Zhang and Nepf (2009) studied

the impact of rooted, emergent vegetation on thermally driven exchange flow, and they showed that the flow magnitude is controlled by the vegetative drag. In contrast to Zhang and Nepf (2009) and Lövstedt and Bengtsson (2008), who considered rooted emergent vegetation, in this paper we consider floating vegetation, for which the root layer extends through only part of the water depth, creating an uneven distribution of drag, which will influence the vertical structure of the exchange flow. For example, Coates and Ferris (1994) created a thermally-driven exchange between a region with the floating plants *Azolla* and *Lemna* and a region of open water. The exchange flow was largely displaced downward beneath the thin root layer ($2-3$ cm), with very little flow within the root layer. More recently, Plew *et al.* (2006) studied the adjustment of ocean current near a suspended aquaculture canopy, which occupied a fraction of the water depth. The strength of the stratification and the horizonal span of the canopy determined whether the incoming flow was diverted downward beneath the canopy or horizontally around it. In this work, we examine how the depth of a root layer changes the vertical distribution of the exchange and influences the volumetric exchange rate. In the next section, we appeal to energy conservation to develop a model that predicts the magnitude of exchange and the depth of the flow beneath the root layer. Section 4.3 describes the experimental setup, which uses a lock exchange to model the exchange flow. Particle Imaging Velocimetry (PIV) is used to measure the velocity field. The comparison between theoretical and experimental results, as well as the extension of theoretical results to field conditions is presented in Section 4.4.

4.2 Model development

Coates and Patterson (1993) studied thermally-driven exchange between a shaded and unshaded region of open water without vegetation. Zhang and Nepf (2009) studied the exchange flow generated by differential light absorption between a region of open water and a region of emergent, rooted vegetation. In both cases, the distribution of light absorption over depth, which follows Beer's Law, produced vertical

variation in temperature, and thus density, in the heated region. Despite this vertical stratification, the exchange flow resulting from the horizontal density difference consisted of a single intrusion and a single return flow at the bed. That is, the presence of mild stratification within the intrusion had no observable influence on the layer structure. Given these observations, we believe that a lock exchange with initially vertically uniform density provides a reasonable surrogate to the natural condition induced by differential light-absorption.

The geometry of the lock exchange model is depicted in Fig. 4.1. We consider a rectangular flow domain with a total depth H and total length $2L_{tank} >> H$ (the figure is not to scale). A removable gate is located at $x = 0$. Initially, the water to the right of the gate has a higher density than the water to the left of the gate. In the lab we generate this density difference with salt addition, and so we label the two densities, ρ_s (with salt addition) and ρ_f (fresh water), shown in white and grey, respectively, in Fig. 4.1. Floating vegetation is present to the right of the gate, and it has a root depth of h_3. The solid volume fraction of the root layer, ϕ, is the ratio of root volume to total volume. The corresponding frontal area per unit volume is denoted $a = Nd/A$, in which d is the root diameter and N is the number of roots per planar area A. The exchange flow is initiated when the gate is removed. The surface current is broken into two layers, flow through the root layer (with depth h_3) and flow beneath the roots (with depth h_2). The return current at the bed has depth h_1. The velocity of each layer is given by u_j, $j = 1, 2, 3$. The length of the current in each layer at a particular point in time is denoted L_1, L_2 and L_3, respectively. The velocity of each layer will be predicted using energy considerations. Modifying the analysis of Benjamin (1968), the potential energy of the system is both converted to kinetic energy and lost to work against the vegetative drag.

For simplicity, we assume the velocity within each layer is vertically uniform and the geometry of each layer is approximated by a rectangle (Fig. 4.1). The continuity equations can then be written as

$$u_2 h_2 + u_3 h_3 = u_1 h_1, \tag{4.1}$$

and

$$h_1 + h_2 + h_3 = H. \tag{4.2}$$

The aquatic vegetation exerts additional drag that retards the flow through the root layer. Consequently, the velocity within the root layer is expected to be slower than the velocity beneath the root layer. We characterize this difference with the following velocity ratio

$$\alpha = u_3/u_2, \tag{4.3}$$

where α is smaller than 1. With the following simplifying assumptions, we can estimate α from the momentum equation. First, it has been shown that when vegetation is present, the viscous drag is negligible compared to the vegetative drag (Tanino *et al*, 2005; Zhang and Nepf, 2008). Second, initially the exchange flow is dominated by inertia (following the classic evolution), but within the root layer the vegetative drag exceeds inertia for $C_D aL > 7$ (Tanino *et al* 2005), in which C_D is the quadratic drag coefficient and L is the length of intrusion into vegetated zone. The inertial transient is discussed in the results, but here, we consider the drag-dominated limit, such that the inertia term is negligible compared to the drag term in the root layer. Finally, we assume that the flow is slowly varying, so that a steady approximation can be made. For two-dimensional steady flow we then have the following equations of momentum,

$$\rho_f u_3 \frac{\partial u_3}{\partial x} = -\frac{\partial P_3}{\partial x} - \frac{1}{2}\rho_f C_D a {u_3}^2, \tag{4.4}$$

$$\rho_f u_2 \frac{\partial u_2}{\partial x} = -\frac{\partial P_2}{\partial x}. \tag{4.5}$$

The equations are scaled by the total pressure difference between the exchanging regions, $\Delta P = (\rho_s - \rho_f)gH$ and by the maximum length-scale of the intruding layers, $x \sim L_2$. Applying these scale parameters and equating Eqs. (4.4) and (4.5) leads to

$$\frac{u_2^2}{L_2} \sim \frac{1}{2} C_D a {u_3}^2, \tag{4.6}$$

from which we can define the velocity ratio,

$$\alpha = K\left(\frac{2}{C_D a L_2}\right)^{1/2}, \tag{4.7}$$

with scale constant K to be determined by experiment.

The rate of change of the total energy (potential and kinetic) in the system is balanced by the energy lost through vegetation drag. We thus have

$$\frac{\partial PE}{\partial t} + \frac{\partial KE}{\partial t} = -Du_3. \tag{4.8}$$

in which PE and KE are the potential and kinetic energy, respectively, and D is the drag due to the root layer. At any point in time, the potential (PE) and kinetic (KE) energy per unit width are given by the following equations,

$$\begin{aligned} PE =& \rho_f g L_{tank} H\frac{H}{2} + (\rho_s - \rho_f)g(L_1 h_1 \frac{h_1}{2}) + \rho_s g L_{tank} H\frac{H}{2} \\ & - (\rho_s - \rho_f)g L_3 h_3 (H - \frac{h_3}{2}) - (\rho_s - \rho_f)g L_2 h_2 (H - h_3 - \frac{h_2}{2}). \end{aligned} \tag{4.9}$$

$$\begin{aligned} KE =& \frac{1}{2}\rho_s {u_1}^2 (L_1 + L_2)h_1 + \frac{1}{2}\rho_f ({u_2}^2 L_2 h_2 + {u_3}^2 L_3 h_3) \\ & + \frac{1}{2}\rho_f (\frac{u_1 h_1}{h_2 + h_3})^2 (h_2 + h_3) L_1. \end{aligned} \tag{4.10}$$

The last term in Eq. (4.10) comes from the flow in the upper layer in the open region (see Fig. 4.1), which supplies the flow into the vegetated region. The velocity in this area is assumed to be uniform and has the magnitude $u_1 h_1/(h_2 + h_3)$ to satisfy continuity. The drag force acting on the fluid inside the vegetation, D, is

$$D = \frac{1}{2} C_D \rho_f {u_3}^2 a h_3 L_3. \tag{4.11}$$

Differentiating Eqs. (4.9) and (4.10) with respect to time, gives the rate of change

in potential and kinetic energy, $\partial PE/\partial t$ and $\partial KE/\partial t$, respectively,

$$\begin{aligned}\frac{\partial PE}{\partial t} &= \Delta\rho g\frac{{h_1}^2}{2}u_1 - \Delta\rho g h_3(H-\frac{h_3}{2})u_3 - \Delta\rho g h_2(H-h_3-\frac{h_2}{2})u_2 \\ &= \rho_s\frac{g'H}{2}u_1\frac{{h_1}^2}{H} - \rho_s g'H\frac{h_3}{H}(H-\frac{h_3}{H})u_3 - \rho_s g'H\frac{h_2}{H}(H-h_3-\frac{h_2}{2})u_2 \\ &= \rho_s 2{u_i}^2u_1\frac{{h_1}^2}{H} - \rho_s 4{u_i}^2u_3\frac{h_3}{H}(H-\frac{h_3}{2}) - \rho_s 4{u_i}^2u_2\frac{h_2}{H}(H-h_3-\frac{h_2}{2}),\end{aligned} \tag{4.12}$$

$$\frac{\partial KE}{\partial t} = \frac{1}{2}\rho_s h_1{u_1}^2(u_1+u_2) + \frac{1}{2}\rho_f(h_2{u_2}^3 + h_3{u_3}^3) + \frac{1}{2}\rho_f\frac{(u_1h_1)^2}{h_2+h_3}u_1, \tag{4.13}$$

where $\Delta\rho = \rho_s - \rho_f$ is the density difference. u_i is the inertial velocity described by Benjamin (1968) for the density-driven exchange flow between two open regions.

$$u_i = (g'H/4)^{1/2}, \tag{4.14}$$

where $g' = (\rho_s - \rho_f)/\rho_s g$ is the reduced gravity. The fact that $u_j = \partial L_j/\partial t$, $j = 1, 2, 3$ are used to derive Eqs. (4.12) and (4.13). Note that when deriving Eq. (4.13), we also assume $\partial u_1/\partial t \approx \partial u_2/\partial t \approx \partial u_3/\partial t \approx 0$. Our experimental measurements justify this simplification.

Following previous studies of exchange flow, we set an additional constraint that the flow adjusts to maximize the exchange. This constraint has been verified by Jirka (1979) and Adams and Cosler (1988), and references therein.

$$\text{Max}(q), \tag{4.15}$$

where q is the flow rate given by

$$q = u_1h_1 = u_2h_2 + u_3h_3. \tag{4.16}$$

We non-dimensionalize the Eqs. (4.1) to (4.3) by normalizing the layer depth by the total water depth H, and the velocities by the inertial velocity, u_i, given in Eq.

(4.14). Specifically, we define

$$(u_1', u_2', u_3') = (u_1, u_2, u_3)/u_i, \qquad (h_1', h_2', h_3') = (h_1, h_2, h_3)/H. \tag{4.17}$$

The primes indicate normalized terms for the rest of this paper. We further normalize Eqs. (4.8) to (4.13) by $\rho_s {u_i}^3 H$, which is the change of kinetic energy per unit width per unit time for the exchange between two open regions. The normalized equations are an optimization problem with an objective function

$$\text{Max}(q') = \text{Max}(u_1' h_1') = \text{Max}(u_2' h_2' + u_3' h_3'), \tag{4.18}$$

subject to

$$\begin{aligned}
&u_2' h_2' + u_3' h_3' = u_1' h_1', \\
&h_1' + h_2' + h_3' = 1, \\
&\frac{\partial PE'}{\partial t'} = 2u_1'(h_1')^2 - 4u_3' h_3'(1 - \frac{h_3'}{2}) - 4u_2' h_2'(1 - h_3' - \frac{h_2'}{2}), \\
&\frac{\partial KE'}{\partial t'} = \frac{1}{2} u_1'^2 (u_1' + u_2') h_1' + \frac{1}{2}\frac{\rho_f}{\rho_s}(h_2' u_2'^3 + h_3' u_3'^3) + \frac{1}{2}\frac{\rho_f}{\rho_s}\frac{u_1'^3 h_1'^2}{h_2' + h_3'}, \\
&\frac{\partial PE'}{\partial t'} + \frac{\partial KE'}{\partial t'} = -\frac{Du_3}{\rho_s {u_i}^3 H} = -\frac{1}{2} C_D \frac{\rho_f}{\rho_s} u_3'^3 h_3' (aL_3), \\
&\frac{u_3'}{u_2'} = \alpha = K(\frac{2}{C_D a L_2})^{1/2}.
\end{aligned} \tag{4.19}$$

In addition, within the condition that satisfies Boussinesq approximation, $\rho_f/\rho_s \approx 1$, so that the normalized solution has no dependence on the the density difference $\Delta\rho$ or the reduced gravity g'. This is because, after normalization by $\rho_s u_i^3 H$, both $\partial KE/\partial t$ and Du_3 are functions of u_i^3, so that these two terms remain in the same proportion even as the density difference $\Delta\rho$ increases. The drag coefficient, C_D is $O(1)$ for all Reynolds number and canopy densities considered here (Tanino and Nepf, 2008). Note that the total domain length L_{tank} drops out of the formulation, so that the result is not dependent on the flow domain, as expected. Finally, if we let $a = 0$, or $h_3 = 0$, we recover the classic solution without vegetation or dissipation, namely,

$u_1 = u_2 = \sqrt{g'H/4}$.

4.3 Experimental procedures

As shown in Fig. 4.2, the experiments were conducted in a Plexiglass tank (200cm(L)× 12.0cm(W) × 20.0cm(H)). The tank has two chambers of equal size, separated by a vertical removable gate. The chambers were filled to 15 cm depth with fresh (left side) and salt water (right side). The density of the fresh water (ρ_f) and salt water (ρ_s) was measured using a hydrometer. As the experiments focused on the impact of the root depth and stem density, the water density difference, $\Delta\rho = \rho_s - \rho_f$, was kept approximately constant across the suite of experiments. In the field, Lightbody *et al.* (2008) and Ultsch (1973) reported a temperature difference of 2 degree Celsius between vegetated regions and nearby open water. This temperature difference corresponds to a density difference of 0.0005g/cm^3. Considering that water depth in freshwater vegetated areas in the field is typically around 1 m, the scale of velocity, $\sqrt{g'H}$, in the field is between 1 cm/s to 4 cm/s. We have selected g' and H to produce a similar velocity scale in the laboratory tank.

The right side of the tank was covered by a perforated PVC board. Dowels with diameter $d = 0.6$cm were pushed through holes in the board. The dowels, representing the root layer, extended a finite depth into the water. The holes on the PVC board were randomly distributed. Each hole on the board was assigned a number, and a program was used to draw a subset of the holes to create a certain density. The stem density of the model vegetation ranged from $\phi = 5\%$ ($a = 6.4\text{m}^{-1}$) to $\phi = 15\%$ ($a = 31.8\text{m}^{-1}$). In the field, the solid volume fraction ϕ ranges from 1% for water lily to 45% for mangroves (Mazdda *et al.*, 1997). The root density for floating vegetation has not been reported in the literature, but is expected to fall into a similar range. The root layer thickness was varied to explore two fractional depth, 13% and 28% of the water depth. In the field, the thickness of the root layer ranges from 10 cm to 80 cm (M. Downing-Kunz, personal communication), or roughly 10% to 80% fractional depth. For each penetration depth, experiments were conducted

for five different root densities from $\phi = 5\%$ to $\phi = 15\%$. Two experiments (case S1 and S2 in Table. 4.1) were also conducted for $\phi = 100\%$ to explore the limit of a fully blocked region. In these two cases, a solid block was inserted into the right side of the tank to a depth of h_3. The experimental parameters are summarized in Table. 4.1.

Flow visualization with dye was used to examine the transition from the initial inertial response to the drag-dominated response. The fresh water was dyed with fluorescein. The vegetated region was illuminated through the tank bottom by an ultra-violet light. A CCD camera was positioned to captured the exchange flow at the middle of the vegetated region. The pictures were taken at 5 fps. In this case, the floating vegetation had a solid volume fraction of 8% and a fractional penetration of 28% of the total water depth. The density of the fresh and salt water were 0.9975 g/cm^3 and 0.9985 g/cm^3, respectively. After the toe of the intruding current passed the visualization window, a second tracer, crystalline *Potassium Permanganate*, was dropped in the middle of the visualization window to generate a vertical streak. The subsequent distortion of this streak revealed the shape of the vertical velocity profile at this later time.

Detailed profiles of velocity in the drag dominated regime ($C_D aL > 7$) were acquired using Particle Imaging Velocimetry (PIV). Pliolite particles with a density of 1.02 g/cm^3 were added to the water. To visualize the flow in the root layer, it was necessary to create a 5 cm wide gap starting 40 cm from the gate. The width of the gap was chosen to reliably calculate the velocity field, and at the same time, to minimize the impact of the gap on the flow inside the root layer. A laser sheet entering through the bottom of the tank illuminated the interrogation region for PIV. The exchange flow velocity was $O(1)$cm/s, so that the settling of the particles can be neglected, because the settling velocity ($O(0.01)$ cm/s) was much smaller than the flow velocity. The movement of the particles was captured using a Sony CCD camera with a resolution of 1024×768 at a frame rate of 5 fps. The image acquisition was started once the intrusion passed the window. The images obtained were later processed by MatPIV v. 161 to produce the velocity field. For each case, we collected 50 to 60

instantaneous velocity profiles, which corresponds to 10 to 12 sec of measurements. A velocity profile was extracted from left edge of the PIV window, closest to the vegetation. The total thickness of the intruding current, h, was measured from the surface to the point where the velocity changes its direction from inflow to outflow. The intrusion depth below the root layer, h_2, was then calculated by subtracting the thickness of the root layer h_3, *i.e.* $h_2 = h - h_3$. The measured discharge rates were estimated by integrating the velocity profile from the bottom to the point where the flow changes from outflow to inflow. We confirmed that the inflow and outflow agreed, with less than 5% difference, indicating the the conservation of volume is satisfied.

The following procedure was used to compare measured discharge rates to our theoretical prediction. The velocity measurements were made as the front moved between L_g and $2L_g$, where $L_g = 42.5$ cm is the position of the middle of the PIV window. For simplicity we assign each case the single length scale L_g. For the duration of the experiments (10 s), the intrusion length changed by less than 40 cm. The drag coefficient, C_D, was determined from values reported in Koch and Ladd (1997) and Tanino and Nepf (2008) for randomly distributed cylinder arrays with uniform cylinder diameter, for Reynolds number ranging from $O(1)$ to O(100) and solid volume fraction 5% to 35%. The relationship between the drag coefficient and the stem Reynolds number, $Re_d = ud/\nu$, is given by the following equation,

$$C_D = 2(\frac{\alpha_0}{Re_d} + \alpha_1), \tag{4.20}$$

where α_0 and α_1 are empirical parameters which depend upon the solid volume fraction ϕ. Using Eq. (4.20), an drag coefficient was determined for each experiment (Table. 4.1). Finally, from the set of feasible solutions is computed by Eq. (4.19), we select the solution that maximized exchange. The theoretical discharge rate can be calculated from Eq. (4.16) and is compared to the measured discharge rate.

4.4 Results

Tanino *et al.* (2005) identified the transition from inertial to drag-dominated flow within an array of cylinders. They showed that the array drag eclipsed inertia when $C_D aL > 7$, where L is the length of the intruding current.. We confirmed this transition for partial depth arrays using dye visualizations, *e.g.* as shown in Fig. 4.3. Fig. 4.3(a) depicts the region from $x = 30$ cm to 55 cm. It shows the shape of the current as the front of the current just arrived at this location. The leading edge of the tracer within the root layer is ahead of that in the region beneath the root layer, indicating that up to this time the velocity in the root layer was higher than that beneath the root layer. At the time corresponding to this image, $C_D aL_3 = 7$, so that the system has just reached the drag dominated limit, but leading up to this time it was in the inertial regime. Fig. 4.3(b) shows the flow after the transition to drag-dominated regime, specifically $C_D aL_3 \approx 18$. For this condition, the intruding current has a uniform depth, and specifically exhibits a horizontal interface. In addition, the second tracer shown in Fig. 4.3(b) reveals that the velocity beneath the root layer is now higher than that inside the root layer. The velocity profile is indicated by the tracer distortion (dashed line) from the initial vertical line (solid line). The dashed line within the rooted layer is the velocity profile from PIV measurement, scaled to match the dye streak. The velocity profile shown in Fig. 4.3(b) represents the drag-dominated limit which is the focus of our predictive model, and which we explore further with PIV measurements.

The time-averaged velocity profile for case 2 is shown in Fig. 4.4. In this case the roots extended 2 cm beneath the surface, producing a fractional penetration of 13%. The errorbars give the standard error of the individual measurements made over the 10 sec averaging period. The flow velocity within the root layer (above 13 cm) is between 0.5 cm/s to 1.5 cm/s, and the flow velocity beneath the vegetation layer is approximately 3.0 cm/s. Fig. 4.5 shows the time-averaged velocity profile for case 7, which has a root layer over 28% of the flow depth. The intruding current again bifurcates into a distinct flow within the root layer and beneath it with $u_3 < u_2$.

The scale analysis suggests that the velocity ratio $\alpha = u_3/u_3$ is dependent on the root density a, but not the root depth, h_3 (Eq. (4.7)). To verify this relationship, we first estimate the velocities u_3 and u_2 from the measured velocity profiles. The velocity in the root layer, u_3, was estimated for each instantaneous velocity profile as the average of the velocity over h_3, the root layer thickness. The flow velocity beneath the vegetation, u_2, was defined as the maximum intruding velocity beneath the floating vegetation. The maximum is chosen as the best estimate of the velocity in this layer in the absence of viscosity, which is neglected in the model development. The measured values for u_2 and u_3 are listed in Table. 4.2. The uncertainty represents the standard deviation among the $50 - 60$ instantaneous values recorded.

The measured α are plotted against $C_D a L_g$ in Fig. 4.6 for cases 1 to 10. The velocity ratio changes with the density of the root layer, but within uncertainty is not sensitive to the root layer thickness. This agrees with Eq. (4.7). We used the estimated values of C_D to fit a single curve to Eq. (4.7) and determined $K = 0.75 \pm 0.04$. When the floating vegetation becomes dense, or $C_D a L$ becomes large, the velocity within the root layer becomes negligibly small such that the behavior of the exchange flow approaches limit of a fully blocked layer. To verify this approach to fully blocked conditions, we compare the velocity profiles for case 10 and S2 in Fig. 4.7. For case 10, $\phi = 15\%$ and $C_D a L = 62$, the velocity inside the root layer is essentially zero, and the shape of the velocity profile beneath the root layer is similar to that of the case S2 in which the floating layer is fully blocked.

With the input α from Eq. (4.7), our theoretical model Eqs. (4.18) and (4.19) find the optimal value for h_2 and u_2 that will maximize exchange (Table. 4.3). The model also reveals that maximal exchange corresponds to the maximum rate of conversion to kinetic energy, *i.e.* maximum $\partial KE/\partial t$. The layer depth, h_2' predicted by using both criteria give the same results (see Table. 4.3). This can be explained by the fact that $KE = 0$ initially, and maximum exchange corresponds to maximum kinetic energy.

The predicted discharge rate, using Eq. (4.16), is compared to the measured discharge rate in Table. 4.3 and plotted in Fig. 4.8. The model tends to over-

predict the discharge rate by about 20%. This can be explained by the fact that viscosity is neglected in our model. Viscosity similarly reduces the magnitude of exchange in open conditions. The theoretical prediction of the exchange velocity between two unobstructed regions is $u_i = 0.5\sqrt{g'H}$ (Benjamin, 1968), but reported experimental measurements are consistently lower, *e.g.* $u_i = 0.42\sqrt{g'H}$ (Shin *et al.*, 2004). This means that the case with no root layer is overpredicted by theory, specifically, $q_{\text{measured}}/q_{\text{predicted}} \approx 0.84$. In our own tank we have observed that $q_{\text{measured}}/q_{\text{predicted}} \approx 0.85 \pm 0.10$ in the absence of vegetation (Fig. 4.8). This degree of overprediction is consistent with our experimental observations, supporting our conclusion that the neglect of viscosity is to blame.

In the field, floating vegetation typically exists as a belt of vegetation along the shoreline. Ultsch (1973) reported temperature difference of 2 degree Celsius between water beneath a patch of water hyacinth and adjacent open water. This corresponds to a density difference of $5 \times 10^{-4}\text{g/cm}^3$. The typical water depth in the shallow band of a lake is approximately 1 m. For a floating vegetation with 10% solid volume fraction, 20% fractional penetration and $L \approx 10$ m, the model predicts an intruding velocity beneath the floating vegetation to be 3cm/s. During a diurnal cycle, this exchange flow can flush $L \rightarrow O(100)$m. It has been observed that in the Finniss River of Australia, the floating vegetation mat extended a maximum of 65 m from the bank (Hill *et al.*, 1987). Lövstedt and Bengtsson (2008) reported that that width of reed belt in Lake Krankejön in southern Sweden was 40 m. Considering the width of the vegetated band observed in field, $O(10)$m to $O(100)$m, the exchange flow can fully flush the area each day.

In field applications, the drag coefficient C_D and the solid volume fraction ϕ of root layer are not easily measured directly. However, field conditions will often approach the fully-obstructed limit (e.g. as shown in Fig. 4.7), because the length-scale of the intrusion is large, producing large $C_D aL$. Specifically, in the field the intrusion may run for $O(10)$ hours, *i.e.* the duration of solar heating, producing intrusion lengths of 10 to 100m, as described in the previous paragraph. The normalized discharge rate $q/u_i H$ for different penetration depths and root layer stem density are shown in Fig.

4.9. The drag coefficient C_D is chosen to be 1, for simplification. As the density of the floating layer becomes higher or the length of the intrusion becomes longer, the magnitude of the discharge rate decreases. As either ϕ or L becomes very large, the discharge approaches the case when the floating layer is fully blocked (indicated by the solid line in Fig. 4.9). This is consistent with our observation that the velocity structure with dense floating vegetation approaches that of a fully blocked layer (Fig. 4.7). The theoretical curve for the blocked case was computed by setting $\phi = 100\%$ in the model. The curves suggest that predictions made using the fully-blocked limit are reasonable (within 50%), even for sparse vegetation. Therefore, reasonable predictions can be made for field conditions using only the root layer depth, the water depth, and the thermal forcing.

4.5 Conclusion

Differential heating between regions of open water and adjacent regions of floating vegetation can produce density-driven exchange. The magnitude of the exchange depends on the density difference, the root layer depth and vegetation drag, parameterized by $C_D aL$. As the intrusion length scale, L, increases, the flow behavior approaches that for a fully blocked layer, for which the normalized flow depends only on the root layer depth. A model developed to predict the discharge slightly overpredicted the measured discharge, and this is attributed to the neglect of viscosity. The range of discharge magnitude estimated for field conditions suggests that this flow could provide daily flushing of vegetated regions, which could significantly impact the water chemistry of the lake system.

Table 4.1: Summary of experimental parameters. The uncertainty of ρ_f and ρ_s is ($\pm 0.0005 \mathrm{g/cm^3}$).

Case	ϕ	a ($\mathrm{m^{-1}}$)	Penetration	ρ_f	ρ_s	C_D
1	0.03	6.4	0.13	0.9980	1.0000	2.0
2	0.05	10.6	0.13	0.9985	0.9995	2.4
3	0.08	16.9	0.13	0.9990	1.0000	2.7
4	0.10	21.2	0.13	0.9975	0.9990	3.0
5	0.15	31.8	0.13	0.9985	1.0005	3.5
6	0.03	6.4	0.28	0.9985	1.0000	2.0
7	0.05	10.6	0.28	0.9985	0.9995	2.5
8	0.08	16.9	0.28	0.9975	0.9985	2.4
9	0.10	21.2	0.28	0.9975	0.9990	3.3
10	0.15	31.8	0.28	0.9985	0.9995	4.6
S1	1.00	∞	0.13	0.9980	1.0000	∞
S2	1.00	∞	0.28	0.9980	1.0000	∞

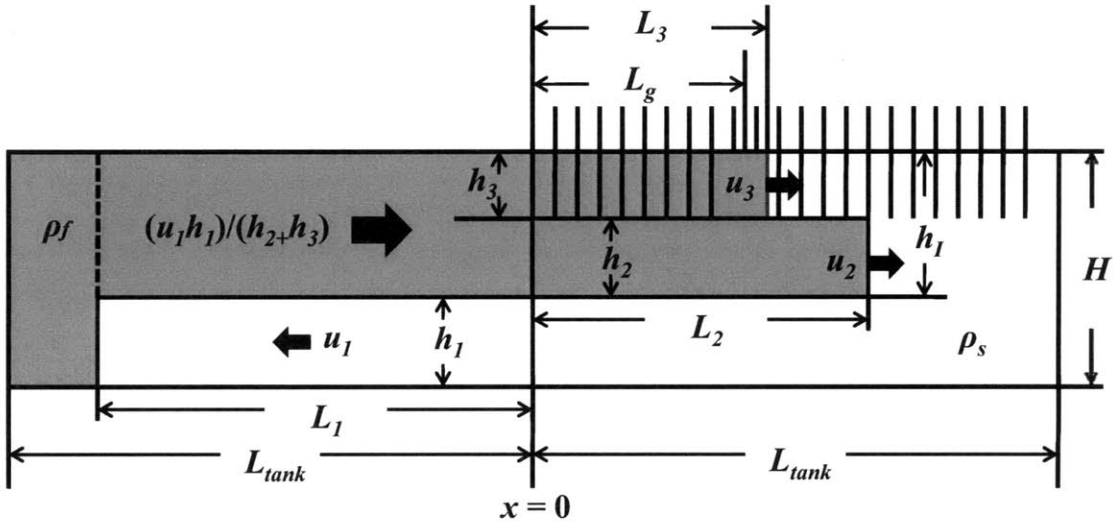

Figure 4.1: Geometry of the flow domain.

Table 4.2: Summary of experimental results of case 1 to 10

Case	u_i(cm/s)(theory)	u_1(cm/s)	u_2(cm/s)	u_3(cm/s)	h_2(cm)
1	2.7 ± 0.5	1.8 ± 0.3	2.6 ± 0.3	1.2 ± 0.2	5.0 ± 0.4
2	1.9 ± 0.7	1.7 ± 0.2	3.0 ± 0.4	0.8 ± 0.3	4.5 ± 0.3
3	1.9 ± 0.7	2.0 ± 0.3	2.7 ± 0.4	0.5 ± 0.3	5.6 ± 0.4
4	2.4 ± 0.6	1.8 ± 0.2	2.8 ± 0.4	0.4 ± 0.3	5.6 ± 0.3
5	2.7 ± 0.5	2.7 ± 0.3	3.1 ± 0.4	0.6 ± 0.5	5.9 ± 0.7
6	2.4 ± 0.6	1.4 ± 0.2	2.4 ± 0.3	1.2 ± 0.2	2.5 ± 0.2
7	1.4 ± 1.0	1.5 ± 0.2	2.4 ± 0.4	0.7 ± 0.3	3.6 ± 0.6
8	1.9 ± 0.7	1.7 ± 0.2	3.0 ± 0.3	0.8 ± 0.3	3.8 ± 0.6
9	2.4 ± 0.6	1.9 ± 0.3	2.8 ± 0.4	0.8 ± 0.3	3.0 ± 0.3
10	1.9 ± 0.7	1.7 ± 0.3	2.6 ± 0.6	0.4 ± 0.5	4.6 ± 0.8
S1	2.7 ± 0.5	2.1 ± 0.2	1.8 ± 0.8	N/A	5.3 ± 1.0
S2	3.3 ± 0.4	2.0 ± 0.2	2.7 ± 0.6	N/A	4.6 ± 0.4

Table 4.3: Comparison of theoretical and measured discharge rate for case 1 to 10

Case	h_2' $Max(q)$	h_2' $Max(\frac{\partial KE}{\partial t})$	h_2' (measured)	q(cm^2/s) (predicted)	q(cm^2/s) (measured)
1	0.42	0.42	0.34 ± 0.03	17.9 ± 3.2	12.6 ± 1.7
2	0.43	0.43	0.31 ± 0.02	12.7 ± 4.5	13.2 ± 1.8
3	0.43	0.43	0.37 ± 0.03	12.7 ± 4.5	12.0 ± 1.8
4	0.44	0.44	0.38 ± 0.02	15.2 ± 3.9	11.8 ± 1.4
5	0.44	0.44	0.39 ± 0.05	17.5 ± 3.1	15.3 ± 1.6
6	0.31	0.31	0.16 ± 0.01	14.2 ± 3.3	9.5 ± 1.2
7	0.32	0.32	0.22 ± 0.04	7.9 ± 5.6	9.2 ± 1.7
8	0.33	0.33	0.22 ± 0.04	10.9 ± 3.9	10.0 ± 1.4
9	0.33	0.33	0.20 ± 0.02	13.4 ± 3.4	11.6 ± 1.5
10	0.34	0.34	0.29 ± 0.06	10.4 ± 3.7	10.4 ± 1.5
S1	0.45	0.45	0.35 ± 0.07	17.1 ± 3.2	12.8 ± 1.2
S2	0.37	0.37	0.31 ± 0.03	14.7 ± 1.9	10.1 ± 1.0

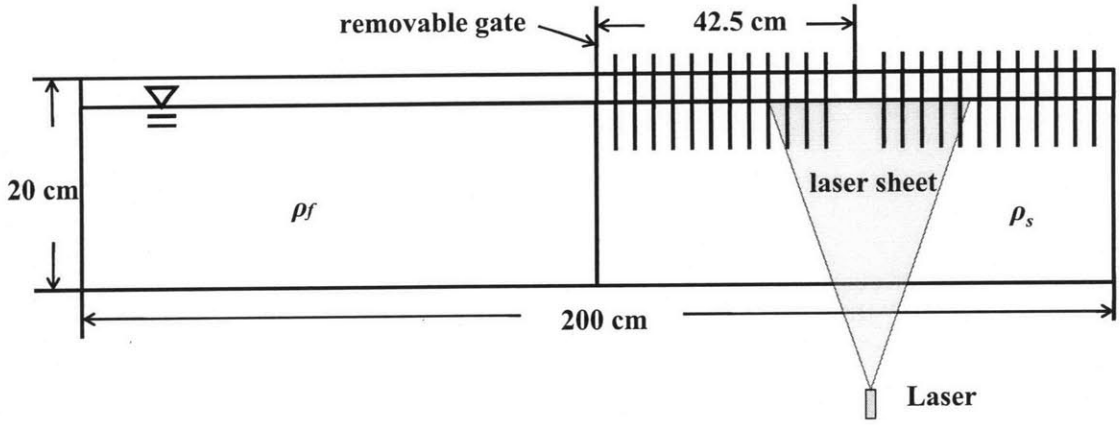

Figure 4.2: A sketch of the experimental setup. Not drawn to scale.

(a)

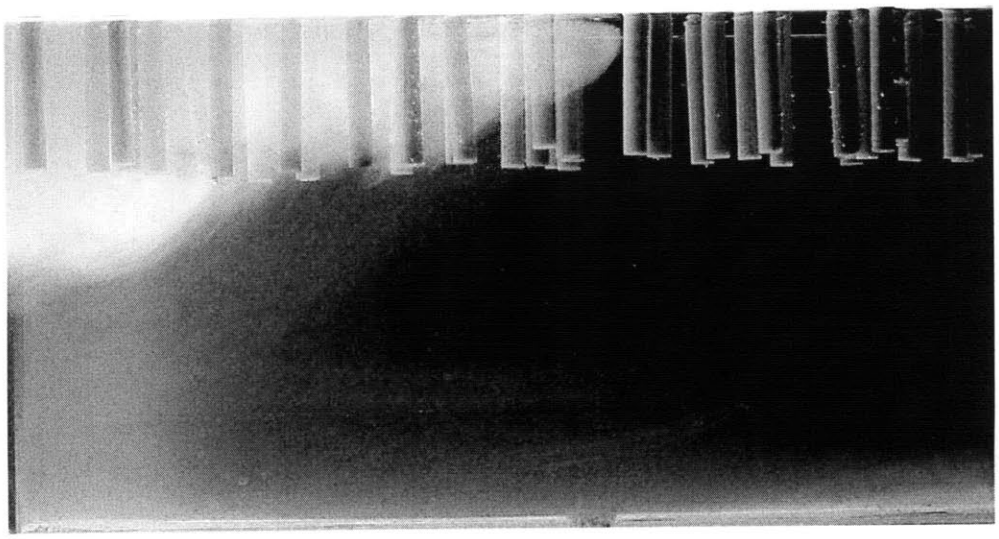

(b)

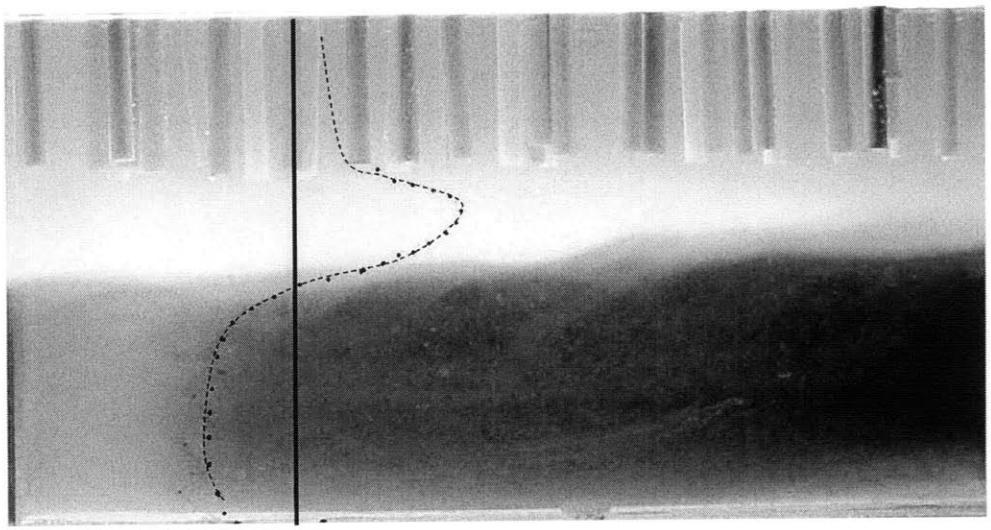

Figure 4.3: Flow visualization using fluorescein and crystalline *Potassium Permanganate* as tracers. The domain corresponds to $x = 30 - 55$ cm and $z = 0 - 15$ cm. (a) At $t \approx 10$ sec after gate is lifted, the intruding current arrives. (b) At $t \approx 30$ sec, the front is beyond the visualization window. The solid line indicates the position of the original streak of the *Potassium Permanganate*. The dots indicate the shape of the dye streak 30 sec later. The dashed line is estimated from PIV measurement for the same solid volume fraction and penetration depth (scaled to match the dye streak).

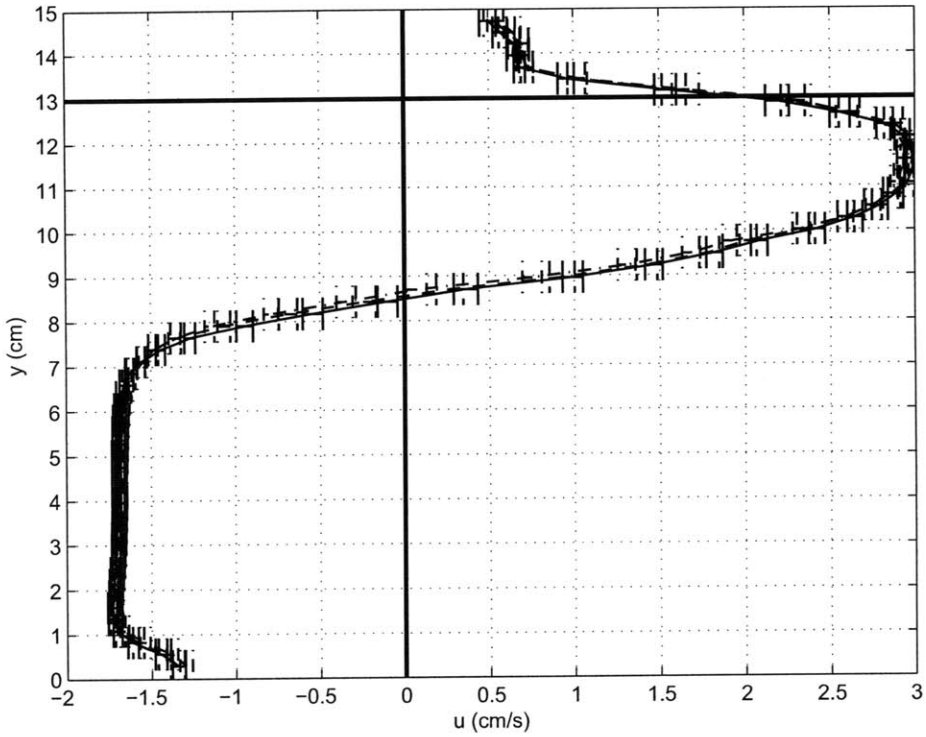

Figure 4.4: Time evolution of the averaged horizontal velocity profiles over 10 sec for case 2 ($\phi = 5\%$ with 13% penetration). The bottom of the floating vegetation is at 13 cm. Errorbars indicate the standard error the velocity measurement. solid line: averaged velocity profile from 4 to 14 sec; dashed line: averaged velocity profile from 6 to 16 sec; dash-dotted line: averaged velocity profile from 8 to 18 sec.

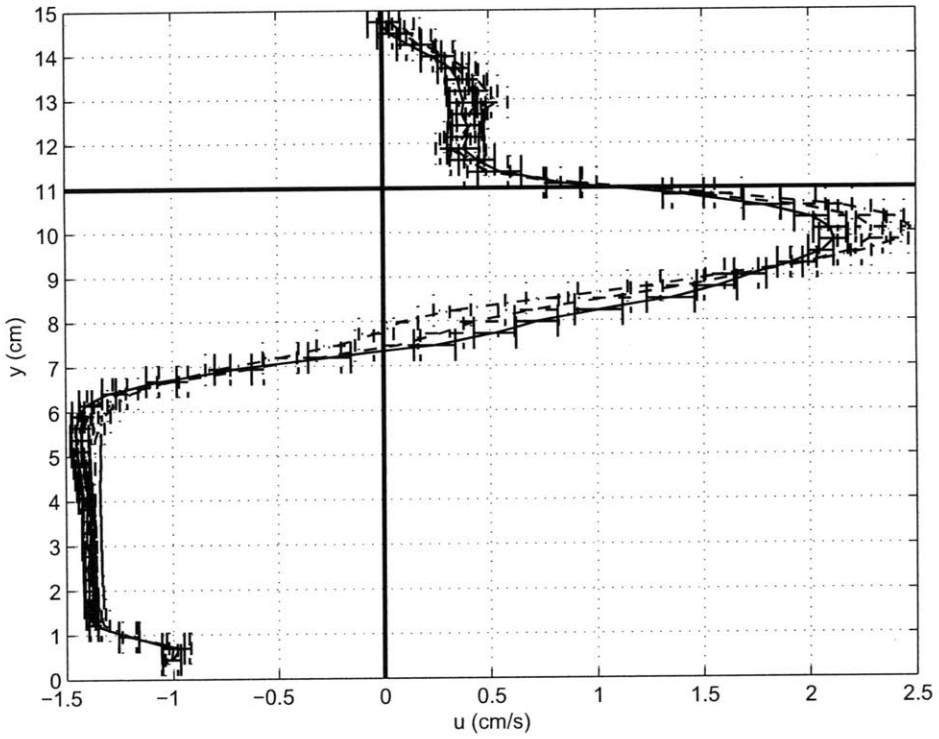

Figure 4.5: Time evolution of the averaged horizontal velocity profiles over 10 sec for case 7 ($\phi = 5\%$ with 28% penetration). The bottom of the floating vegetation is at 11 cm. Errorbars indicate the standard error the velocity measurement. solid line: averaged velocity profile from 6 to 16 sec; dashed line: averaged velocity profile from 8 to 18 sec; dash-dotted line: averaged velocity profile from 10 to 20 sec.

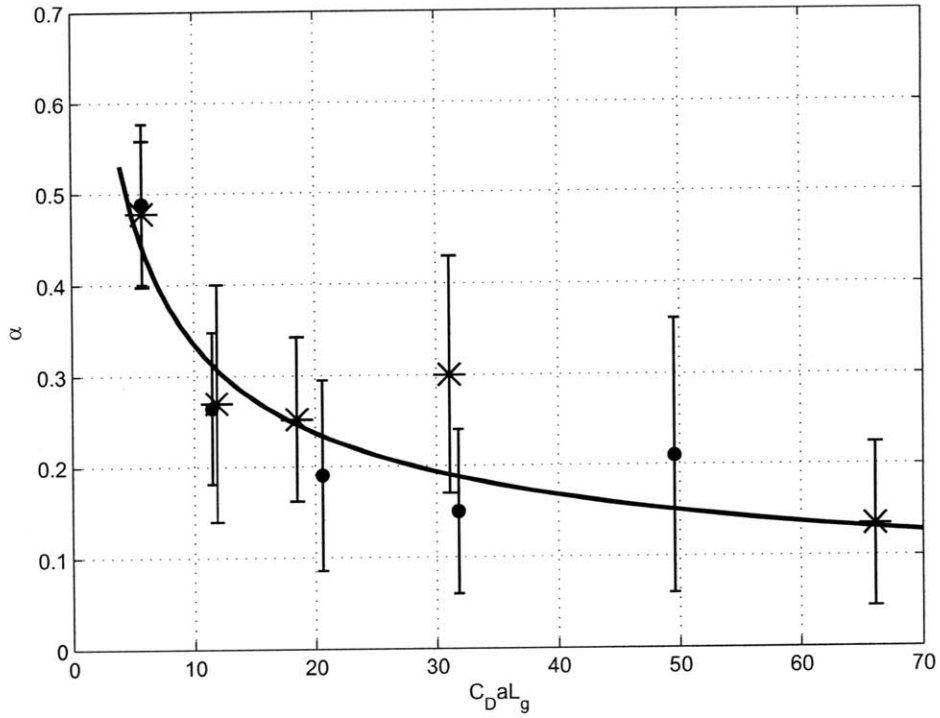

Figure 4.6: The experimental measurements of the velocity ratio α for case 1 to 5 ($\bullet$) and for case 6 to 10 ($*$). The solid line is the best fit using Eq. (4.7). The scaling constant K is equal to 0.75 ± 0.04.

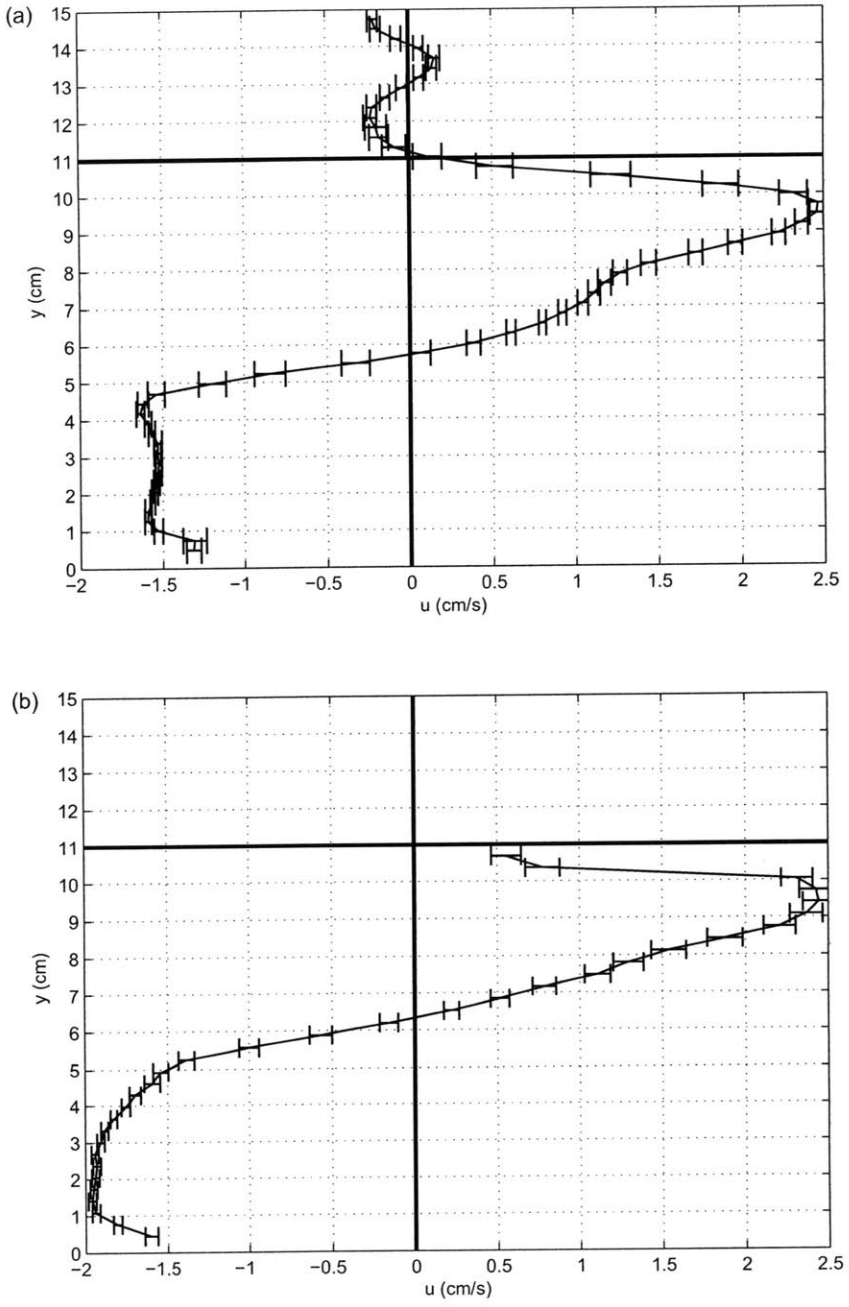

Figure 4.7: (a) Averaged horizontal velocity profiles from 8 - 18 sec for case 10 ($\phi = 15\%$ with 28% penetration). (b) Averaged horizontal velocity profiles from 8 - 18 sec for case S2 (fully blocked with 28% penetration).

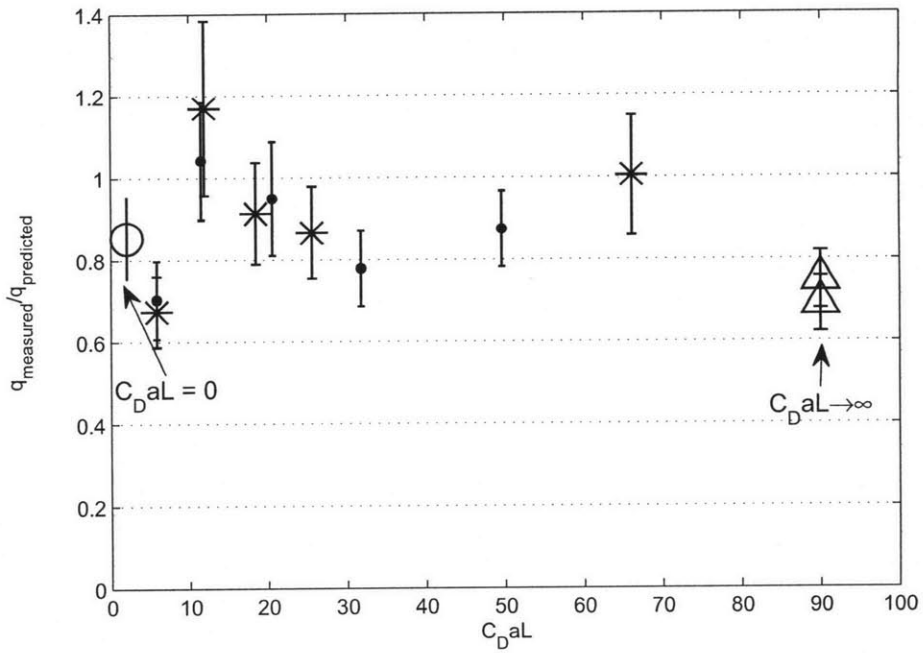

Figure 4.8: Plot of the $q_{\text{measured}}/q_{\text{predicted}}$ versus C_DaL. Cases 1 to 5 (dot); cases 6 to 10 (asterisk); cases S1 and S2 (triangle); pure open case (open circle). $q_{\text{measured}}/q_{\text{predicted}} = 0.87 \pm 0.15$ for all cases.

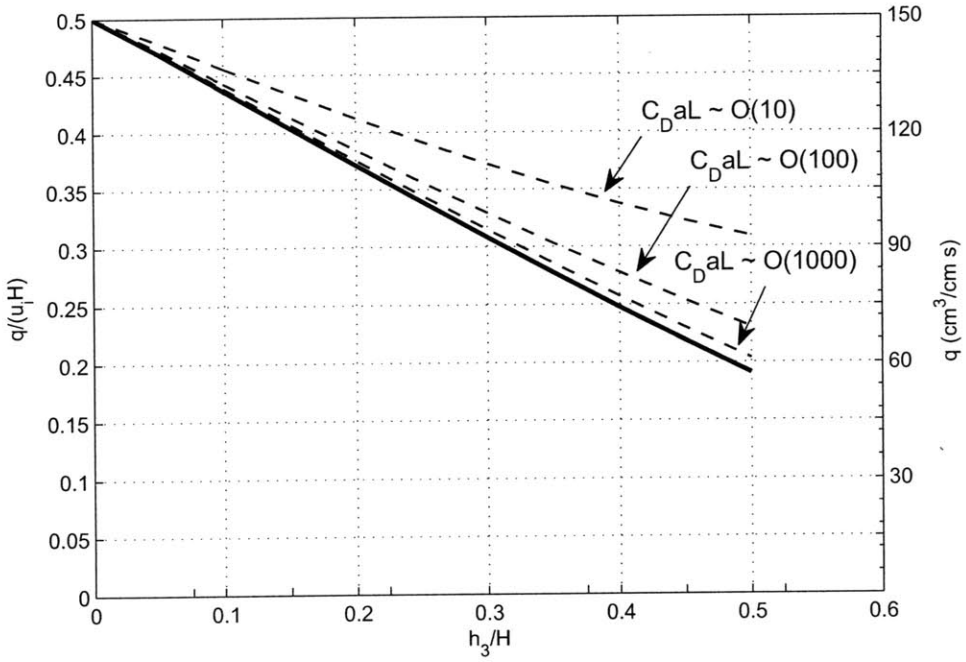

Figure 4.9: Variation of normalized discharge rate q/u_iH versus fractional penetration depth h_3/H for different values of C_DaL (dotted line). The right axis shows the corresponding discharge rate per unit width in physical unit (cm^2/s), for $\Delta T = 2°C$ and $H = 1$ m. The solid line is for the case when the floating layer is fully blocked, which gives the lower bound of the discharge rate for a certain fractional penetration.

Chapter 5

Summary

This thesis explored several regimes of density-driven exchange flow that are likely to occur in natural systems where aquatic vegetation provides shade to the water column. The three studies are summarized below.

First, a lock-exchange experiment was used to study the exchange flow between the open and a canopy of emergent vegetation. In this case the density difference between open water and vegetated water is constant in time, *i.e.* $g' \neq f(\text{time})$. During the initial stage of the flow, the system is controlled by the balance between buoyancy and inertia. The exchange flow in both the open and the vegetated region resemble the classic unobstructed lock exchange flow as studied by Benjamin (1968). After this initial transient, the intruding flow into the vegetated region is controlled by the balance between buoyancy and vegetative drag. The transition to drag-dominated regime occurs when $C_D aL > 7$ (Tanino *et al.*, 2005). Because of the additional drag exists only in the vegetated region, the exchange current in the open and vegetated region exhibit asymmetry. The toe of the current in the open region is still controlled by inertia and continues to propagate at a constant speed set by the initial inertial condition. The exchange flow in the vegetated region has a triangular shape, indicating a linear velocity profile. The toe in the canopy decelerates over time and the deceleration is related to the vegetative drag. Specifically, the toe velocity within the canopy as well as the discharge rate decrease with a increasing vegetative drag.

Second, the exchange flow driven by differential solar heating was studied by cre-

ating model solar radiation using theater lights. In this case the density difference of water between an open and vegetated region grows gradually in time through uneven absorption of solar radiation. In the vegetated region, the incoming solar radiation is blocked by the emergent portion of the vegetation. In the open area, the solar radiation can be absorbed by the water. The transmission of solar radiation in water is governed by Beer's Law. Compared to the previous case, the density difference of water and hence the buoyancy is time-varying and therefore $g' = f(\text{time})$. Using scaling analysis, three distinct flow regimes were identified. Initially, the flow is in the inertia-dominated regime, which is characterized by the balance between inertia and buoyancy. After this transient, the flow enters the drag-dominated regime, which is characterized by the balance between buoyancy and vegetative drag. Scaling analysis verified by experiment shows that once the flow has entered the drag-dominated regime, the exchange flow velocity into vegetated region is constant in time. This occurs because both the thermal forcing (driving force) and the vegetative drag experienced by the exchange current increase linearly in time, and these two terms balance one another. The energy-limiting regime occurs when the incoming heat flux into the open region is in balance with heat flux being transported into the vegetated region though advection. Coates and Patterson (1993) have shown that when there is no vegetation, the inertia-dominated regime is followed by the energy-limiting regime. However, the analyses presented in this thesis show that in the presence of the aquatic vegetation the energy limiting regime is unlikely to occur during a diurnal cycle. Finally, the thickness of the intruding current into the vegetation is set by the length scale of light penetration.

Lastly this thesis described the exchange flow that results from the presence of floating vegetation, for which the roots extend from the surface through only part of the water depth. In this case, the vegetative drag is not uniformly distributed over the water depth. The intruding current into the vegetated side bifurcates, with some flow moving through the root layer, and the remaining flow directed beneath the root layer. Flow visualization has shown that after the initial inertial stage has passed, the current entering the root layer is moving at a slower speed than the current

going beneath the root layer. A model to predict the magnitude of exchange and some aspects of flow structure was developed using energy conservation. After the exchange flow has been initiated, the potential energy of the system is converted into kinetic energy and losses to vegetative drag. The system selects the flow distribution that optimizes the conversion to kinetic energy. Using the model, we have also shown that the condition of maximizing energy conversion is equivalent to maximizing flow rate, which is generally used in the literature when studying maximum exchange. If the roots of the floating vegetation extend beyond 50% of the water depth, the exchange flow is dynamically similar to the case with rooted, emergent vegetation (i.e. vegetation over the full depth), and the theory developed for exchange flow between open water and emergent vegetation can be used to predict the volumetric exchange.

Using field data to characterize the potential thermal gradients between the vegetated and open regions, the models developed above predict exchange flow on the order of 0.1 to 1 cm/s. With this velocity scale and the diurnal time-scale for solar forcing, the presence of vegetation is expected to produce exchanges that impact spatial scales of $O(100)$ m. These scales suggest that thermally-driven exchange flow can be an important mechanism in setting lake-scale chemical budgets and ecology, especially in a protected water body with weak wind condition.

Appendices

Appendix A

Averaged velocity profiles for cases in Chapter 4

Measurements of velocity profiles for cases 1 to S2 in Chapter 4 are shown in this section. All the velocity profiles presented are averaged velocity profiles over 10 seconds, starting from 8 seconds after the exchange current passed the visualization window. Detail experimental parameters are listed in Table A.1.

Table A.1: Summary of experimental parameters for cases in Chapter 4. The uncertainty of ρ_f and ρ_s is ($\pm 0.0005 \mathrm{g/cm^3}$).

Case	ϕ	a ($\mathrm{m^{-1}}$)	Penetration	ρ_f	ρ_s	C_D
1	0.03	6.4	0.13	0.9980	1.0000	2.0
2	0.05	10.6	0.13	0.9985	0.9995	2.4
3	0.08	16.9	0.13	0.9990	1.0000	2.7
4	0.10	21.2	0.13	0.9975	0.9990	3.0
5	0.15	31.8	0.13	0.9985	1.0005	3.5
6	0.03	6.4	0.28	0.9985	1.0000	2.0
7	0.05	10.6	0.28	0.9985	0.9995	2.5
8	0.08	16.9	0.28	0.9975	0.9985	2.4
9	0.10	21.2	0.28	0.9975	0.9990	3.3
10	0.15	31.8	0.28	0.9985	0.9995	4.6
S1	1.00	∞	0.13	0.9980	1.0000	∞
S2	1.00	∞	0.28	0.9980	1.0000	∞

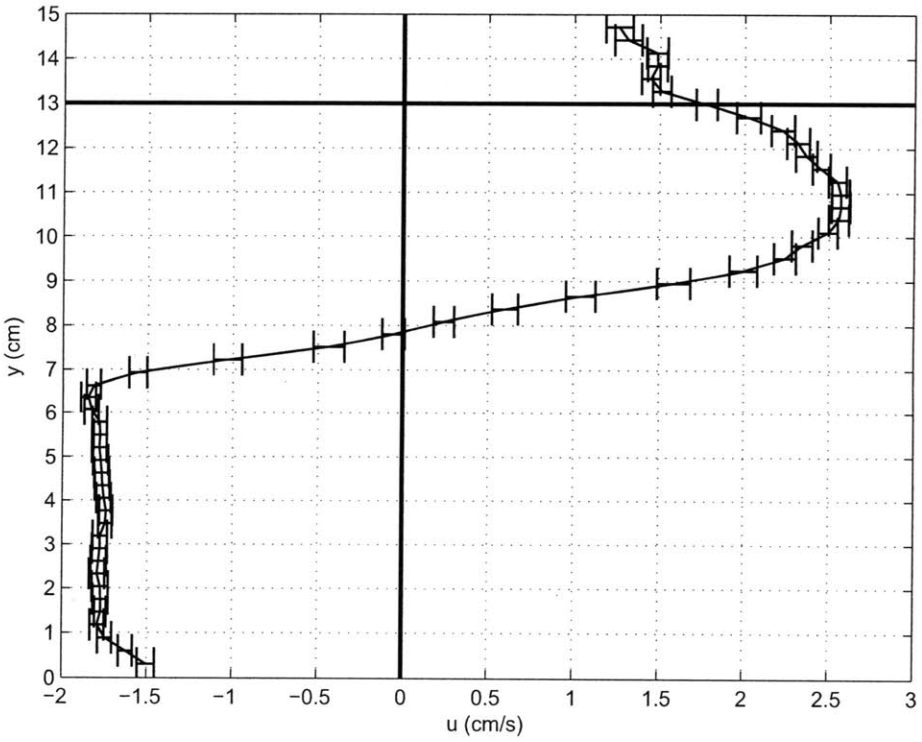

Figure A.1: Averaged velocity profile for case 1.

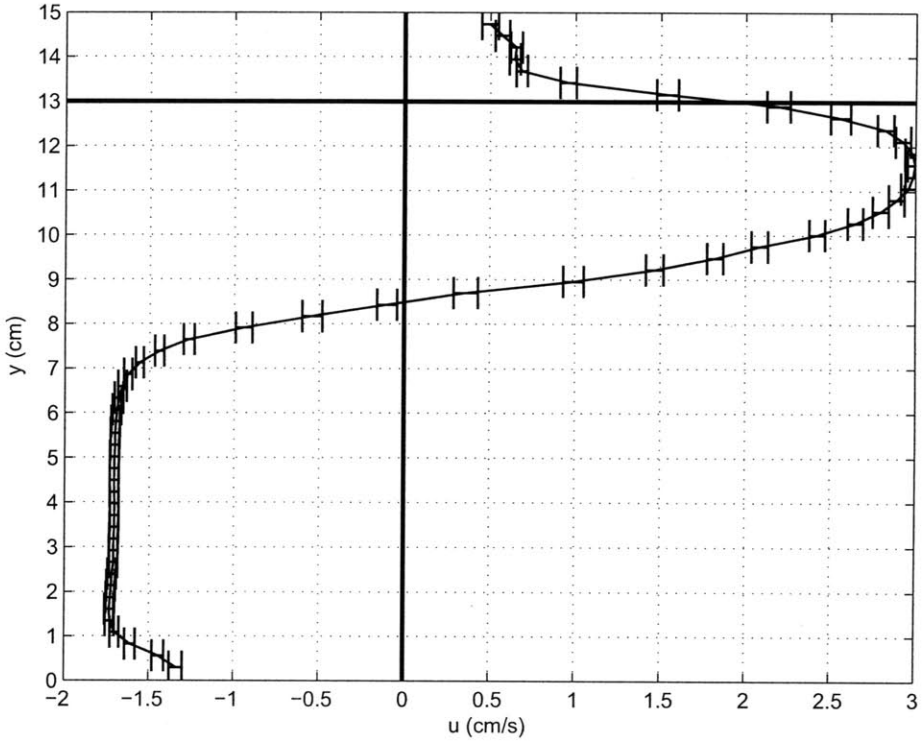

Figure A.2: Averaged velocity profile for case 2.

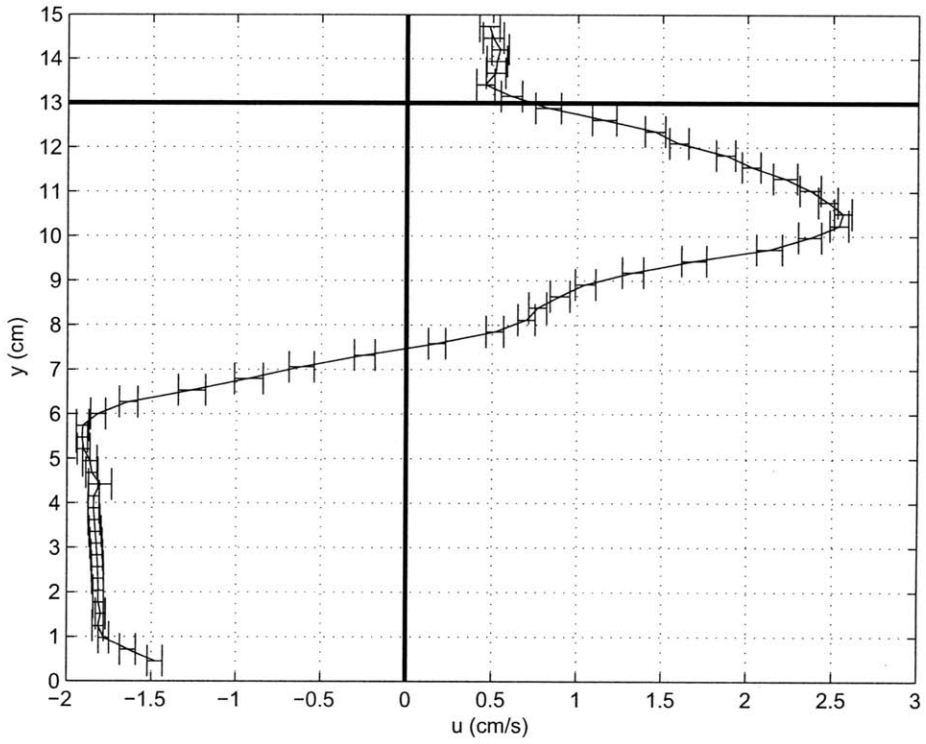

Figure A.3: Averaged velocity profile for case 3.

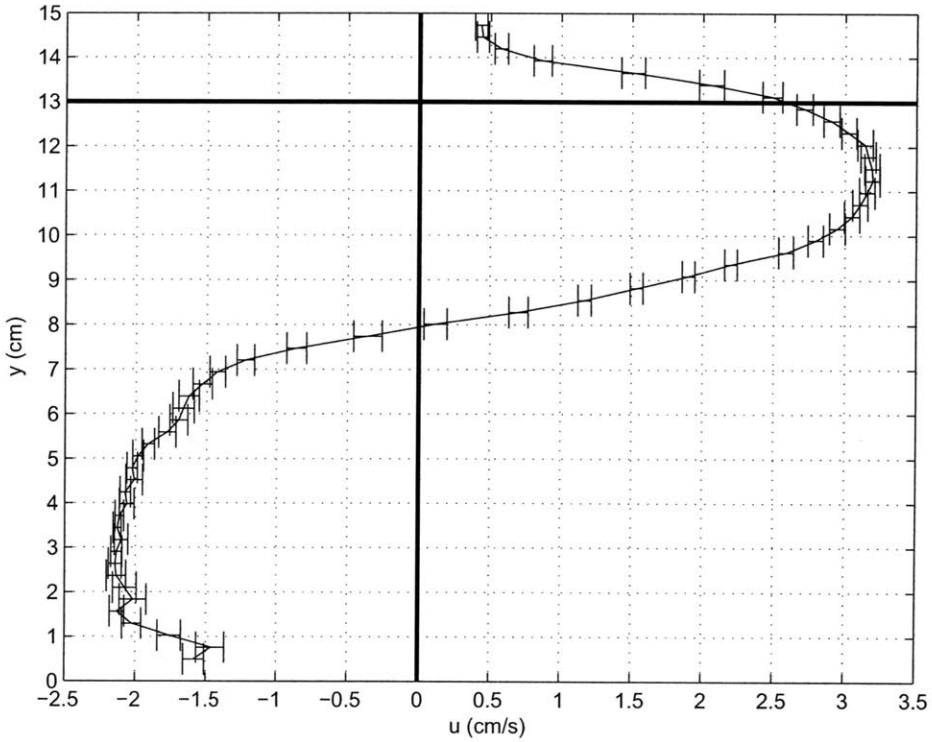

Figure A.4: Averaged velocity profile for case 4.

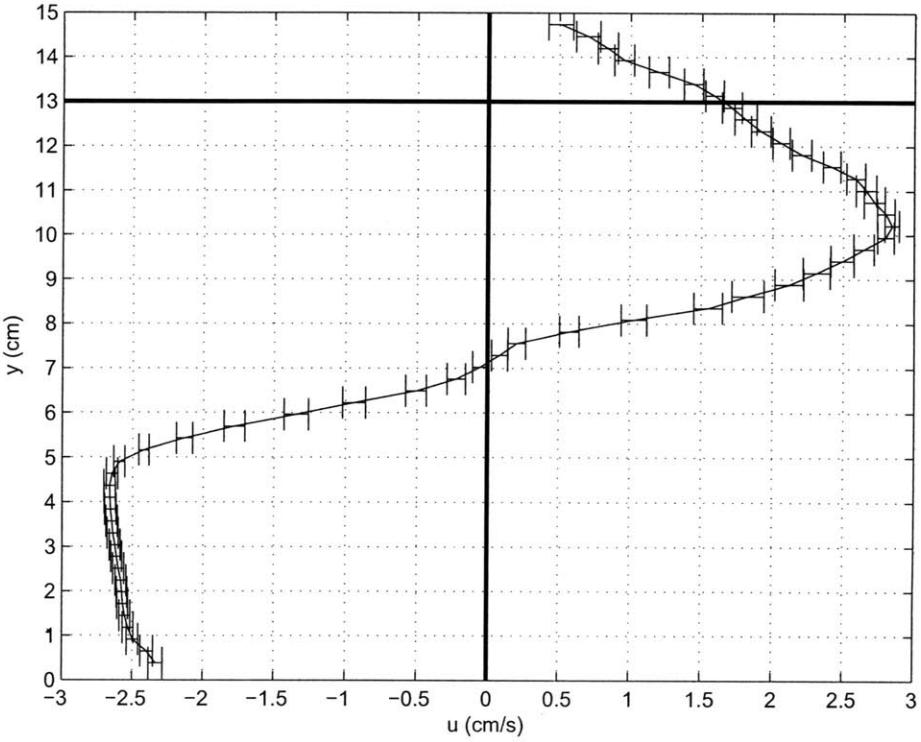

Figure A.5: Averaged velocity profile for case 5.

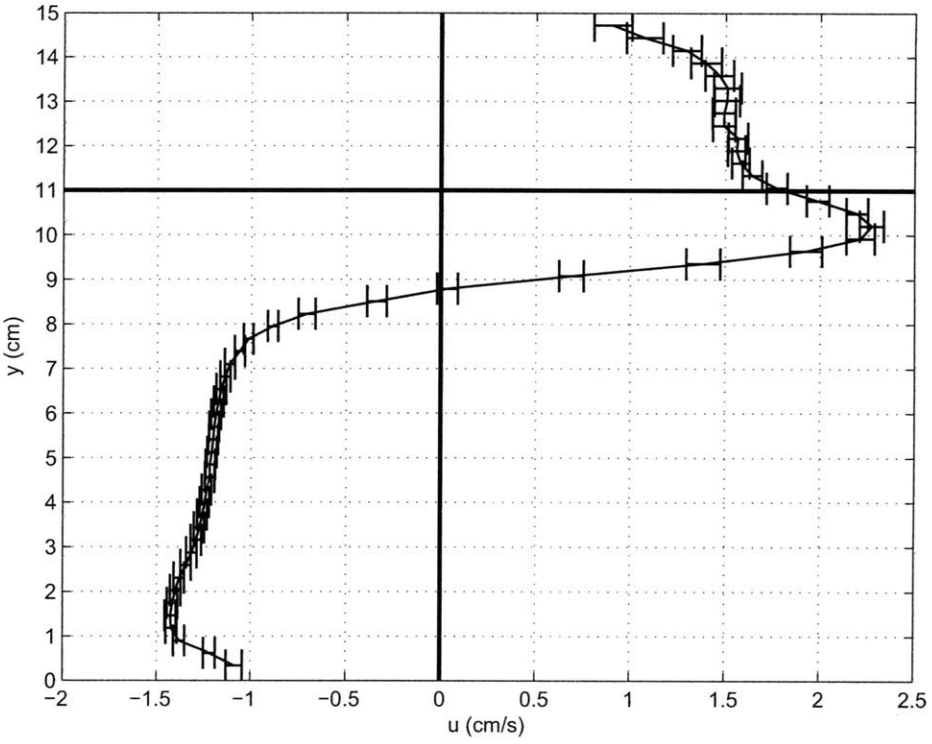

Figure A.6: Averaged velocity profile for case 6.

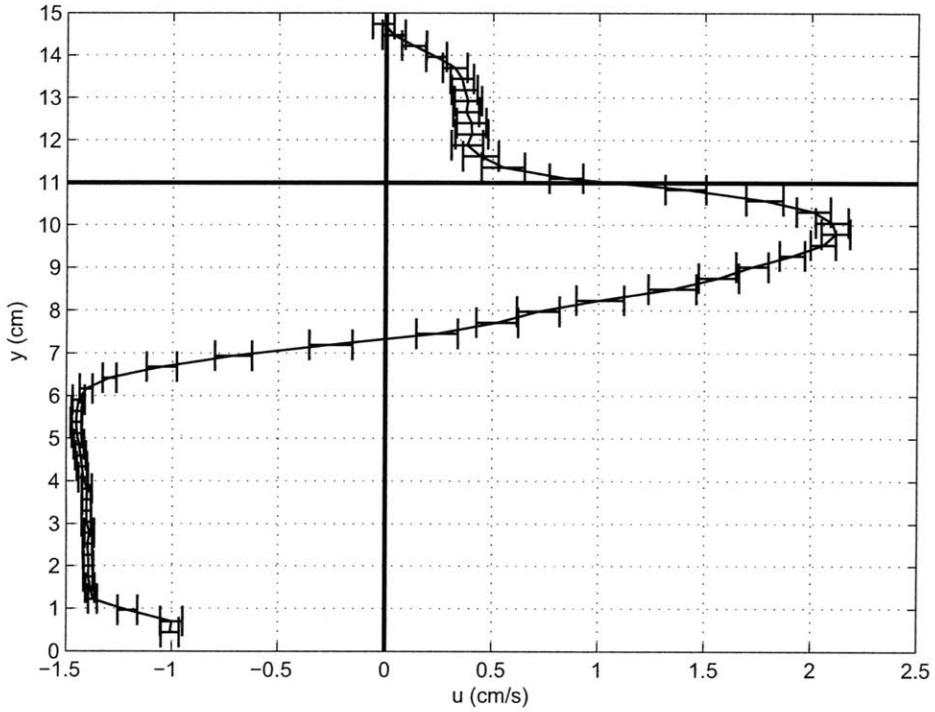

Figure A.7: Averaged velocity profile for case 7.

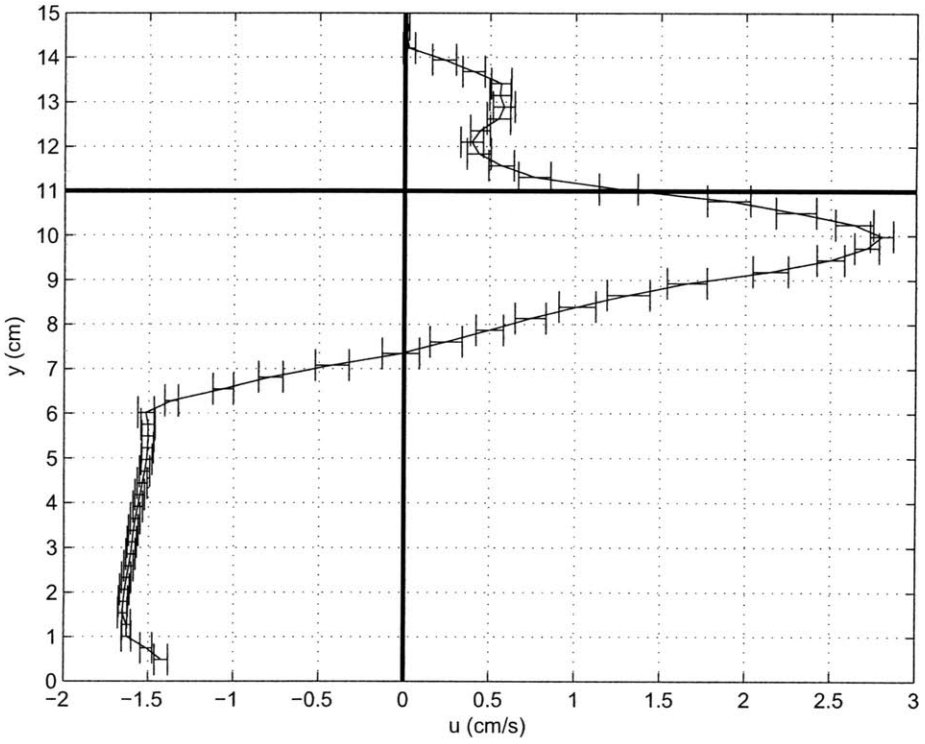

Figure A.8: Averaged velocity profile for case 8.

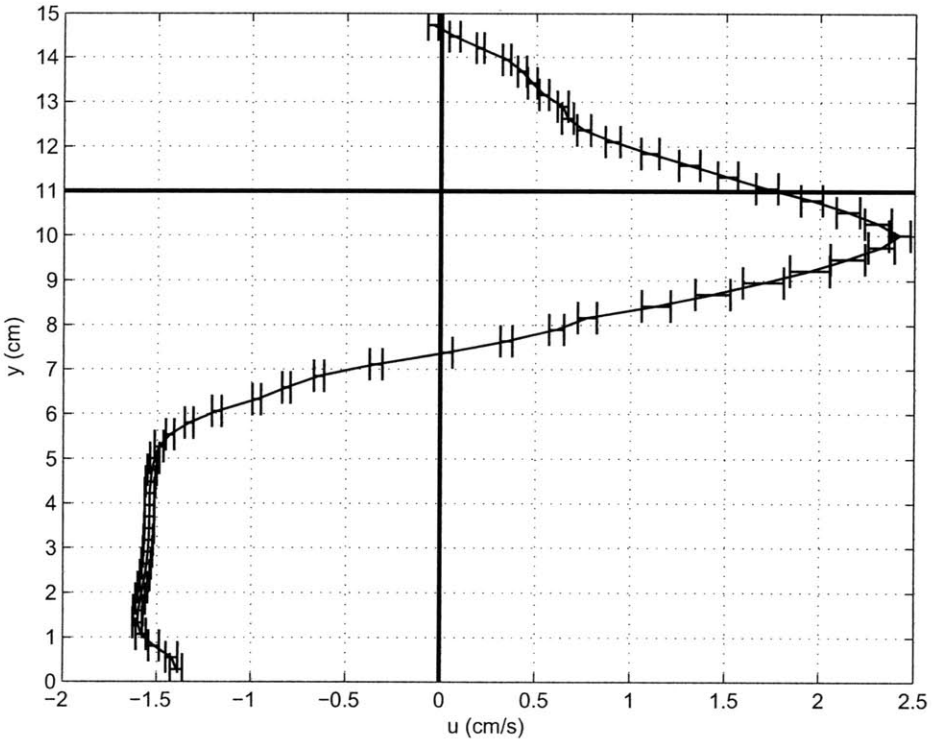

Figure A.9: Averaged velocity profile for case 9.

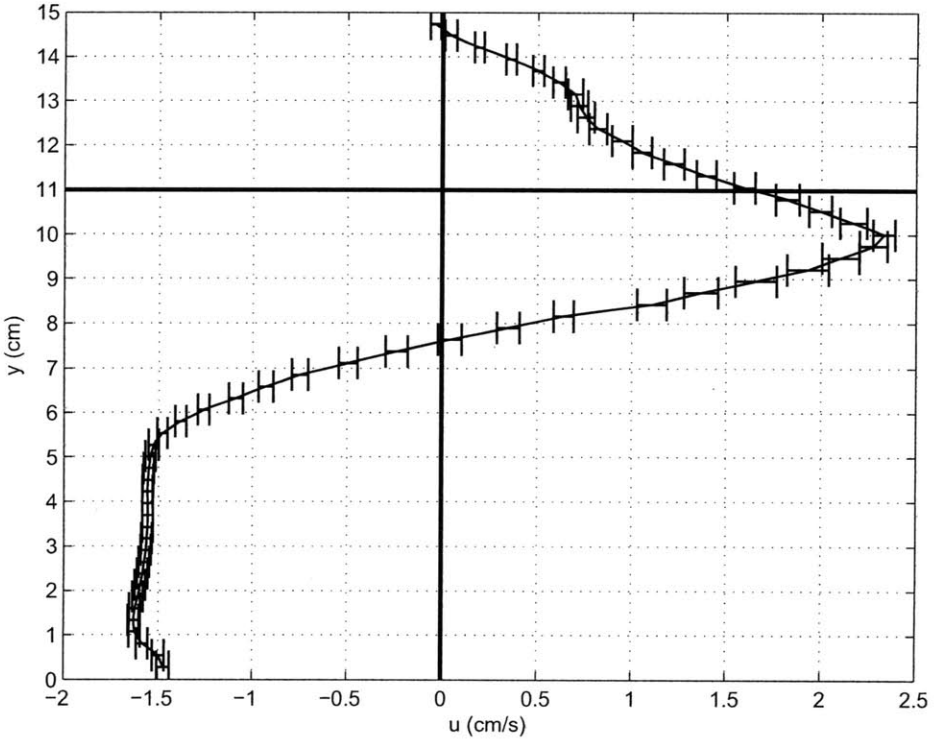

Figure A.10: Averaged velocity profile for case 10.

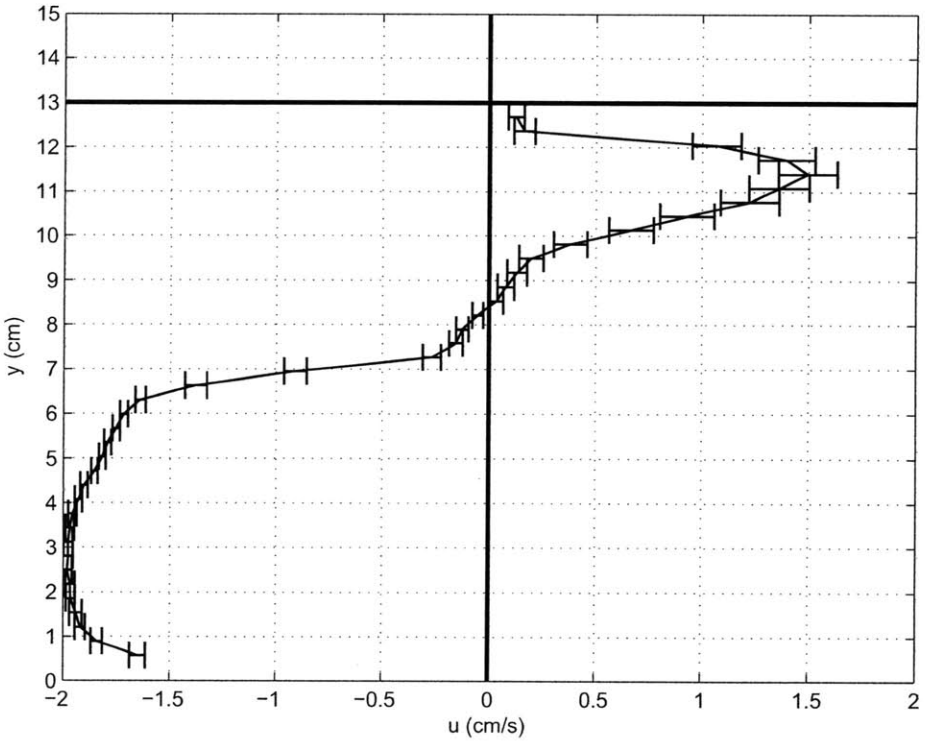

Figure A.11: Averaged velocity profile for case S1.

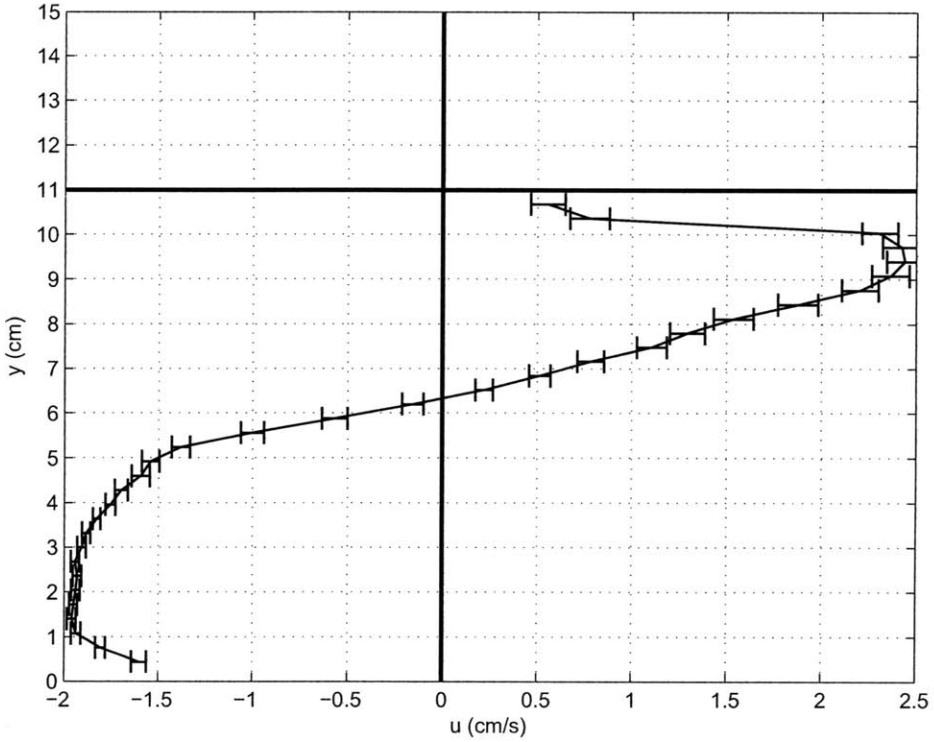

Figure A.12: Averaged velocity profile for case S2.

Bibliography

[1] Adams, C. S., R. R. Boar, D. S. Hubble, M. Gikungu, D. M. Harper, P. Hickley and N. Tarras-Wahlberg (2002), The dynamics and ecology of exotic tropical species in floating plant mats: Lake Naivasha, Kenya, *Hydrobiologia*, 488(1-3), 115–122.

[2] Adams, E. E. and D. J. Cosler (1988), Density exchange flow through a slotted curtain, *J. Hydraulic Res.*, 26(3), 261–273.

[3] Adams E. E., and S. A. Wells (1984), Field measurements on side arms of Lake Anna, VA.. *J. Hydraul. Eng.*, 110(6), 773–793.

[4] Azza, N., P. Denny, J. van de Koppel and F. Kansiime (2006), Floating mats: their occurrence and influence on shoreline distribution of emergent vegetation, *Freshwater Biology*, 51(7), pp. 1286–1297.

[5] Benjamin, T. B. (1968), Gravity currents and related phenomena. *J. Fluid Mech.*, 31, 209–248.

[6] Burke, R. W., and K. D. Stolzenbach (1983), Free surface flow through salt marsh grass, *MIT Sea Grant Coll. Program Rep. MITSG 83-16*, Mass. Inst. of Technol., Cambridge.

[7] Chimney, M. J., L. Wenkert, and K. C. Pietro (2006), Patterns of vertical stratification in a subtropical constructed wetland in south Florida (USA). *Ecol. Eng.*, 27s, 322-330.

[8] Coates, M. J., and J. C. Patterson (1993), Unsteady natural convection in a cavity with non-uniform absorption of radiation. *J. Fluid Mech.*, 256, 133–161.

[9] Coates, M., and J. Ferris (1994), The radiatively driven natural convection beneath a floating plang layer. *Limnol. Oceanogr.*, 39(5), 1186–1194.

[10] Dale, H. M. and T. Gillespie (1976), The influence of floatingvascular plants onthe diurnal fluctuations of temperature near the water surface in early spring. *Hydrobiologia*, 49(3), 245–256.

[11] Edwards, A. M., D. G. Wright, and T. Platt (2004), Biological heating effects of a band of phytoplankton. *J. Mar. Syst.*, 49, 89–103.

[12] Farrow, D. E., and J. C. Patterson (1993), On the response of a reservoir sidearm to diurnal heating and cooling. *J. Fluid Mech.*, 246, 143–161.

[13] Farrow, D. E. (2004), Periodically forced natural convection over slowly varying topography. *J. Fluid Mech.*, 508, 1–21.

[14] Gharib, M. and D. Daribi, (2000), Digital particle image velocimetry, in *Flow Visualization*, (Ed. Smits, A. J. & Lim, T. T.), Chapter 6, 123–147, Imperial College Press, London.

[15] Gill, A. E. (1982), *Atomsphere–Ocean Dynamics*, Academic Press, New York.

[16] Hatcher, L., A. J. Hogg, and A. W. Woods (2000), The effects of drag on turbulent gravity currents. *J. Fluid Mech.*, 416, 297–314.

[17] Hill, R. G. J. W. Webb and A. M. A. Smith (1987), Floating vegetation mats on a floodplain billabong in the Northern Territory of Australia, *Hydrobiologia*, 150, 153–164.

[18] Horsch G. M., and H. G. Stefan (1988), Convective circulation in littoral water due to surface cooling. *Limnol. Oceanogr.*, 33(5), 1068–1083.

[19] Jacob D. L. and M. L. Otte (2004), Long-term effects of submergence and wetland vegetation on metals in a 90-year old abandoned Pb-Zn mine tailings pond, *Environmental Pollution*, 130(3), 337–345.

[20] Jamali, M., X. Zhang and H. M. Nepf (2008), Exchange flow between a canopy and open water, *J. Fluid Mech.*, 611, 237–254.

[21] James, W. F., and J. W. Barko (1991), Estimation of phosphorus exchange between littoral and pelagic zones during nighttime convection circulation. *Limnol. Oceanogr.*, 36(1), 179–187.

[22] James, W. F., J. W. Barko, and H. L. Eakin (1994), Convective water exchanges during differential cooling and heating: implications for dissolved constituent transport. *Hydrobiologia*, 394, 167–176.

[23] James, W. F., and J. W. Barko (1999), Convective water exchanges in a wind-sheltered littorall region of Eau Reservoir, Wisconsin USA. *Arch. Hydrobiol*, 145(3), 373–383.

[24] Jirka, G. H. (1979), Supercritical withdrawal from two-layered fluid system - Part 1: two dimensional skimmer wall, *J. Hydraulic Res.*, 17(1), 43–51.

[25] Kadlec, R. C. (2002), Overland flow in wetlands: Vegetation resistance, *J. Hydraul. Eng.*, 116(5), 691–706.

[26] Koch, D. L. and A. J. C. Ladd (1997), Moderate Reynolds number flows through periodic and random arrays of aligned cylinders, *J. Fluid Mech.*, 349, 31–66.

[27] Knauer, K. H. Nepf and H. Hemond (2000). The production of chemical heterogeneity in Upper Mystic Lake. *Limnol. Oceanogr.*, 45(7), 1647–1654.

[28] Lee, P. F., and K. A. McNaughton (2004), Macrophyte induced microchemical changes in the water column of a northern Boreal Lake. *Hydorbiologia*, 522, 207–220.

[29] Lei, C. and J. C. Patterson (2002a), Natural convection in a reservoir sidearm subject to solar radiation: experimental observations, *Experiments in Fliuds*, 552, 207–220.

[30] Lei, C. and J. C. Patterson (2002b), Unsteady natural convection in a triangular enclosure induced by absorption of radiation. *J. Fluid Mech.*, 460, 181–209.

[31] Lightbody, A. F. and H. M. Nepf (2006), Prediction of velocity profiles and longitudinal dispersion in emergent salt mash vegetation, *Limnol. Oceanogr.*, 51(1), 218–228.

[32] Lightbody, A., Avener, M. and H. M. Nepf (2008), Observations of short-circuiting flow paths within a constructed treatment wetland in Augusta, Georgia, USA. *Limnol. Oceanogr.*, 53(3), 1040–1053.

[33] Lövstedt, C. B. and L. Bengtsson (2008), Density-driven current between reed belts and open water in a shallow lake, *Water Resour. Res.*, *44*, W10413, doi:10.1029/2008WR006969.

[34] Lowe, R. J., P. F. Linden, and J. W. Rottman (2002), A laboratory study of the velocity structure in an intrusive gravity current. *J. Fluid. Mech.*, 456, 33–48.

[35] MacIntyre, S., J. R. Romero and G. W. Kling (2002), Spatial-temporal variability in surface layer deepening and lateral advection in an embayment of Lake Victoria, East Africa. *Limnol. Oceanogr.*, 47(3), 657–671.

[36] Mariana, M., N. Mazzeo, B. Moss and L. Godrigues-Gallego (2003), The structuring role of free-floating versus submerged plants in a subtropical shallow lake, *Aqu. Eco.*, 37, 77–391.

[37] Mazda, Y., E. Wolanksi, B. King, A. Sase, D. Ohtsuka and M. Magi (1997), Drag forces due to vegetation in mangrove swamps, *Mangr. Salt Marsh*, 1, 193–199.

[38] Monismith, S. G., J. Imberger and M. L. Morison (1990), Convective motions in the sidearm of a small reservoir, *Limnol. Oceanogr.*, 35(8), 1676–1702.

[39] Nepf, H. M., and C. E. Oldham (1997), Exchange dynamics of a shallow contaminated wetland, *Aquat. Sci.*, 59(3), 193–213.

[40] Nepf, H. M. (1999), Drag, turbulence, and diffusion in flow through emergent vegetation. *Water Resour. Res.*, 35(2), 479–489.

[41] Oldham, C. E., and J. J. Sturman (2001), The effect of emergent vegetation on convective flushing in shallow wetlands: Scaling and experiment. *Limnol. Oceanogr.*, 46(6), 1486–1493.

[42] Padial, A. A., S. M. Thomaz, and A. A. Agostinho (2009), Effects of structural heterogeneity provided by the floating macrophyte Eichhornia azurea on the predation efficiency and habitat use of the small Neotropical fish Moenkhausia sanctaefilomenae, *Hydrobiologia*, 624, 161–170.

[43] Plew, D. R., R. H. Spigel, C. L. Stevens, R. I. Nokes and M. J. Davidson (2006), Stratified flow interactions with a suspended canopy, *Environ. Fluid Mech.*, 6, 519–539.

[44] Pokorný and Květ (2004), Aquatic plants and lake ecosystems, in *The Lakes Handbook* (ed. O'Sullivan, P. E. & Reynolds, C. S.), Vol. 1, Chapter 11, 309–340. Blackwell Science, Malden, MA.

[45] Sartoris, J. J., J. S. Thullen, L. B. Barber and D. E. Salas (2000), Investigation of nitrogen transformations in a southern California constructed wastewater treatment wetland. *Ecol. Eng.*, *14*, 49–65.

[46] Shin, J. O., S. B. Dalziel, and P. F. Linden (2004), Gravity currents produced by lock exchange. *J. Fluid Mech.*, 521, 1–34.

[47] Simpson, J. E. (1997), *Gravity currentes in the laboratory, atmosphere, and ocean*, Cambridge University Press, Cambridge.

[48] Sturman, J. J. and G. N. Ivey (1998), Unsteady convective exchange flows in cavities, *J. Fluid Mech.*, 386, 127–153.

[49] Sturman, J. J. C. E. Oldham and G. N. Ivey (1999), Steady convective exchange flows down slopes, *Aquat. Sci.*, 61, 260–278.

[50] Sveen, J. K. (2004), An introduction to MatPIV v. 1.6.1., Internet Resources.

[51] Tanino, Y., H. M. Nepf and P. S. Kulis (2005), Gravity currents in aquatic canopies, *Water Resour. Res.*, 41, W12402, doi:10.1029/2005WR004216.

[52] Tanino, Y., and H. M. Nepf (2008), Laboratory investigation of mean drag in a random array of rigid, emergent cylinders, *J. Hydraul Eng.*, 134(1), 34–41

[53] Trevisan, O. V. and A. Gejan (1986), Convection driven by the non uniform absorption of thermal radiation at the free-surface of a stagnant pool, *Numerical Heat Transfer*, 10(5), 483–506.

[54] Ultsch, G. (1973), The effect of water hyacinth (Eichhornia crassipes) on the microenvironment of aquatic communities. *Archiv. Hydrobiologia*, 72, 460–473.

[55] Wetzel, R. G. (2001), Light in inland water, in *Limnology*, 3rd Ed. Academic Press, San Diego, CA.

[56] White, F. M. (1991), *Viscous Fluid Flow*, 2nd ed., McGraw-Hill, New York.

[57] Zhang, X. and H. M. Nepf (2008), Density Driven Exchange Flow between Open Water and an Aquatic Canopy, *Water Resour. Res.*, *44*, W08417, doi:10.1029/2007WR006676.

[58] Zhang, X. and H. M. Nepf (2009), Thermally Driven Exchange Flow between Open Water and an Aquatic Canopy, *J. Fluid Mech.*, 632, pp. 227-243.